AFCRL-67-0201

AD656658

# TECHNICAL REPORT

# ANALYTICAL AND EXPERIMENTAL STUDIES OF MICROWAVE INTERACTION WITH A HYPERSONIC AIR PLASMA

By: Donald W. Boyer and Dean R. Bitikofer

CAL No. AA-2053-Y-1

Contract No. AF 19(628)-4968
Project No. 4642
Task No. 464202

Scientific Report No. 1
February 1967





Contract Monitor
John F. Lennon
Microwave Physics Laboratory

Distribution of this document is unlimited

Prepared for:
Air Force Cambridge Research Laboratories
Office of Aerospace Research
Bedford, Massachusetts 01730

CORNELL AERONAUTICAL LABORATORY, INC.
OF CORNELL UNIVERSITY, BUFFALO, N. Y. 14221

AFCRL-67-0201

# ANALYTICAL AND EXPERIMENTAL STUDIES OF MICROWAVE INTERACTION WITH A HYPERSONIC AIR PLASMA

Donald W. Boyer
Dean R. Bitikofer

Cornell Aeronautical Laboratory, Inc.
of Cornell University
Buffalo, New York 14221

Contract No. AF19 (628)-4968

Project No. 4642

Task No. 464202

Scientific Report No. 1

February 1967

Contract Monitor
John F. Lennon



Prepared for:

AIR FORCE CAMBRIDGE RESEARCH LABORATORIES
OFFICE OF AEROSPACE RESEARCH
UNITED STATES AIR FORCE
BEDFORD, MASSACHUSETTS 01730

CORNELL AERONAUTICAL LABORATORY, INC.
BUFFALO, NEW YORK 14221

# ANALYTICAL AND EXPERIMENTAL STUDIES OF MICROWAVE INTERACTION WITH A HYPERSONIC AIR PLASMA

CONTRACT NO. AF 19(628)-4968

FEBRUARY 1967

PREPARED FOR:

ELECTRONICS SYSTEMS DIVISION
AIR FORCE SYSTEMS COMMAND
UNITED STATES AIR FORCE
BEDFORD, MASSACHUSETTS 01730

PREPARED BY:

*D.W. Boyer, Project Engineer*
*Aerodynamic Research Department*

APPROVED BY:

*J.G. Hall, Head*
*Aerodynamic Research Department*

*D.R. Bitikofer*
*Electronics Research Department*

*R.E. Kell, Assistant Head*
*Electronics Research Department*

## FOREWORD

The work reported herein was sponsored by the Air Force Cambridge Research Laboratories, Office of Aerospace Research, USAF, under Contract AF 19(628)-4968. Mr. John Lennon of the AFCRL Microwave Physics Laboratory served as the technical monitor.

This research was performed during the period February 1965 through December 1966 by the Cornell Aeronautical Laboratory Aerodynamic Research Department with the Electronics Research and the Hypersonic Facilities Departments collaborating; the tests were conducted in the CAL 96-inch Hypersonic Shock Tunnel during May 1966.

In addition to those whose names appear on the title page, major contributors to this program included: Mr. B. R. Tripp in various phases of the program, particularly the microwave aspects and Mr. D. R. Romeo in the performance of the shock-tunnel experiment. Acknowledgment is also made of the cooperation of the Sandia Corporation for the use of certain electronic components and machine-computer programs developed under Contracts P. O. 4804 and 5003.

## ABSTRACT

Analytical and experimental studies are described of phenomena associated with the interaction of microwave radiation with the aerodynamically generated plasma surrounding a hemisphere-cylinder model in the CAL High Energy Shock Tunnel. The report is an interim report on continuing studies.

The program consisted of three parts, namely, (1) measurements of the changes in antenna radiation patterns at C-band (4.25 GHz), (2) an investigation of antenna breakdown, and nonlinear signal transmission effects, at S-band (2.7 GHz), and (3) measurements of the coupling between two antennas at S-band.

Nonequilibrium flow field calculations are discussed which describe the plasma properties in the vicinity of the antennas on the model. Analytical calculations have also included the computation of the complex transmission and reflection coefficients for microwave propagation through the inhomogeneous afterbody shock layer plasma.

A Phase I series of experiments measured the effect of the hypervelocity plasma on the radiation pattern of a C-band transmitting antenna located on the model cylindrical afterbody. Measurements of signal attenuation were made at four locations in the roll plane about the model at angular positions up to 90° from the normal to the waveguide antenna aperture. The measurements indicated an increase in the signal attenuation with angular departure of the receiving antenna from the aperture normal.

A Phase II experimental program investigated nonlinear interaction effects due to propagation of variable high power S-band pulse radiation through the afterbody shock layer plasma. These latter tests also included measurements of the effect of the plasma on the coupling between two adjacent S-band antennas. While the coupling measurements were successful, no nonlinear interaction effects were observed at the Phase II antenna power levels, primarily as a result of high power reflection due to plasma-induced antenna mismatch effects. Breakdown and coupling studies are to be continued at considerably higher power levels in a Phase III test program.

TABLE OF CONTENTS


| Section | | | Page |
|---|---|---|---|
| I | INTRODUCTION | | 1 |
| II | THEORETICAL CALCULATIONS OF THE ENVIRONMENTAL FLOW FIELD AND ELECTRO-MAGNETIC INTERACTION EFFECTS | | 3 |
| | 2.1 | Introduction | 3 |
| | 2.2 | Nonequilibrium Nozzle Flow | 4 |
| | 2.3 | Body Nose Region Flow | 5 |
| | 2.4 | Axisymmetric After body Flow | 7 |
| | 2.5 | Microwave Propagation Calculations | 9 |
| | 2.6 | Qualifying Comments on the Theoretical Solutions | ii |
| III | EXPERIMENTAL ENVIRONMENT | | 13 |
| | 3.1 | Hypersonic Shock Tunnel | 13 |
| | 3.2 | Dielectric Test Section | 13 |
| | | 3.2.1 Description and Design | 13 |
| | | 3.2.2 Electrical Performance | 15 |
| | 3.3 | External Preparation for Microwave Tests | 17 |
| | 3.4 | Test Model | 19 |
| | | 3.4.1 Antennas | 19 |
| | | 3.4.2 Pressure and Heat Transfer Instrumentation | 20 |
| | | 3.4.3 Electrostatic Probes | 21 |
| IV | EXPERIMENTAL PROGRAMS | | 23 |
| | 4.1 | Aerodynamic and Environment Calibration and Purity of Airflow | 23 |
| | 4.2 | Antenna Pattern Studies | 26 |

TABLE OF CONTENTS (Cont.)


| Section | | | Page |
|---|---|---|---|
| | 4.2.1 | Microwave Instrumentation for the Pattern Tests | 26 |
| | 4.2.2 | Evaluation of the Dielectric Test Section for Pattern Measurements | 28 |
| | 4.2.3 | Experiments | 29 |
| | 4.2.4 | Experimental Results and Discussion | 32 |
| | | 4.2.4.1 Pattern Studies | 32 |
| | | 4.2.4.2 Electrostatic Probes | 36 |
| | | 4.2.4.3 Surface Pressure and Heat Transfer | 37 |
| 4.3 | Breakdown Studies | | 38 |
| | 4.3.1 | Microwave Instrumentation for the Breakdown Tests | 39 |
| | | 4.3.1.1 General Functional Description | 39 |
| | | 4.3.1.2 Pulse Transmitter and Receiver | 41 |
| | | 4.3.1.3 CW Transmitter and Receiver | 42 |
| | | 4.3.1.4 Pulse and Waveform Generator Subsystem | 43 |
| | 4.3.2 | Experiments | 44 |
| | 4.3.3 | Experimental Results and Discussion | 45 |
| V | CONCLUSIONS | | 50 |
| | REFERENCES | | 53 |

## LIST OF ILLUSTRATIONS


| Figure | | Page |
|---|---|---|
| 1 | Species Distributions for Pure Airflow in the CAL Hypersonic Nozzle | 55 |
| 2 | Density Variation in Hypersonic Nozzle Airflow | 56 |
| 3 | Electron Number Density Profiles Calculated Normal to the Shock in the Nose Region of the 12-Inch Diameter Hemisphere-Cylinder Model | 57 |
| 4 | Electron Collision Frequency Profiles, Calculated Normal to the Shock in the Nose Region of the Hemisphere-Cylinder Model | 58 |
| 5 | Electron Number Density Profiles Calculated Along Rays Normal to Model Afterbody Surface | 59 |
| 6 | Collision Frequency Profiles Calculated Along Rays Normal to Model Afterbody Surface | 60 |
| 7 | Calculated Surface Pressure Distribution Over the 12-Inch Diameter Hemisphere Cylinder Model | 61 |
| 8 | Calculated Boundary Layer Edge Conditions on Model Afterbody | 62 |
| 9 | Transmission and Reflection Coefficients for Propagation at 4.25 GHz Along Rays Normal to Body Surface | 63 |
| 10 | Transmission and Reflection Coefficients for Propagation at 2.7 GHz Along Rays Normal to Body Surface | 64 |
| 11 | Basic Components of the CAL 96-Inch High Energy Shock Tunnel | 65 |
| 12 | Schematic Diagram of Tunnel Layout | 66 |
| 13 | Dielectric Test Section - Reflection Coefficient vs. Frequency | 67 |
| 14 | Schematic of Reflection Measurement | 68 |
| 15 | Antenna Reflection Coefficient vs. Antenna-Dielectric Wall Spacing | 69 |
| 16 | Experimental Arrangement for Antenna Radiation Pattern Measurements | 70 |
| 17 | Experimental Arrangement for Antenna Breakdown Studies | 71 |
| 18 | Test Section Pitot Pressure Distribution, $L$ = 4 Ft. | 72 |
| 19 | Test Section Pitot Pressure Distribution, $L$ = 6 Ft. | 73 |
| 20 | Simplified Block Diagram of Single Frequency Microwave Interferometer | 74 |

## LIST OF ILLUSTRATIONS (cont.)


| Figure | | Page |
|---|---|---|
| 21 | X-Band Interferometer Response in a Hypersonic Airstream With Slight Contamination | 75 |
| 22 | X-Band Interferometer Response in a Pure Hypersonic Airstream | 76 |
| 23 | Functional Block Diagram of Microwave Instrumentation for the Radiation Pattern Measurements | 77 |
| 24 | Functional Block Diagram of the Microwave Compression Receiver | 78 |
| 25 | Dynamic Range of Microwave Compression Receiver | 79 |
| 26 | Low Reflectance Test Section Performance | 80 |
| 27 | Incident and Reflected Power at Transmitter Antenna, and Received Signals | 81 |
| 28 | Received Signals at 0° and 45° Antenna Positions | 82 |
| 29 | Received Signals, $M_i$ = 8.52, Throat Diameter = 0.66 In. | 83 |
| 30 | Received Signals, $M_i$ = 8.55, Throat Diameter = 0.66 In. | 84 |
| 31 | Incident and Reflected Power at C-band Transmitter Antenna, Throat Diameter = 0.66 In. | 85 |
| 32 | Received Signals, $M_i$ = 8.57, Throat Diameter = 0.5 In. | 86 |
| 33 | Received Signals, $M_i$ = 8.53, Throat Diameter = 0.5 In. | 87 |
| 34 | Incident and Reflected Power at C-Band Transmitter Antenna, Throat Diameter = 0.5 In. | 88 |
| 35 | Signal Attenuation Through Hemisphere-Cylinder Model Afterbody Plasma, $M_i$ = 8.52, Throat Diameter = 0.66 In. | 89 |
| 36 | Signal Attenuation Through Hemisphere-Cylinder Model Afterbody Plasma, $M_i$ = 8.55, Throat Diameter = 0.66 In. | 90 |
| 37 | Signal Attenuation Through Hemisphere-Cylinder Model Afterbody Plasma, $M_i$ = 8.57, Throat Diameter = 0.50 In. | 91 |
| 38 | Signal Attenuation Through Hemisphere-Cylinder Model Afterbody Plasma, $M_i$ = 8.53, Throat Diameter = 0.50 In. | 92 |
| 39 | Measured Surface Pressure Distribution on Hemisphere-Cylinder Model | 93 |
| 40 | Measured Heat Transfer Distribution on Hemisphere-Cylinder Model | 94 |
| 41 | General View of the Microwave Instrumentation for the Breakdown Tests | 95 |
| 42 | Block Diagram of the Microwave Instrumentation for the Breakdown Tests | 96 |

LIST OF ILLUSTRATIONS (cont.)


| Figure | | Page |
|---|---|---|
| 43 | Trigger and RF Pulse Timing Sequence for the Breakdown Tests | 97 |
| 44 | Incident Microsecond Pulse Train Employed in the Breakdown Studies | 98 |
| 45 | Block Diagram of Microwave Instrumentation for the Breakdown Tests | 99 |
| 46 | Peak Power Output of the TWT Amplifier vs. Frequency | 100 |
| 47 | Typical One-Microsecond Pulses from the Sperry STS-101 TWT Amplifier | 101 |
| 48 | Received One-Microsecond Pulse | 102 |
| 49 | Breakdown Instrumentation - Pulser and Waveform Generator Subsystem | 103 |
| 50 | CW Signal Attenuation at 2.84 GHz and Pulse Train | 104 |
| 51 | Received Pulse Shapes in the Breakdown Tests | 105 |
| 52 | Received Pulse Pair in the Breakdown Tests | 106 |
| 53 | Coupling Between Two S-Band Antennas | 107 |
| 54 | Reflected Power at Transmitter Antenna | 108 |

BLANK PAGE

# I. INTRODUCTION

This is an interim report on continuing analytical and experimental studies of the interaction of microwave radiation with the aerodynamically generated pure-air plasma surrounding a hemisphere-cylinder model in the CAL High Energy Shock Tunnel. The intention in these studies is to provide further insight into microwave-plasma interaction phenomena which characterize electromagnetic radiation from simple waveguide antennas on a hypervelocity vehicle. In particular, the phenomena investigated were changes in antenna radiation patterns, antenna reflection coefficient (magnitude only), mutual coupling between two antennas, and nonlinear plasma-microwave signal interaction effects.

While laboratory gas discharge experiments can be designed to produce plasmas possessing electron number densities of interest and can yield useful results, the interaction phenomena mentioned are very dependent upon the thermodynamic state of the plasma, and experiments under high enthalpy flow conditions are necessary to ensure a reentry type flow environment around the body – an environment characterized by a high velocity of the plasma over the antenna. The reentry situation is further characterized by gradients in the electron number density and collision frequency both in the stream direction and in the direction normal to the body surface, and by the presence of a boundary layer growing along the body surface, which engulfs the high temperature (high electron density) streamlines which passed through the strongest portion of the bow shock wave. The engulfed entropy layer flow then contributes to heat transfer to the body surface at the expense of peak electron density level in the inviscid plasma flow. Ideally, all these factors must be present in an experimental plasma environment to best ensure a reasonable interpretation of actual flight microwave transmission behavior based on the results of facility experiments. It is reiterated, however, that the present studies were concerned with a pure-air plasma. The effects of ablation on microwave transmission were not included in the analysis and experiments. Actually, in the reentry case, ablation products may significantly alter the microwave properties of the plasma and a more complete

understanding of transmission problems in the reentry case must eventually require the inclusion of such effects.

The aims of the present program were first, to continue previous antenna radiation pattern studies under pure-air conditions (Reference 1) at C-band in the new High Energy Shock Tunnel, which provided a dielectric test section specially designed for the performance of microwave-plasma interaction studies, and secondly, to extend the interaction studies to higher power levels to investigate nonlinear propagation and breakdown phenomena. While not included in the original program plan, these latter studies were also extended to include measurements of the effect of the plasma on the coupling between two adjacent antennas.

Theoretical studies included the computation of the effects of non-equilibrium in the tunnel freestream, nose region and afterbody flow fields, and of the complex transmission, reflection, and absorption coefficients for microwave propagation through the afterbody shock layer plasma.

The theoretical studies are discussed in Section II, and the details of the test facility, microwave environment, and instrumented model are described in Section III. A description of the microwave instrumentation pertinent to the pattern shift and breakdown experiments is presented in Section IV along with the details of the actual experiments and the experimental results.

# II. THEORETICAL CALCULATIONS OF THE ENVIRONMENTAL FLOW FIELD AND ELECTROMAGNETIC INTERACTION EFFECTS

## 2.1 Introduction

Basic to the understanding and interpretation of experimental measurements of microwave transmission effects in a plasma is the analytical description of the gasdynamic, chemical, and electrical properties of the flow in the region of interest. In essence, the important parameters in the present study are the shock layer electron number density and collision frequency profiles at the antenna locations on the model. However, in order to provide an accurate analytical description of these parameters in flows appropriate to experimental studies at high total enthalpy levels, calculations must include the consideration of nonequilibrium effects which arise as a result of shock-induced processes in the flow around the body as well as those which are peculiar to the test environment itself. Particularly, in the shock tunnel, since the relative motion between the body and the freestream is generated by the expansion of shock-processed test gas from an initial (reservoir) state wherein the gas is appreciably dissociated and partially ionized, the cumulative effects of nonequilibrium require that we consider the solution for the nonequilibrium state of the entire flow from the moment the gas starts to expand into the nozzle, down to the model freestream, into the body nose flow region and through the expansion to the afterbody flow region in order to arrive at predictions for the electron number density and collision frequency in the vicinity of the antennas. Accordingly, a brief description is first given of the method of flow calculation in each of these regions prior to a discussion of the calculation of microwave propagation through the prescribed afterbody plasma.

The required flow field solutions are accomplished by means of computer programs which have been developed at CAL[2, 3, 4] for the calculation of internal and external flows undergoing coupled finite-rate chemical and ionization processes. In describing such nonequilibrium flows, an 8-species air model, including only the $NO^+$ ion, has been assumed with

adjustments between the species concentrations determined by 11 chemical reactions. The single reaction controlling the plasma electron concentration is the efficient binary process $NO^+ + e^- \rightleftharpoons N + O$. The reaction kinetic data employed in the flow field calculations are presented in Table 1.[2, 5]

## 2.2 Nonequilibrium Nozzle Flow

The effect of chemical nonequilibrium on the inviscid one-dimensional expansion of the reservoir gas in a hypersonic nozzle is computed by numerical integration of the governing chemical and fluid flow equations. The rotational, vibrational, and electronic degrees of freedon are assumed to remain equilibrated throughout the expansion and only the interchange of chemical energy with the flow process is considered. The program requires the specification of the initial equilibrium reservoir state (temperature and pressure) for the chemical system and the prescribed local to throat area ratio vs. axial distance distribution for the particular nozzle.

The theoretical species distributions for a pure airflow expansion in the hypersonic nozzle used for the work reported herein are shown in Fig. 1. The reservoir conditions assumed were those of the actual experiments to be described. The figure illustrates the considerable departure from composition equilibrium in some species, including electrons, occurring in the nozzle freestream for conditions typical of high enthalpy shock tunnel operation. While the dissociation energy of nitrogen is completely recovered in the expansion because of the fast nitric oxide shuffle reactions (Table I, reactions 8, 9), the O and NO concentrations freeze in the early portion of the nozzle expansion. In this case, however, the frozen static enthalpy only amounts to about 3.5% of the total enthalpy of the flow. The variation in gas density in the nozzle is shown in Fig. 2. Selected equivalent density altitudes of the hypervelocity freestream are also indicated on the figure. The present tests were performed at an equivalent density altitude of 155,000 feet.

## 2.3 Body Nose Region Flow

The computation of the inviscid flow in the subsonic-transonic region about a blunt, axisymmetric body is performed by means of an inverse method calculation which can be iterated to yield a desired body shape.[4] The fluid flow and chemical and vibrational rate equations are integrated numerically with the initial conditions imposed by the assumed shock shape and tunnel freestream (or flight) conditions. The calculation further includes the computation of the boundary layer growth around the real or desired body shape in such a manner that the viscous-inviscid interaction problem is solved in a step by step fashion. This is accomplished by computation of the boundary layer edge coordinates and the mass flux in the boundary layer, and by the location of that point in the inviscid flow which has the same mass flux (between it and the wall) as that in the boundary layer. Differences between the coordinates of this inviscid point and those of the boundary layer edge are used to adjust the shock shape and the integration is repeated until overall consistency in the boundary layer and inviscid mass flows is obtained for the desired body shape. The inclusion of the boundary layer in the stagnation region and afterbody flow field calculations is necessary since the density levels corresponding to equivalent flight altitudes of interest, even behind the strong shocks of hypersonic flow, are so low that the boundary layer may represent a sizeable fraction of the shock layer. The boundary layer effectively alters the shape of the body and so affects the pressure distribution, the shock shape, and all the other flow variables.

The parameters of importance in investigations of microwave interaction phenomena are the plasma electron number density, $\eta_e$, and the collision frequency, $\nu_e$, as well as their spatial distributions. Profiles of these parameters, along rays normal to the bow shock wave in the nose region, are shown in Figs. 3 and 4, respectively, for several angular ray locations over the hemispherical nose of the 12-inch diameter CRL hemisphere-cylinder model employed in the experimental studies. In the figures, the coordinate $y$ is the distance along the ray normal to the shock, and the profiles shown extend over 98% of the distance to the body surface. Again,

the test conditions assumed correspond to those of the actual experiments. At the particular microwave frequencies of interest in this program, namely, 2.7 GHz and 4.25 GHz, it is seen that the subsonic nose region plasma ($\theta \leq 20^{\circ}$) is at least an order of magnitude overdense to the microwave radiation. Microwave propagation calculations (Sec. 2.5) have indicated, for example, that even for propagation through the shock layer in the region of the sonic line, the corresponding plasma properties (Figs. 3 and 4, $\theta = 21^{\circ}$) result in a signal transmission loss, according to simple plane wave theory, which varies from -50 dB to -60 dB in the frequency range from 2.7 GHz to 4.25 GHz. Owing to sensitivity limitations of the instrumentation, therefore, no transmission measurements from the stagnation region antenna were included in these experiments.

The collision frequencies of Fig. 4 were computed according to the relation[6]

$$\nu_c = \frac{4}{3}\left(\frac{8kT_e}{\pi m_e}\right)^{1/2} \sum_j n_j Q_j \qquad (\omega > \nu_c)$$

where $k$ is the Boltzmann constant and $m_e$ is the electron mass; $n_j$ and $Q_j$ are, respectively, the number density and collision cross section of the $j^{th}$ species. In the above expression, which may be written

$$\nu_c = 7.32 \times 10^5 T_e^{1/2} \sum_j n_j Q_j \quad sec^{-1}$$

the actual electron temperature, $T_e$, is not known. Owing to the small fractional kinetic energy loss sustained by the electrons in a collision, the electrons may be largely energetically isolated from the rest of the flow during expansion in the hypersonic nozzle. As a result the electron temperature in the hypervelocity freestream may be an appreciable fraction of the initial reservoir temperature. The nonequilibrium, heavy particle temperature on the other hand is quite low ($\sim 330^{\circ}$ K). In computing the electrical properties of the flow corresponding to the X-band interferometer station in the nozzle, a somewhat arbitrary practice has been to freeze the electron temperature at the gas temperature where departure from chemical equilibrium in species concentrations becomes evident. For the conditions of tunnel operation pertinent to these studies, the above criterion resulted in an electron

temperature assumed to remain constant at 3600° K throughout the nozzle expansion. The temperature $T_e$ = 3600°K was assumed in the calculation of the collision frequency profiles of Fig. 4. In addition, and solely as an illustration of the effect of the uncertainty in the electron temperature on the calculated collision frequencies, the profiles corresponding to the maximum ($\theta$ = 44°) and minimum ($\theta$ = 14°) angular ray locations in the nose region solution were also calculated assuming the electron temperature to be equal to the local nonequilibrium gas temperature in the shock layer. The corresponding collision frequency profiles are indicated by the dashed lines in the figure. The further effect of assuming an electron temperature equal to the cold freestream gas temperature ahead of the bow shock is also indicated for one profile case. It is seen that, apart from the unrealistic cold $T_e$ case, the collision frequency is not particularly sensitive to the present choice of electron temperature. It may be noted, parenthetically, that the above uncertainty in the magnitude of the collision frequency is aggravated also to some extent by the usual approximation, inherent in Eq. (1), in which the species cross sections are assumed independent of the electron velocity. This overall uncertainty in the collision frequency is unfortunate in view of the important role of this parameter in electromagnetic interaction phenomena.

## 2.4 Axisymmetric Afterbody Flow

The solution for the axisymmetric supersonic nose region and afterbody flow field is accomplished by means of an adaptation of the method of characteristics which employs a mesh composed of streamlines and rays normal to the body. The conventional characteristics mesh is unsatisfactory in finite-rate flow field calculations owing to the large order of magnitude changes in the concentrations of some species across the shock layer. The necessary interpolation procedures along the characteristics can then lead to serious errors in the concentrations of these species. The nonequilibrium afterbody program is designed to accept the results of the nose region program as input data and consequently uses the same thermochemical model. A feature of the afterbody program is the inclusion of a boundary layer matching

procedure which computes the boundary layer step by step with the external flow and thus allows for all displacement interactions.

By means of the nose region and afterbody programs, the entire flow field about the CRL 12-inch diameter hemisphere-cylinder model has been calculated. The freestream conditions selected for computation were those at which the actual experiments were conducted. The particular theoretical calculations described herein were, in fact, performed subsequent to the tests.

Calculated distributions of the electron number density across the shock layer on the cylindrical afterbody of the model are shown in Fig. 5. The indicated profiles are along rays normal to the body surface and extend from the edge of the boundary layer to the shock wave. The selected rays correspond to the body shoulder position and to the center of each of the three antennas installed on the model cylindrical afterbody. The relative positions of these antennas are indicated schematically in Fig. 12. The peak electron number density is seen to fall off by a factor of 2 between the shoulder and the midpoint of the C-band antenna, located 4.75 inches downstream of the shoulder. These peak values are, in turn, considerably less than those existing over the hemispherical nose of the body (Fig. 3). This behavior results from the swallowing of the high-temperature entropy layer streamlines into the boundary layer as the flow expands around the body. The afterbody shock layer plasma is then essentially composed of streamlines which have passed through progressively weaker portions of the bow shock wave. The streamtube temperatures, and hence the peak electron number densities over a particular afterbody antenna location are, therefore, lower than those that would have existed over the antenna had more of the entropy layer flow persisted in the afterbody region. The corresponding calculated collision frequency profiles are shown in Fig. 6. For the purposes of the afterbody calculations, the electron temperature was assumed to remain constant along each streamline at about 90 percent of the initial streamline temperature immediately behind the bow shock. The electron temperature therefore decreases monotonically along the ray from the boundary layer edge to the shock wave. The gas density, however, and hence $\sum n Q$, increases monotonically along the ray. The net effect results in a minimum in the

profile and an increase in $\nu_e (\sim T_e^{1/2} \sum n_Q)$ as the shock is approached. The profiles of Figs. 5 and 6 then define the plasma properties for normal propagation of radiation from each of the antennas.

The characteristics calculation for the pressure distribution over the model surface, normalized to the body stagnation point pressure, is shown in Fig. 7. The antenna locations on the afterbody are also indicated in this figure. Finally, the variation of the flow velocity, temperature, mass density and electron number density at the edge of the boundary layer on the cylindrical afterbody are shown as a function of the distance aft of the body shoulder in Fig. 8.

## 2.5 Microwave Propagation Calculations

In order to aid in the analysis of microwave signal attenuation and antenna pattern distortion effects, a computer program has been developed at CAL[7] for the calculation of microwave propagation through plasmas of arbitrary properties. The program concept was evolved by CAL, under internal support, and the actual computer program was developed under Contract 4804, Suborder 3, from the Sandia Corporation. The program determines the complex transmission, reflection, and absorption coefficients of an inhomogeneous planar plasma slab having arbitrary electron number density and collision frequency profiles in the direction normal to the slab. The distinguishing characteristic feature of the program is its extremely high computational speed, typically yielding transmission and reflection coefficient data, at one frequency and for one angle of incidence, for a plasma approximated by 75 homogeneous slabs, in about one second of IBM 7044 machine time.

The original model of microwave transmission effects assumed that the plasma slab was bounded on either side by free space. It is recognized, however, that the assumption of free space boundaries does not represent the majority of real-life antenna problems. Since in many situations, including the present hypersonic tunnel experiments, the antenna is a waveguide installed in the metallic surface of the body, the computer solution was

extended* to provide for the calculation of microwave propagation through an inhomogeneous, lossy plasma slab from a source on an infinitely extended ground plane[8]. Microwave propagation calculations in the present study included both the free space and the ground plane solutions.

Propagation is analyzed by representing the plasma by several adjacent, homogeneous slabs which approximate the true variation in plasma characteristics. The electrical properties of each slab are characterized by an ABCD matrix for the purposes of analysis. The complex transmission and reflection coefficients of the composite plasma are determined by computing an overall ABCD matrix which relates the amplitude of the transverse electric field and amplitude of the transverse magnetic field on one side of the plasma to the corresponding quantities on the other side in terms of the product of the individual matrices. Both TE and TM modes of propagation (i.e., both polarizations) at arbitrary angles of incidence can be readily analyzed with this program. The fact that plane wave transmission coefficients can be so readily generated as a function of angle of incidence is important in solving problems concerning plasma-produced distortion of antenna radiation patterns by Fourier analysis techniques.

The profiles obtained from the flow field solutions, shown in Figs. 5 and 6, were used to compute the propagation of the incident antenna radiation through the shock layer plasma at each of the two signal frequencies employed in the program, at the appropriate antenna locations. The transmission and reflection coefficients calculated for 4.25 GHz and 2.7 GHz for plasma conditions normal to the body surface are shown in Figs. 9 and 10. The figures show the free-space and ground-plane solutions. In both cases, the ground plane result indicates a 2 to 3 dB increase in signal attenuation over the free-space result. The results also indicate that the C-band signal strength should sustain a 3 to 4 dB loss on propagation through the shock layer and that the S-band signal attenuation should be of the order of 5 to 8 dB. While the theoretical signal attenuations indicated above are within the measurement capability of the receiving equipment, the signal attenuations

*Under Contract 5003, Suborder 2, from the Sandia Corporation

actually measured at these test conditions (Secs. 4.2.4 and 4.3.3) were found to be considerably larger than the predicted values.

## 2.6 Qualifying Comments on the Theoretical Solutions

In view of the apparent discrepancies between experimental and theoretically predicted signal attenuations, it is necessary at this stage, following the presentation of the several theoretical methods employed to complement the experimental investigation, to comment on some possible inadequacies or uncertainties in the theoretical solutions.

While the solution for the afterbody flow field is, in itself, exact, the local magnitude of the plasma electrical properties is obviously dependent on the rate constant assigned to the $NO^+$ recombination reaction. The rate indicated in Table I is that almost universally used. The reaction rate, however, was actually measured for the ionization process, $N + O \rightarrow NO^+ + e^-$, and the reverse rate computed by means of the equilibrium constant. While an overall uncertainty of perhaps a factor of 5 is possible for this reaction, the effect of such a rate change on the present computed results has not been determined. Another point concerning the flow field calculations is the calculation of the boundary layer thickness. The necessity for including the boundary layer growth along the body surface has already been mentioned. The actual thickness of the local boundary layer, however, determines the amount of swallowing of the high entropy streamlines which in turn directly affects the peak magnitude of the electron number density profile in the inviscid shock layer. The present calculations have employed a locally similar, ideal gas calculation, including pressure gradient, for the computation of boundary layer thickness. It is noted, however, that the reacting boundary layer thickness will be somewhat thinner than the ideal gas result. Studies are, in fact, continuing at the present time to determine the effect of finite reaction rates on the boundary layer thickness in axisymmetric body flows. The calculations herein may, therefore, tend to underestimate the peak of the electron number density profile and hence the estimated loss in signal strength. This latter possibility is particularly significant in view of the critical dependence of the transmission coefficient on the peak electron

number density. It was shown, for example, in some of the initial calculations performed during the planning of this program, where the assumed test conditions rendered the peak $n_e$ just critical for 4.25 GHz radiation, that a 20% change in the peak $n_e$ produced a 40% dB change in attenuation.

Several remarks should also be made concerning the microwave propagation calculations. In this respect it is noted that the effect of gradients in the electrical properties of the flow transverse to the direction of propagation are not accounted for in the present program formulation. Furthermore, in both the ground-plane and free-space solutions, the plasma slab is assumed to be infinitely extended whereas in the present case, the model has a curved surface geometry of finite extent. In other words, the plane wave model may not adequately account for actual transmission effects. In addition, and probably first in importance, is the fact that since all the reflected waves are re-reflected by the ground plane, the effect of power reflection back into a finite-size slot aperture has not been taken into account in the ground-plane solution, a fact which could result in an appreciable underestimation of the overall signal attenuation for plasma conditions where appreciable power reflection occurs.

These discussions serve to emphasize the need for independent measurements of the plasma conditions at the antenna location, which would make it possible to determine if the discrepancy between predicted and measured effects is due to significant errors in flow field calculations, or electromagnetic calculations, or both.

# III. EXPERIMENTAL ENVIRONMENT

## 3.1 Hypersonic Shock Tunnel

The experiments to be described were performed in the CAL High Energy Shock Tunnel under conditions which generated a hypervelocity flow of pure air at 14,000 ft/sec at an equivalent density altitude of 155,000 ft. The general arrangement of the shock tunnel is shown in Fig. 11. The tunnel employs a chambered shock tube to shock process the air to the desired reservoir state prior to expansion to the test section through a selected axisymmetric nozzle. Hydrogen is used as the driver gas at pressures up to 25,000 psi and initial temperatures up to 750° F. In the present program a 10-1/2° half-angle conical nozzle was used having an exit diameter of 3 ft. The steel nozzle was equipped with a 15-inch-long mylar frustum section to permit nozzle freestream measurements to be made with an X-band interferometer. The nozzle exited into a special cylindrical dielectric test section, 4 feet in internal diameter and 10 feet long, located between the conical nozzle and the 8-foot diameter receiver tank.

The hemisphere-cylinder model was installed in the shock tunnel at the end of a sting which positioned the model antennas at about the axial midpoint of the dielectric test section. A sketch of the installation arrangement is shown in Fig. 12.

## 3.2 Dielectric Test Section

### 3.2.1 Description and Design

In order to provide a suitable environment for the conduct of microwave-plasma interaction studies in the shock tunnel, a unique low-reflectance dielectric test section was designed by CAL and fabricated by a contractor to our specifications. The design, construction, and checkout of the dielectric test section, as well as the other effort described in this section, were supported internally by CAL.

The test section consists of 10 layers of nylon phenolic honeycomb and 11 layers of fiberglass cloth in a sandwich-type construction giving a total wall thickness of approximately 4 inches. This construction provides adequate mechanical strength and vacuum integrity. The internal diameter of the test section is 4 ft. and its 10-ft. length permits measurements of antenna radiation patterns of plasma covered models and propagation path attenuation over a wide range of model viewing angles.

The extremely wideband microwave transmission properties were obtained from an intensive parametric investigation using the computer program for the computation of electromagnetic propagation in layered media (Sec. 2.5). With this approach, a laminated, low-reflectance dielectric wall was designed having a low power reflection coefficient which at no point exceeded 0.01 at normal incidence, as shown in Fig. 13, over the full decade frequency range from 1.0 GHz to 10 GHz. The reflection coefficients for angles of incidence in the range 0° - 88° were also computed with favorable results in that the peak reflection coefficient for TM mode propagation remained less than -20 dB, over the full decade, for angles of incidence up to 65°, whereas that for TE mode propagation remained better than -20 dB down for incidence angles up to 35°. Reflection coefficients were determined, experimentally, during the design phase with microwave measurements on a planar sample of the sandwich dielectric material and very good agreement was obtained between the predicted and measured values, the measured values actually lying about 2 - 3 dB below the computed result.

In addition to the above effort to minimize microwave reflection off the dielectric test section, theoretical and experimental investigations were made in order to determine an optimum test section length. While the test section should be much longer than its diameter in order to minimize diffraction and multipath effects resulting from the proximity of the metallic sections at the ends of the test section, aerodynamic requirements establish an upper bound to the useable length.

The limiting aerodynamic factors are test time and allowable flow expansion. The test time available is short, less than 1 millisecond, and an excessive test section length would increase the time required for

starting the flow at the expense of test time. The conical nozzle terminates at the entrance to the dielectric test section. However, since the conical expansion nozzle generates a source flow, the gas continues to expand in the stream direction further decreasing the density. Another aerodynamic restraint, therefore, is the necessity for testing at moderate hypersonic Mach numbers (8 - 10) in order to avoid expanding the flow to too low gaseous densities which would result in low electron number densities in the flow about the body.

Electromagnetic factors include diffraction and multipath effects, which were investigated with a scaled model of the shock tunnel. Tunnel dimensions were scaled so that measurements at 35 GHz could be used to predict effects at 1.5 GHz. Microwave field strengths were measured near the scaled metal tanks at the ends of the test section with the tank edges illuminated by an antenna in the scaled test section and the measurements were compared with similar measurements with the tanks removed. By varying the test section length, a minimum length was selected which yielded an acceptably small perturbation of the antenna radiation patterns.

In addition to the above considerations, cost and mechanical considerations made it desirable to limit the length of the dielectric test section. A length of 10 ft. was selected as being the best compromise of all factors. As a result of the tests with the scaled model, it was determined that most of the 10-ft. length is acceptable on electromagnetic grounds without significant distortion of the antenna radiation pattern.

### 3.2.2 Electrical Performance

The present program was the first experimental program to employ the new dielectric test section. Prior to the tests, therefore, the microwave reflection and transmission properties of the test section were measured at frequencies from S- to X-band.*

---

*Supported internally by CAL

## Reflection Measurements

A diagram of the experimental microwave set-up for the reflection measurements is shown in Fig. 14. A horn antenna was placed 5 ft. inside the test section and radiated outward perpendicular to the test section wall as indicated in the figure. A directional coupler and calibrated attenuator were used to measure reflected power. The horn antenna was matched to free space (zero reflected power) with the slide screw tuner before it was inserted inside the test section.

The reflection coefficient in dB relative to the power transmitted by the horn as a function of the horn to test section wall spacing, T, at 2.7 GHz is shown in Fig. 15. The increase in reflection coefficient as T increased from 20 to 24 inches is due to the focusing effect of the cylindrical walls. The cause of the ripple on the curve is uncertain; it may be due to environment reflections or inhomogeneity in the test section wall. In any event, the error in measuring the voltage reflection coefficient of an antenna in a shock tunnel model will be less than ±0.02 (-35 dB reflection coefficient).

Next, the spacing T was fixed and the test section was rolled about its cylindrical axis. If the dielectric was uniform in the circumferential direction, there would be no change in the reflection coefficient. With two trial values of T (1/2 and 24 inches), the reflection coefficient varied between -25 dB and -32 dB for the 1/2-inch spacing, and between -36 dB and -38 dB for the 24-inch spacing as the test section was rolled. The test frequency was 2.7 GHz.

## Transmission Measurements

For the transmission coefficient measurements, a transmitter horn was placed inside the test section (Fig. 14) and a receiver horn was placed outside about 10 to 22 inches away from the outside wall. Only normal incidence transmission as a function of test section roll angle, at T = 1/2 inch and 24 inches (see Fig. 14), was investigated. The results are shown in Table 2 below.

Table 2

TRANSMISSION FLUCTUATION FOR TEST SECTION
(Roll Angle 0 - 360°)

| Frequency (GHz) | T = 1/2" | T = 24" |
|---|---|---|
| 2.7 | ±0.3 dB | ±0.4 dB |
| 3.95 | ±0.6 dB | ±0.5 dB |
| 10.0 | | ±1.7 dB |

The variation in transmission as a function of roll angle is probably due to the nonhomogeneous test section distorting the wavefront, and is not believed to represent a change of dissipation loss. For shock tunnel antenna pattern measurements, changes of pattern with and without plasma are of interest. Therefore, the error in measurement of plasma-induced effects should be considerably less than the fluctuations tabulated above. At all three of the above frequencies, the transmission loss varied less than ±0.5 dB as transmitter-receiver horn spacing was varied.

The electrical tests have shown that microwave reflection and transmission vary somewhat because the shock tunnel test section is circumferentially nonhomogeneous. Nevertheless, the error in measuring voltage reflection coefficient and pattern for a shock tunnel model antenna is estimated at less than ±0.02 and ±0.5 dB, respectively. These errors are negligible for purposes of the present experimental investigation.

## 3.3 Preparations for Microwave Tests

Careful consideration was given to the area external to the tunnel in the vicinity of the dielectric test section, so that the placement of the necessary equipment would offer minimum interference to microwave-plasma interaction tests. A wooden arch was constructed to serve as a support for the receiving antennas. The antennas themselves were mounted at the ends of wooden poles which could be easily moved so as to position the antennas at any desired distance and angular displacement from the slot antennas on

the model. Microwave absorber material was installed on the arch to minimize roof and wall reflections, and additional absorber material was also placed on the floor under the dielectric test section. General views of the prepared tunnel area are shown in Figs. 16 and 17. Specifically, Fig. 16 shows the four-receiver arrangement for the pattern tests, while Fig. 17 shows the two-antenna arrangement employed in the breakdown studies.

The actual dielectric test section is hidden in these photographs by the translucent polyethylene bag extending from the nozzle to the large steel receiver tank. The presence of the polyethylene bag is a safety feature, its purpose being to maintain an inert, nitrogen-helium atmosphere around the outside of the dielectric test section. In the event of possible accidental puncture of the test section wall from within, by a ricochetting metallic diaphragm fragment, for example, the influx of external inert gas to the predominantly hydrogen atmosphere existing in the shock tunnel following a run would not present an explosion hazard as it would in the case of an influx of air. The bag itself, upon collapsing following a puncture, would also provide a temporary seal while the normal post-run tunnel purging procedure is continuing. The presence of the bag has been shown not to be detrimental to the conduct of microwave experiments.

The freestream nozzle flow was monitored during the tests by means of an X-band interferometer, located at about the 15-inch diameter station of the nozzle. The interferometer hardware on the transmitting side is shown in Figs. 16 and 17. While the precise interpretation of microwave interferometer data in terms of electron concentration requires the use of assumptions which have not yet been adequately justified, the use of the interferometer here was primarily to give assurance that the test flow was free of contamination rather than to provide a demonstration of the closeness of accord between interferometer measurements in the present tunnel plasma geometry and theoretical predictions. Theoretical estimates of the amount of X-band phase shift were made using the computed flow conditions at the interferometer station (Figs. 1 and 2). The freestream was considered a pure uncontaminated airflow provided the measured shift was in reasonable

agreement with this result, in view of the effects of uncertainties in reaction rates, effective plasma path length, plasma boundary curvature, boundary layer electron concentration gradients, etc. It may be noted that the free-space interferometer technique is usually considered favorable when the dimensions of the plasma are greater than the beam width and wavelength of the electromagnetic radiation and the measurements are essentially limited to frequencies greater than the plasma frequency, i.e., the approximate analysis usually invoked for the interferometer technique is most nearly correct when

$$\omega^2 > \omega_p^2$$

$$\omega^2 > (c/D)^2$$

where $c$ is the speed of light and $D$ is the characteristic dimension (diameter) of the plasma. The first condition permits a convenient simplification by viewing the plasma dielectric properties as a small local perturbation to a free-space system and the second is essentially a diffraction condition which permits reducing the problem of propagation to a ray-tracing problem with a plane-wave model as a first approximation. Typical tunnel operating conditions herein, where the interferometer was used, were such that $\omega^2/\omega_p^2 \sim 250$ and $\omega^2/(\frac{c}{D})^2 \sim 3250$ for $D \sim 30$ cms. The use of an interferometer seems reasonable under these circumstances.

### 3.4 Test Model

The model employed in the experimental studies was a 12-inch diameter hemisphere-capped cylinder which has been used in previous programs at CAL for the Air Force Cambridge Research Laboratories.* A schematic diagram of the model installation in the shock tunnel is shown in Fig. 12.

#### 3.4.1 Antennas

The model is equipped with one X-band waveguide antenna, one C-band waveguide antenna, and three S-band waveguide antennas. The

*Under Contract AF 19(604)-8494.

long dimensions of the X- and C-band slots are oriented axially and located on opposite sides of the model, each slot centered 4.75 inches aft of the model shoulder. Two of the S-band antennas are located on the cylindrical afterbody, the slots positioned one behind the other with their short dimensions parallel to the flow direction (transverse orientation) and with their centers 2.5 inches apart. The center of the upstream S-band antenna aperture is 6.4 inches aft of the model shoulder. The third S-band antenna is located at the nose of the hemisphere-cylinder model. In the experimental studies to be discussed, neither the X-band antenna nor the nose region S-band antenna was employed.

### 3.4.2 Pressure and Heat Transfer Instrumentation

In order to verify the test conditions during the experiments, the hemisphere-cylinder model was instrumented both surface heat transfer and pressure measurements. Heat transfer to the model stagnation point is proportional to $H_o \sqrt{p_{STAG}}$ and its calculation, based upon the measured stagnation point pressure, $p_{STAG}$, provides a check on the total enthalpy, $H_o$, of the flow. Similarly, since $p_{STAG} \sim \rho_\infty H_o$, the measurement of pressure and heat transfer at the stagnation point affords a check on the local density, $\rho_\infty$, of the freestream flow. The location of the surface instrumentation is indicated in the accompanying Table 3. Both the angular ($\theta$) and surface distance (S) locations of the hemispherical nose instrumentation are indicated, the latter distance being normalized by the nose radius $R_b = 6$ inches.

Table 3

CRL MODEL INSTRUMENTATION

| Pressure | | Heat Transfer | |
|---|---|---|---|
| $\theta$ | $S/R_b$ | $\theta$ | $S/R_b$ |
| 0° | 0 | 15° | .244 |
| 22.5 | .392 | 30 | .524 |
| 37.5 | .654 | 45 | .786 |
| 67.5 | 1.178 | 60 | 1.048 |
| 90.0 | 1.570 | 75 | 1.310 |
| | 1.924 | | 1.800 |
| | 2.924 | | 2.426 |
| | 3.924 | | 3.426 |
| | 4.924 | | 4.426 |

### 3.4.3 Electrostatic Probes

In addition to the surface pressure and heat transfer instrumentation, several electrostatic probes were also located on the model. It should be noted that the presence of the probes was a consequence of a continuing CAL supported program on the development of electrostatic probes for flow field diagnostics. They cannot yet be used to pinpoint inaccuracies either in the computed flow field or in the results of microwave measurements. The problem of the local or point measurement of parameters pertinent to hypervelocity ionized airflows is a very demanding one. Diagnostic techniques have been borrowed from other disciplines and have often been applied to regions in which the assumptions of the original theory are no longer true. A justification, perhaps, is that even though the theory is strained, it may at least indicate trends. This is indicative of the problem for the flow conditions of interest here. There is at present no diagnostic technique that can furnish unambiguous and accurate data on the point ion number density in a high mass motion continuum plasma, as typified by the shock layer and large regions of the boundary layer on a hypervelocity-vehicle. At present, qualitative results have to suffice. The CRL model geometry and the high enthalpy flow conditions represented a satisfactory checkout environment for probe techniques and is typical of flow situations wherein point measurements of plasma properties are desired. The intention is to similarly record probe data on all high enthalpy shock tunnel programs and to revise the interpretation of such data in pace with the development of suitable theoretical treatments.

One probe was installed flush with the surface at the nose of the model and two probes were located diametrically opposite one another at the plane of the midpoint of the C-band antenna aperture. The probes were 90° from the antenna position. The stagnation point probe consisted of a 0.025-inch diameter collecting surface with a concentric reference electrode 0.125-inch inside diameter and 0.250-inch outside diameter. Both electrodes were copper and the insulation was Teflon. The side probes were 0.005-inch diameter copper wire, 5 mms long, and extended, therefore, only into the boundary layer on the model. Each probe was insulated by means of 0.125-inch

diameter Teflon plugs from the model wall which served as the reference electrode. All probes were DC biased to collect the positive ion saturation current.

Additional electrostatic probe instrumentation was provided by the use of a rake consisting of 5 small probes of 0.004-inch tungsten wire, each mounted in an insulating quartz holder. The probes were of similar design to those employed by French[9] and were installed in a sharp wedge of 2.5-inch span, 1/4-inch thick. The probe spacing was 1/2 inch with the probe tip 1 inch out from the sharp leading edge of the wedge. The quartz was fused onto the tungsten wire near the tip leaving about 1/4 inch of the wire exposed and the resultant cylindrical wire surfaces were aligned parallel with the flow. The rake was mounted in a vertical position over the model cylindrical afterbody with the nearest probe two inches above the model surface. The plane of the probe tips was 8.5 inches aft of the model shoulder. All the probes were operated at +6V to collect electron saturation current. Again, as with the model mounted probes, the aim was to acquire additional experience in the use of electrostatic probes for flow field diagnostics. The probe measurements were, in fact, piggyback experiments which took advantage of the plasma test environment provided by the current tests.

# IV. EXPERIMENTAL PROGRAMS

## 4.1 Aerodynamic and Environment Calibration and Purity of Airflow

At the outset of the entire program, a preliminary determination of the test conditions for the experiments was made, based upon the results of flow field microwave propagation calculations of the type described in Section II. A test condition was assumed, typical of high-enthalpy tunnel operation, such that the corresponding theoretical estimates for the loss in transmitted signal strength for propagation through the afterbody shock layer were appreciable, i.e., of order -15 to -20 dB or so, yet within the -25 dB range of the receiving equipment. Accordingly, an incident shock Mach number, $M_i = 9.3$, was proposed with the resultant reservoir gas, at 10,000 psi pressure, expanded into the test section through a 1.36-inch diameter nozzle throat.*

Prior to the commencement of the pattern tests (Phase I) and the breakdown tests (Phase II), the quality of the freestream flow with respect to flow uniformity, core size, cleanliness, etc. was investigated in a preliminary program of experiments. The tunnel conditions were those assumed above for the initial theoretical investigations. The aerodynamic calibration was performed using a 4-ft. diameter steel test section in place of the dielectric test section, and the airflow calibration consisted of pitot pressure profile measurements at several axial locations in the test section. The results indicated good quality freestream conditions. Typical pitot pressure surveys from this calibration are shown in Figs. 18 and 19 for pitot rake positions 4 ft. and 6 ft, respectively, downstream of the 3-ft. diameter exit plane of the conical nozzle. The inviscid core diameter is seen to be approximately 32 inches and 28 inches, respectively, at these two stations. The higher pressures measured by the

*As it developed, however, the above tunnel conditions in actual experiment were found to result in complete blackout of the transmitted 4.25 GHz CW signal. The test conditions were later modified to achieve transmission and all the theoretical calculations were subsequently repeated for the actual conditions of the tests. These repeat calculations are those described previously in Section II.

outer gauges on the pitot rake at the 6-ft. station (Fig. 19) indicate the detections of the oblique shock wave which is a part of the wave system establishing the flow in the cylindrical test section. When installed in the shock tunnel, the nose of the CRL model was at the 4-ft. station in the test section and remote freestream wave phenomena did not affect the local flow over the model. Subsequent use of a smaller nozzle throat for the microwave tests than the 1.36-inch diameter throat used in the airflow calibrations would not reduce the test core diameter by more than about 6 inches.

The purity of the freestream plasma flow was inferred from measurements made by means of an X-band interferometer centered at the 15-inch diameter nozzle station. A simplified block diagram of the microwave interferometer, with which transmitted and received signals are compared in amplitude and phase, is shown in Fig. 20. The signal from the klystron oscillator is fed to the transmitting horn antenna through standard X-band waveguide, and a portion of this signal is diverted by the 10 dB directional coupler and added to the received signal in the 3 dB coupler. The detected signal at ② is equal to $\left| \frac{\vec{a}}{\sqrt{2}} - \frac{j\vec{b}}{\sqrt{2}} \right|$, where $\vec{a}$ is the reference signal and $\vec{b}$ is proportional to the received signal. The bridge is initially balanced (without plasma present) by adjustment of amplitude of $\vec{b}$ with the precision attenuator and phase of $\vec{a}$ with the calibrated phase shifter to yield $\vec{a} = -j\vec{b}$, or zero signal amplitude at ②. If the signal attenuation through the plasma is insignificant, the voltage at ② provides a measure of the phase shift through the plasma. Signal attenuation was checked by measurement of output voltage at ④, which is proportional to the received signal. The bridge frequency is measured at ③ and any reflected signal is detected at ①.

Initial experience with the interferometer on the monitoring of high-enthalpy tunnel flows, well prior to the current program, indicated that the freestream electron number density at the interferometer station was much higher than predicted from corresponding nozzle solutions which assumed a pure airflow. The high electron density was believed to be the result of ionization of impurities of unknown source or nature in the air. The contamination was, in fact, sufficient to cause apparent blackout (i.e., attenuation

greater than 20 dB) of the 9 GHz bridge frequency in nozzle flows of pure nitrogen. Fig. 21 shows amplitude-phase (②, Fig. 20) interferometer records in both nitrogen and air flows at an incident shock Mach number of 9.5. The smooth plateau in the traces represents complete attenuation (i.e., attenuation > 20 dB) of the incident signal. The peak in the traces which occurs just prior to the plateau represents phase shift at incomplete attenuation. The signal attenuation rises rapidly during the initiation of flow in the nozzle, but provided some signal traverses the plasma, a change in phase from the reference signal can be recorded. When the signal attenuation later decreases sufficiently to again allow some propagation through the plasma, phase shift may then be recorded which again results in a peak in the profile as the attenuation falls off. On observation of similar behavior in the abrupt onset of transmission cutoff in direct attenuation measurements, Talbot[10] concluded that this indicated little refractions of the incident radiation through the less dense (boundary layer) regions of the flow.

A rigorous program of cleaning was instituted to reduce the contamination problem. The driven tube was cleaned by pulling many passes of a tight-fitting lint-free cloth swab through the tube, using both absolute alcohol and perchlorethylene as the cleaning agents. The throat station was also thoroughly cleaned, following its actual removal from the tunnel for this purpose. This careful cleaning of the driven tube and throat assembly was accomplished before each run. The possible effects on flow contamination of such variables as the amount of cleaning, level of driven-tube evacuation pressure, use of brass versus mylar throat diaphragm, presence of the centerbody plug assembly, pressure, shock speed and throat size were all investigated. The centerbody assembly houses a plug which closes the tunnel throat after the reflected shock-processed, or reservoir, gas has entered the nozzle and prevents the passage of any fragments of the main metal diaphragms from entering the nozzle. While the airflow was cleaned to an extent which indicated freedom from contamination, the program was not carried to a stage permitting a specific quantitative determination of the net effect of each of the above variables. The results indicated, however, that the use of the centerbody does not contribute to flow contamination nor, most probably, does the use of a mylar throat diaphragm. The careful cleaning of the driven tube and throat assembly prior to each run is probably the most important operation to ensure the maintenance of adequate purity

airflow. Adherence to the above cleaning procedure rendered the nozzle freestream flow apparently free from the effects of contamination. Measurements of the phase shift, $\Delta\phi$, from interferometer records of the type shown in Fig. 22 were found to be in very good agreement with values calculated at the interferometer station from the corresponding nozzle flow solution (e.g., $\Delta\phi_{meas.} = 12°$, $\Delta\phi_{calc.} = 8°$).

## 4.2 Antenna Pattern Studies

The antenna pattern studies were conducted at a frequency of 4.25 GHz. The model was sting mounted in the dielectric test section (Fig. 12) and rotated so that the normal to the C-band antenna aperture was parallel to the floor. The antenna normal was taken as the roll plane 0° reference position for the external antennas as indicated in the accompanying sketch. Four dipole receiver antennas were mounted on the wooden arch at angular positions 0°, 45°, 90° and 135°. A general view of the equipment arrangement for the pattern tests is shown in Fig. 16.

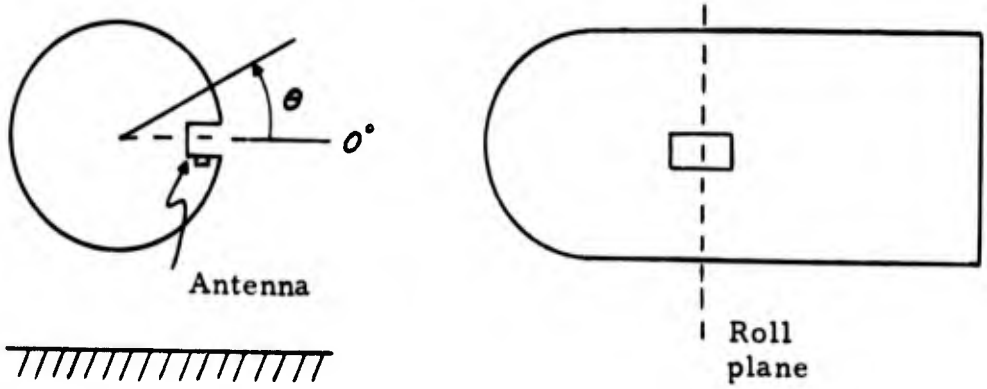


### 4.2.1 Microwave Instrumentation for the Pattern Tests

A block diagram of the microwave instrumentation used to study plasma-induced distortion of antenna radiation patterns is shown in Fig. 23. The instrumentation consisted of a C-band transmitter and four receivers, which enabled measurement of microwave signal attenuation at four arbitrary locations exterior to the dielectric test section. The C-band transmitting antenna was mounted on the model and provision was made for recording the antenna voltage standing-wave ratio (VSWR) during the tests.

The microwave power requirement for the experiments was estimated by summing the power losses between the TWT amplifier output and receiver input and by subtracting receiver sensitivity. Losses, excluding signal spreading loss, are tabulated in Table 4. Note that, in the estimate, a 30 dB allowance is made for signal attenuation. The receiver technique relies upon measurement of the average received signal power; therefore, a 3 dB allowance should be made to account for the difference between peak and average power of the 50% duty factor modulation.

Table 4

TABULATION OF MICROWAVE LOSSES

| | Insertion Loss in dB |
|---|---|
| Coaxial cables and connectors | 5.0 |
| Isolator | 1.0 |
| Dual directional coupler | 1.0 |
| Transmitting antenna | -4.0 |
| Receiving antenna | -4.0 |
| Maximum signal attenuation | 30.0 |
| Modulation loss | 3.0 |
| | 32.0 |

A spreading loss, $\lambda^2/(4\pi)^2 R^2$ of 49 dB was computed by assuming a typical maximum transmitter-receiver antenna separation, $R$, of 5 feet and a frequency of 4.25 GHz. Addition of this spreading loss to the 32 dB loss calculated above yields a total signal loss of 81 dB. A receiver sensitivity of -43 dBm was assumed, which therefore resulted in a microwave power requirement of 6.3 watts.

Special microwave compression receivers were loaned to the program for the radiation pattern measurements. The receivers were designed and fabricated by CAL under Contract 4804, Suborder 7 with the Sandia Corporation and, together with the associated oscilloscope displays, provided an experimentally measured dynamic range capability in excess of 30 dB for the tests. The large dynamic range capability was deliberately designed into the instrumentation to account for possible wide variations of test conditions from

test to test and for a priori uncertainty in conditions during a given test. The receivers have a bandwidth of 100 KHz and can respond to very rapid signal fluctuations during the test.

A block diagram of the compression receiver is shown in Fig. 24. The 2 MHz modulation is detected and amplified in several bandpass amplifier stages. Signal saturation occurs in successive stages, beginning with the last stage first, as the input signal level is increased. Output voltages of each stage are detected, filtered, and summed, providing a DC voltage level which is a nonlinear function of the amplitude of the microwave signal at the receiver input. A plot of DC voltage at the receiver output as a function of the microwave signal level at receiver input for a typical receiver is shown in Fig. 25.

### 4.2.2 Evaluation of the Dielectric Test Section for Pattern Measurements

The electrical properties of the dielectric test section and environmental reflections will modify the antenna-model free space radiation pattern. Thus, it is of particular interest to compare radiation patterns taken under the following conditions: 1) outdoor antenna range, 2) measurements made in situ in the shock tunnel with the dielectric test section removed, 3) measurements made in situ with the test section in place in the tunnel.

Radiation patterns taken in the roll plane under the above conditions are shown in Fig. 26. The dashed curve shows the pattern taken on the outdoor antenna range and the circles correspond to the case of the model sting mounted in the shock tunnel, but with the dielectric test section removed. The solid curve is the pattern taken under similar conditions with the dielectric test section reinstalled in the tunnel. From these patterns, it is concluded that nearly all the measurement error is due to the dielectric test section and that negligible error is contributed by external environmental reflections. The results show, moreover, that radiation patterns measured about a model antenna do not differ from the free space pattern by more than 1 dB for roll angles up to 80°, disregarding any additional effects due to plasma.

Also, a lateral movement of the model ±1 inch was found to change the pattern by ±1.5 dB or less under the above conditions. In summary,

the errors in measurement resulting from test section and environmental effects are small enough to be ignored for the investigations of this program.

### 4.2.3 Experiments

The first experiments on C-band (4.25 GHz) transmission through the afterbody shock layer were performed at the total enthalpy level established by an incident shock Mach number of $M_i = 9.3$. This condition was that proposed as a result of the theoretical estimates for the magnitude of transmission loss as discussed in Section 4.1. Under these conditions, however, it was found that no receiver response was observed and that the incident radiation was almost completely reflected back into the transmitting antenna. Several additional runs were made at successively reduced levels of total enthalpy corresponding, specifically, to incident shock Mach numbers of 8.6, 8.2 and 7.7. In all cases, no signal at all was received by the dipole antennas at the 90° and 135° positions. In addition, the run at $M_i = 8.6$ also resulted in no measurable signal at the 0° and 45° receiving antennas. The incident and reflected power oscilloscope records for this latter case are shown in Fig. 27. Also indicated in the figure are the received signals for the 0°, 45° and 90° receiver antennas. The received signal level immediately following the starting shock in these records (i.e., after 1.5 msec) is at least -25 dB relative to the pre-shock level. Momentary recovery of the microwave signal did occur during the test flow, however, at the 0° and 45° antennas in the runs at $M_i = 8.2$ and $M_i = 7.7$. The received signals at these two antenna locations for the $M_i = 7.7$ run are shown in Fig. 28. The signals are seen to be quite widely fluctuating during the test flow. The approximate mean levels of the signals represent a change in signal attenuation of order -14 dB and -20 dB, respectively, for the 0° and 45° antenna positions. The X-band interferometer, meanwhile, indicated the freestream airflow to be uncontaminated throughout all these runs.

The useful test flow over the model commences, consistently, about 2.4 to 2.6 msec after the start of the trace sweep in the oscilloscope records and continues for about 0.5 to 0.6 msec. Characteristically, in all microwave records, an immediate loss, or even complete attenuation, of the

transmitted signal strength occurs as the nozzle starting shock moves over the antenna. This occurs about 1.5 msec after the start of the trace in the oscilloscope records. The starting shock moves through the test section in advance of the quasi-steady test slug of gas and is separated from it by other wave phenomena responsible for the matching of conditions between the test gas and the nonsteady post-starting shock conditions. During this interval, the apparent electron number density may be quite high. In some cases, the receiving antennas may indicate an apparent blackout condition existing from the arrival of the starting shock right up until the arrival of the test slug. The term "blackout" has been used herein to describe the situation where, within the sensitivity of the receiving equipment, the receiver response does not indicate any transmitted radiation. In other cases, partial or complete recovery of the free space level signal may occur prior to arrival of the useful test gas. The reason for the apparent high electron number density in the starting shock processed, very low pressure nozzle gas is unknown. It is, however, a characteristic feature of shock tunnel testing, evidenced by the responses of electrostatic probes, microwave interferometers, and the microwave transmission experiments.

During these initial runs on the pattern studies, severe erosion damage occurred to the model nose heat-transfer instrumentation which rendered the gauges inoperative after the first hundred microseconds of flow. The source of the bombardment was considered to be particles from the diaphragm initially located at the nozzle throat station. In the tests thus far, this diaphragm was a thin sheet (0.001 inch) of brass shim. The erosion damage to the heat-transfer instrumentation was therefore considered to have been due to the presence of brass in the core stream flow, either in liquid or solid form. It was possible, therefore, that the reflection properties of the model plasma were adversely affected by the presence of this metal. At this point in the program, the pattern tests were interrupted for an additional series of diagnostic tunnel tests, the purpose of which was to investigate the effect of using nonmetallic throat diaphragms, throat size, and off-axis mounting of the model on the signal reflection properties and transmission loss behavior of the model plasma.

Fourteen diagnostic tunnel runs were made, during which it was determined that, while the instrumentation erosion problem was circumvented by mounting the model off the centerline when a brass shim throat diaphragm was used, off-axis mounting was unnecessary when mylar was used as the throat diaphragm, provided also that the shock-tube cleaning procedure was extended, at reasonable run intervals, to include the interior surfaces of the nozzle and dielectric test section. However, in spite of the removal of instrumentation-damaging particles from the immediate model freestream at a particular tunnel operating condition, the indicated attenuation of the incident signal strength through the afterbody shock layer remained considerably higher than predicted.

Further tunnel runs were made at an incident shock Mach number of order 8.5 employing smaller nozzle throat diameters in order to reduce the freestream density level and, hence, the electron number density in the body flow field. Also, at this stage in the experiments, the model was rotated 90°, so that the normal to the model antenna aperture was perpendicular to the floor. The external receivers, however, were left in their original positions. The angular observation of the antenna field was thereby reduced from 135° to 90°. The reason for the change was two-fold: first, the new receiver positions at +45° and -45° provided a check on the uniformity of the flow and, secondly, the demonstrated influence of the dielectric test section in perturbing the free space pattern at roll angles larger than 80° to 90° (by up to 5 dB at 150°) would make it difficult to interpret, unambiguously, the data recorded by a receiver antenna 135° from the transmitting slot. Following this change, however, it was found necessary to reduce the initial 1.36-inch throat diameter by about half before satisfactory signal attenuation measurements could be obtained. At a throat diameter of 0.964 inches, in fact, the afterbody plasma still resulted in almost complete blackout of the incident radiation. At throat diameters of 0.66 inch and 0.5 inch, however, the body generated plasma condition was such that useful records were obtained of the signals received by all four of the external antennas. The Phase I pattern tests were concluded by performing repeat runs at each of these two throat diameters.

The recorded response of the receiver antennas during two repeat shock-tunnel runs at an incident shock Mach number of 8.5 are shown

in Figs. 29 and 30. In both cases, the throat diameter was 0.66 inch. The corresponding incident and reflected power records measured at the model C-band transmitting antenna are shown in Fig. 31. The second series of theoretical calculations, which are those discussed in detail in Section II, were performed for this test condition. The receiver signals recorded during two repeat runs with a 0.5-inch throat are shown in Figs. 32 and 33. The oscilloscope recording the 90° antenna signal triggered again later on in the flow in Fig. 32, which accounts for the double trace. The corresponding incident and reflected power measurements recorded at the transmitting antenna during these two runs are shown in Fig. 34. The incident shock Mach number for these 0.5-inch diameter throat runs was also 8.5.

The signal (channel 18) appearing on the bottom of the record for the $\theta = -45°$ antenna in Fig. 29 is the model surface pressure in the vicinity of the stagnation point which was included in these records to indicate the establishment of quasi-steady test flow over the model.

### 4.2.4 Experimental Results and Discussion

#### 4.2.4.1 Pattern Studies

The results of the Phase I pattern studies are determined from measurements of the experimental records of Figs. 29 to 34. By way of introduction, several general remarks are appropriate, however. The received signals obviously fluctuate quite rapidly with time from the moment the starting shock moves over the antenna. The reason for these fluctuations is not clear. The pressure and heat-transfer measurements, while reflecting a lower frequency response capability, do not indicate any appreciable variation in the steadiness of the local flow. These rapid fluctuations do not then allow more than an indication of an average effect of the plasma on signal transmission during the test portion of the overall tunnel flow. As mentioned previously, the useful or steady-pressure test flow is established about 1 msec after the starting shock moves over the model, or about 2.4 to 2.6 msec after the start of the trace in the oscilloscope records. Reference may be made here to the pressure records accompanying the external receiver signals of Figs. 29, 32, and 33.

The corresponding receiver records of Figs. 29 and 30 taken during the two 0.66-inch throat runs appear very similar and indicate quite good reproducibility of the test conditions. When the signal trace excursions are interpreted according to the indicated calibration levels, however, where 0 dB corresponds to the no-plasma case measured with the model in the dielectric test section (Fig. 26), the signal attenuations for the records of Fig. 29 are seen to be about 4 dB greater than those of Fig. 30. There is some evidence also of local plasma nonuniformity around the model when the ±45° antenna position records are compared in Fig. 29. It is not possible to estimate, however, to what extent the inhomogeneities in the test section wall, discussed earlier, contribute to the slight difference in the mean signal level for these two antennas. During both these runs, the power reflected back into the antenna aperture remained high for almost the entire duration of recorded flow over the model, following the starting shock. The percentage power reflection during the test has been estimated from the records of Figs. 31 and 34 by taking the ratio of the peak-to-peak amplitude to the maximum amplitude, observed during the time of complete signal attenuation, which was taken to represent the condition of maximum power reflection. The brief instances of reduced power reflection evident in the records correlate exactly with the peaks (signal recovery) in the receiver antenna records (e.g., Fig. 29, $\theta = 0°$; and Fig. 31, $M_i = 8.52$).

The signals received by the four receiver antennas during the two 0.5-inch throat diameter runs are shown in Figs. 32 and 33, where the indicated calibrations are referred to 0 dB for the no-plasma case. These records, also, indicate a slightly lesser reduction in the transmitted 4.25 GHz signal strength for one of the runs, namely those of Fig. 33. The differences in the mean received signal level of corresponding antennas in these two figures is quite distinct and amounts to about 5 dB. The reflected power measurements are also consistent with the observed differences in signal attenuation for these two runs. Fig. 34 shows that little power is reflected from the plasma during the $M_i = 8.53$ run of Fig. 32 throughout the entire period of the useful test flow, actually, from 0.7 msec to 1.5 msec following the arrival of the starting shock.

These differences in the mean received signal levels must be taken as indicative of the overall repeatability of the plasma environment generated about a body in the shock tunnel. The initial shock tube pressure conditions set prior to a run may be repeated to good accuracy for each run. In the present program, for example, the initial hydrogen driver tube pressure was within 20 psi of the nominal 14, 300 psi pressure and the initial driven tube air pressure was set to 16 ±0.05 psi for all the experimental runs. Such occurrences, however, as variations in the diaphragm rupturing process from run to run result in the measured slight variations in incident shock Mach number. These, in turn, may cause a 1% to 3% variation in the reflected shock, or reservoir, pressure and hence in the local gas and electron number density in the model flow field.

The plasma attenuation, given by the difference between the receiver response with and without plasma about the model, as recorded by the four external receivers during the 4.25 GHz pattern experiments, is summarized in the polar plots of Figs. 35 to 38. The mean level of signal attenuation during the test flow is indicated by the filled-in symbol on the plots. The no-plasma antenna pattern, measured with the model in place in the dielectric test section (Fig. 26), is also indicated in these figures. The theoretically predicted signal attenuation for the 0° antenna position in the 0.66-inch throat runs, taken from Fig. 9, is also shown in Figs. 35 and 36. Both the free space and approximate ground plane calculations are given.

The microwave measurements show that, in all cases, the signal attenuation increases with angular departure of the external receiver from the transmitting antenna aperture normal or 0° position. In the 0.66-inch throat tests, Figs. 35 and 36 indicate that the 4.25 GHz signal attenuations measured, respectively, at the 0°, 45°, and 90° receiving antenna positions vary from 11 - 15 dB, 20 -23 dB, and 25 - 28 dB below the no-plasma values. Furthermore, the signal attenuation for normal propagation is seen to be about 7 - 11 dB greater than that predicted by the approximate ground plane solution. As discussed earlier in Section 2.6, however, the analytical model employed in the propagation calculations is an approximate one, and one of the approximations is that the change in antenna impedance due to the plasma has not been

taken into account. The resulting mismatch, in the real case, causes an increase in the amount of power reflected and hence a reduction in the transmitted power. For example, the theoretical reflection coefficient at the C-band transmitting antenna location for the free space-plasma propagation calculation is shown in Fig. 9 to be -10 dB, i.e., only one-tenth of the incident power is reflected from the plasma. Although satisfactorily detailed reflection calibration curves were not obtained, the approximations discussed earlier were used to evaluate the experimental measurements of Fig. 31. This evaluation indicates that upwards of 80% of the incident power is reflected back into the antenna. The measured reflected power may be used to indicate a rough correction for the discrepancy between the theoretical and experimental loss in signal strength at the 0° position in Figs. 35 and 36. Since of the order of 80% of the antenna, or source, power is reflected, only 20% of the antenna power actually gets into the plasma, i.e., the power measured at the receiver output is already 7 dB down, due to reflection losses alone, apart from any additional absorption losses within the plasma. The predicted attenuation values shown in the figures could therefore be increased by at least 7 dB to account for mismatch effects, bringing them into closer accord with measured values. In the case of the microwave transmission experiments performed with a 0.5-inch throat, Figs. 37 and 38 illustrate that the observed signal attenuations at the 0°, 45°, and 90° antenna locations, respectively, range from 1 - 2 dB, 1 - 5 dB and 4 - 9 dB below the no-plasma values. No corresponding theoretical estimates were made for this particular test condition.

The occurrence of such large power reflection was not anticipated in the present program and the reflection coefficients could not be measured sufficiently accurately with the instrumentation provided. These results emphasize the need for an improved technique of measurement of high values of reflected power in future investigations. Currently, an analytical-numerical study of the calculation of the self-admittance of an antenna immersed in a plasma is being made at CAL which will permit refinement of the ground plane solution to take reflection losses into account and therefore provide much improved correlation of theoretical and experimental results on microwave propagation through such plasmas.

#### 4.2.4.2 Electrostatic Probes

Owing to probe damage sustained as a result of particle bombardment encountered in the beginning of the pattern tests, little worthwhile data was recorded by the surface probe at the stagnation point of the model in these experiments. Furthermore, a theory for the quantitative interpretation of continuum hypersonic boundary-layer probe data is lacking. As a result, the electrostatic probe results are purely qualitative. Nevertheless, no gross anomalies in probe data were encountered. The probe data also indicated fluctuations in the response and very good qualitative agreement was, in fact, obtained in the temporal behavior of the probe current and the receiver response. In view of the preliminary nature of the electrostatic probe experiments, however, about all that should be stated at this stage is that probe interpretation based upon a simplified theory appropriate to the type of flow yields results consistent with the microwave results. Bredfeldt, et al[11] have indicated that probes biased to collect the positive ion saturation current as employed herein yield more reliable data than probes biased for electron collection. Following Bredfeldt, the current $i_+$ drawn by the probe is related to the ion saturation current $i_{0+}$ by

$$i_+ = F i_{0+}$$

where $F$ is a complex function of probe geometry, flow velocity and electron and ion temperatures. Based upon such assumptions as the equality of electron and ion temperatures, an expression for $F$ was obtained[11] from which a calculation and plot was made for the variation of electron number density as a function of the ion current measured by the probe. It was found that for all the tunnel runs employing a 0.964-inch diameter throat or larger, for which radiation blackout occurred, the average electron number densities indicated by the boundary-layer electrostatic probes varied from 2.5 to 8 times the critical number density for 4.25 GHz radiation ($n_{e_{CRIT}} = 2.3 \times 10^{11}\ cm^{-3}$). On the other hand, for the runs corresponding to Figs. 29 to 34, employing either a 0.66-inch or 0.5-inch diameter throat, the boundary-layer probes indicated an average electron density varying from 0.1 to 0.7 times the critical density.

The electron currents collected by the probe rake in the shock layer, assumed to be proportional to the electron number density, clearly indicated a minimum in the number density as shown also in the theoretical profiles of Fig. 5. However, the variation in the currents collected by the five probes in the rake indicated that the minimum occurred about 1 cm closer to the body surface than the number density minimum in the corresponding theoretical profile. It is premature at this point, however, to attempt a rationalization of this apparent discrepancy. These probes will continue to be used to monitor high $M_i$ airflows in the shock tunnel to gain experience in their operation and interpretation. It is hoped thereby that more reliable information on the point electrical properties of the CRL model flow field may be obtained during the forthcoming extension of the breakdown tests.

#### 4.2.4.3 Surface Pressure and Heat Transfer

The measured distributions of the surface pressure and heat transfer over the model, normalized by the stagnation point values, are shown in Figs. 39 and 40, respectively. The individual data points have been included in both plots to indicate the run by run scatter in the measurements. The solid curve in each figure is one drawn through the mean of the data at each body station. The theoretical pressure distribution obtained from the nose region and afterbody flow field calculations of Section II (Fig. 7) has also been included in Fig. 39. The pressure measured at the stagnation point on the model was within 4% of the value calculated in the bow-shock solution. The measured afterbody pressures, however, are seen to fall below the predicted distribution until, at the position of the most aft antenna on the model ( $S/R_b = 3.1$ ), they differ by a factor of two. The reasons for the discrepancy, in toto, are not complete. It is not entirely a nonequilibrium effect, since the flow-field calculations included the influence of finite-rate chemistry. The lower-than-predicted model pressures do appear, however, to typify the distributions measured, thus far, on axisymmetric hemisphere-cylinder bodies in high enthalpy conical airflows.

This behavior has been observed on the same CRL model and on one of a smaller (3-inch) diameter in another CAL shock tunnel as described in a previous report[1] on pattern studies in ionized flow fields. Since

the same type of discrepancies in the pressure distribution have been observed in different tunnels at high $M_i$, it is not considered likely that the tunnel test flow itself is the factor responsible. The airflow calibrations in the present case have, in fact, indicated good freestream flow uniformity and core size (Figs. 18 and 19). The model pressure data in themselves are also consistent in their indication of the experimental distribution. However, one correction is applicable, namely, a source flow correction to account for the effect of the continued expansion of the freestream conical flow past the model. An indication of the size of a source flow correction to the present theoretical distribution has been determined from the results of recent ideal-gas calculations for the effect of spherical source flow about hemisphere-cylinders.[12] The ideal gas source flow correction to the calculated afterbody distribution is indicated also in Fig. 39. Its effect is seen to account for most of the observed discrepancy between the theoretical and measured pressure distributions. In view of the consistent behavior in separate tunnels, it is, of course, also possible that the observed effect is partially abetted by slight imperfections in the fabrication of the model. An investigation into the implications of the lower-than-predicted afterbody pressures on the electrical properties of the afterbody plasma could not be undertaken in this program.

The heat-transfer data were measured during the 10 runs of the Phase II breakdown studies. The run-by-run measurements are seen to repeat quite well. In addition, the stagnation point values for the heat transfer were in reasonable agreement with the simplified Fay-Riddell theoretical value

$$\dot{q}_{THEORY} = 2.25 \sqrt{\frac{p_{STAG}}{2R_b}} (H_o - H_{WALL}) \times 10^{-6}$$

such that $\frac{\dot{q}_{EXPT}}{\dot{q}_{THEORY}} = 1 \pm \sigma$, where the standard deviation had the value $\sigma = 0.2$ for the 10 runs.

## 4.3 Breakdown Studies

The two afterbody S-band antennas were employed in the breakdown studies and the model was mounted so that the normal to the S-band antenna apertures was parallel to the floor.

Two microwave systems were used in the tests, namely, a high-power pulse transmitter and receiver, operated at a frequency of 2.7 GHz, and a low-power CW transmitter and receiver to monitor the signal attenuation through the plasma during the application of high-power pulses. The frequency of the CW system was 2.84 GHz and was separated by a few megacycles from the frequency of the pulse system to avoid interference. Several items of microwave equipment were loaned to the Phase II program by the Sandia Corporation under Contract 4804, Suborder 7.

Pulse signals were transmitted from the fore S-band antenna and both pulse and CW signals were transmitted from the aft S-band antenna. The pulse and CW signals were monitored by separate antennas mounted on the wooden arch surrounding the test section exterior. The dipole receiver antenna for the pulse signals was located at the 0° position and the dipole CW receiver antenna at about the 16° position. These antennas were closely spaced to ensure that the detected signals traversed essentially the same propagation path. The antenna arrangement is seen in Fig. 17 and a general view of the equipment arrangement for the breakdown tests is shown in Fig. 41.

### 4.3.1 Microwave Instrumentation for the Breakdown Tests

#### 4.3.1.1 General Functional Description

A block diagram of the pulse system is shown in Fig. 42 and the triggering sequence and RF pulse modulation waveforms are shown in Fig. 43. The transmitter provided a train of one-microsecond pulses, which were alternately switched between the two S-band antennas on the model, as indicated in Fig. 43. High-speed switching of the pulses between the antennas was effected with a solid-state, single-pole, double-throw microwave switch at the output of a pulse transmitter.

For the duration of any one test, the pulse train consisted of approximately 10 pulse pairs, spaced 100 microseconds apart, with a spacing of 20 microseconds between the pulses of each pair. The RF pulse train detected at the output of the transmitter is shown in Fig. 44. Provision was made to vary the RF pulse amplitude during a run by as much

as 10 dB (Fig. 43) and to change the average transmitter power output level from run to run. Each power excursion comprised a triangular envelope of 5 pulse pairs at about a 3 dB power level separation, and two such amplitude modulated power excursions were made during one tunnel run. Provision was also made for detecting and recording the reflected power at the terminals of both transmitting antennas, and the incident power at the terminals of one S-band antenna, as shown in Fig. 42.

The pulse receiver consisted of an antenna, located outside the test section, a crystal video detector, a linear video amplifier and ten oscilloscopes. The oscilloscopes were triggered sequentially and in synchronization with the transmitter pulse modulator so that each received pulse pair was displayed on a separate oscilloscope. The oscilloscope pulse waveforms were recorded directly by Polaroid cameras.

The pulse transmitter consisted of a low power CW source, modulators, and a high power S-band traveling wave tube amplifier. The traveling wave tube, Sperry Type STS-101*, had a maximum peak power capability of approximately 500 watts. Variation of average RF power and pulse modulation was accomplished by modulating the RF input to the tube.

During the breakdown tests, provision was also made to permit the measurement of the coupling between the two S-band antennas on the model. The system configuration employed for the coupling measurements provided a high power pulse signal to the fore antenna while a crystal video receiver, connected to the aft antenna, measured the coupled signal. Also, the external pulse receiver was used to observe the pulse signal transmitted through the plasma. In addition, a CW transmitter and receiver was included to permit the monitoring of signal attenuation, as a function of time, during the breakdown tests.

---

*The TWT amplifier was made available to the program by CAL under contract AF 30(602)-2077.

#### 4.3.1.2 Pulse Transmitter and Receiver

A block diagram of the complete RF system, including both pulse and CW instrumentation, is shown in Fig. 45. A gated low-power klystron oscillator generated a train of RF pulses of constant width, the pulse width being slightly greater than the width of a pulse pair at the transmitter output. The pulse train was then amplitude-modulated by a PIN diode modulator, in order to provide the triangular variation of pulse amplitude at the transmitter output, as shown in Fig. 43. A 2-watt traveling wave tube at the modulator output was used to amplify the output of the modulator.

A second PIN diode modulator, at the output of the traveling wave tube amplifier, formed the pulse pairs by amplitude modulation of the input waveform. The RF pulses were then applied, in turn, to the Sperry traveling wave tube amplifier, manual RF level control, and a high-power crystal switch, which switched the pulses between the two S-band transmitting antennas on the model.

Several remarks concerning the traveling wave tube amplifier are appropriate at this point. The tube had not been used for two or more years prior to the present program and its condition was uncertain. In preliminary tests of its performance, considerable effort was required to activate the tube owing to the fact it had become gassy. Extended low-voltage operation did reduce the ion level sufficiently to enable high-voltage operation of the tube with a limited degree of success. This procedure was repeated several times during the course of the program. It was recognized at the outset by both CAL and AFCRL project personnel that the condition of the tube posed some threat to the success of the program. However, owing to funding limitations and the fact that no suitable alternate RF source was available to the program, it was decided to proceed with the program as planned.

The peak power capability of the traveling wave tube, after activation, is shown as a function of frequency in Fig. 46, and typical one-microsecond RF output pulses are shown in Fig. 47. The amplitude modulation during the pulse was caused by an excessive positive ion level in the

tube. This phenomenon was aggravated by the need for operating the tube as a quasi-linear amplifier to meet the variable pulse amplitude requirements so that the levelling effect of saturation could not be used.

One-half inch diameter low-loss coaxial cables were used to connect the model to the transmitter which was located outside the tunnel. The internal pressure of the "Styroflex" dielectric cables was maintained at atmospheric pressure to avoid RF breakdown and the cables were routed to the model through a pressure plate and "O" ring air seals on the side of the steel dump tank. In order to prevent the accidental pumping of the cables down to the pre-run tunnel pressure, the cables were vented to atmospheric pressure on the outside of the tank. Type "N" coaxial connectors were used at the model and Teflon plugs and silicone grease were used to prevent RF breakdown of the air gap of these connectors. Addition of the plugs and the grease did not affect the VSWR of the connectors; this point was verified experimentally. All RF components including the directional couplers were located outside the tunnel to avoid RF breakdown problems.

The pulse signal receiver comprised a crystal video detector, a pre-amplifier, and a low impedance amplifier which was used to excite the 10 monitoring oscilloscopes. Oscilloscope sweeps were synchronized by a shift register, triggered by a pulse which preceded the first pulse pair. A typical pulse at the output of the receiver is shown in Fig. 48 and the corresponding amplitude response calibration traces, referred to 0 dB for the no-plasma case, indicate the very limited receiver dynamic range capability of approximately $\pm 5$ dB.

#### 4.3.1.3 CW Transmitter and Receiver

A low-level 2.84 GHz CW signal, derived from a klystron signal generator, was injected by means of a directional coupler into the RF transmission between the output of the crystal switch and the aft S-band antenna, as shown in Fig. 45. The CW signal was used to monitor signal attenuation during the breakdown tests and by virtue of the slight frequency separation, both pulse and CW measurements could be made, simultaneously, without mutual interference.

An independent antenna and receiver were provided for the CW measurements. The CW receiver instrumentation consisted of an RF preselector, a mixer, a klystron local oscillator, log response IF receiver, and two oscilloscopes for data display. The receiver provided a bandwidth capability of approximately 2 MHz, which was adequate for preserving the time history of signal amplitude fluctuations. The dynamic range of the receiver was approximately 30 dB.

#### 4.3.1.4 Pulse and Waveform Generator Subsystem

A block diagram of the pulse and waveform generator subsystem is shown in Fig. 49. In addition to the trigger signal derived from the operation of the shock tunnel, the master waveform generator can be activated by either a manually activated single pulse or a free-running internal trigger. This choice of operation permitted full checkout of the system prior to initiation by the shock tunnel derived trigger.

One output of the master waveform generator is used to reset the shift register and another output provides a timing pulse to the burst pulser. The burst pulse generator has a built in time delay so that the pulse train occurs at the desired time in the flow. A second waveform generator is activated by the burst pulser for the duration of the pulse train. This generator supplies timing pulses to two pulsers, identified as Pulser No. 1 and Pulser No. 2 in Fig. 49.

The first pulser determines the width and position of the first pulse of each pulse pair in the pulse train, while the second pulser determines the width and position of the second pulse of the pair. A second output from Pulser No. 1 is used to trigger the function generator and the shift register, as shown in the figure. A third output from the pulser is used to trigger the RF generator and to provide the RF straddle pulse. The shift register is reset by the reset gate and advanced by one position for each output of Pulser No. 1. Each flip-flop of the shift register provides one of the ten oscilloscope triggers. Thus, one synchronizing pulse is initiated by each output of the pulser. The function generator has a time delay adjustment, so that the modulation can be started at the desired time.

### 4.3.2 Experiments

The experiments were conducted at the same test conditions as those employed for the antenna pattern studies. This run condition was such that the 2.84 GHz CW signal suffered a signal attenuation of about 20 dB in propagating through the afterbody shock layer. The basic breakdown experiments involved the switched application of pulses between each S-band antenna with a 20-microsecond interval between each pulse of a pulse pair. In this manner, any field-induced perturbations in electron concentration in the region of the upstream antenna would have time to be convected by the flow to the region of the downstream antenna so as to coincide with the transmission of a pulse from this antenna. The fact that both S-band antennas, due to their close proximity, were essentially in the same aerodynamic plasma and hence should normally exhibit the same breakdown behavior, provided for a meaningful interpretation of the effects, if any, of plasma perturbations caused by the upstream antenna on the breakdown of the aft antenna.

In addition, during two of the breakdown test runs, measurements were made simultaneously of the coupling between the two S-band antennas. In the coupling experiments, one varying amplitude excursion of single pulses was transmitted from the fore antenna only, at a pulse repetition frequency of 10 KHz, and the energy received at the aft antenna during pulse transmission from the fore antenna was measured.

Throughout all the Phase II breakdown tests, the initation of the pulse sequence was delayed following the firing of the shock tunnel in order to ensure coincidence of pulse transmission with the development of useful test flow over the antennas.

A total of 10 runs was made in the breakdown experiments. However, the limited performance capability and reliability of the high-power microwave traveling wave tube amplifier hindered the program from the outset. During the operation of the microwave instrumentation in the tunnel, the TWT required continual manual adjustment of the focusing current to keep the helix intercept current within acceptable limits. This

requirement for manual attendance placed a severe restriction on the time the equipment could be left unattended prior to each run. This constituted a major difficulty because tunnel operating procedure requires that personnel vacate the immediate tunnel area during the ten minutes or so immediately preceding each run while the driver tube is pressurized with hydrogen. In the interim, the increased degree of tube defocusing would frequently trip system interlocks and de-energize the TWT amplifier before the test was initiated.

Residual gas within the TWT was a continuing problem requiring repeated curing of the tube through a low-voltage cycle to maintain the ion level at a tolerable value. Apparently the situation finally developed to the point where the ions effected significant defocusing of the beam. The tube employed a convergent beam and the beam entrance potential field was readily modified by the ions so that the original focus design no longer held. Such focusing modifications could cause increased beam scalloping with resultant excessive defocusing.

While attempting operation of the TWT at higher power levels, one of the diodes of the RF switch broke down. Subsequently, RF noise was observed on the system output under similar operating conditions. It is assumed that the high average power level of this RF noise caused the diode breakdown, because the duty cycle of the normal transmitted pulsed signal was insufficient to account for the diode failure. Spare diodes were on hand to permit repair of the switch as needed. The defocusing problem was circumvented by operating the tube at a reduced RF power output level. The maximum power at the antenna terminals during the tests was 140 to 150 watts.

### 4.3.3 Experimental Results and Discussion

The results of the breakdown tests may be summarized as follows. At the maximum peak pulse power of 150 watts delivered to the antenna, representing a power density of 6 watts/cm$^2$, no temporal changes in pulse shape were observed which could be attributed to the plasma alone. Changes in pulse shape with attenuation level did occur, but such shape

changes were found to be duplicated in the no-flow calibration records when pulse shape and amplitude were studied as a function of attenuator setting.

Following two successive failures of the crystal switch in attempts to maximize the pulse power at the beginning of the experiments, the first two runs with pulse power applied were performed with the pulse train applied to the fore antenna only. One useful feature in this arrangement, however, was that the displayed pulse width could be made as large as desired for pulse shape definition. Accordingly, the pulse receiver recording oscilloscopes were operated with a 0.5 $\mu$ sec/cm sweep to provide 2 cm width of the one-microsecond pulse. The second pulse of each pulse pair was not recorded in this arrangement. In the operation as originally planned, with the first and second pulse in each pulse pair transmitted from the fore and aft antennas, respectively, the received pulse display would have been recorded on the 10 cm graticule of one oscilloscope. The displayed pulse width in this case would be about 0.5 cm.

One of the pulse signals received in these first experiments has been shown previously in Fig. 48. This particular pulse is the first pulse of the fourth pulse pair in a train similar to that shown in Fig. 44. The signal attenuation in this case, as measured from the records of Fig. 48, is 21 dB, referred to 0 dB for the case with no plasma. The CW signal corresponding to this particular run is shown in Fig. 50 for two sweep speeds. The location of the start of the right trace (b) sweep in the left trace (a) of Fig. 50 may readily be identified at 2.45 msec from the start of the trace. The pulse train (Fig. 44) was initiated at the same time as the trace (b) trigger, as shown in Fig. 50. The position of the particular pulse shown in Fig. 48 is then readily identified 300 $\mu$ secs after the start of trace (b). This pulse is seen to be located about midway through the useful test time which commences 2.6 msec from the start of trace (a). At this point, the CW signal loss is 21 dB, in agreement with that measured from the pulse record of Fig. 48. As observed previously in the calibration record of Fig. 48, the dynamic range in the pulse receiver circuitry is unfortunately quite small, about 5 dB. The pre-run pulse receiver attenuator setting was such that the anticipated signal attenuation during the run would result in a pulse amplitude

about half the height of the graticule. For a signal reduction about 5 dB more or less than anticipated, the received signal was, respectively, too small for reliable measurement or off scale. Many of the signals received during the second power excursion in these experiments were, in fact, off scale as evidenced by the CW signal loss levels indicated for those times in Fig. 50(a).

At peak pulse power levels of the order of 150 watts, reasonably stable operation of the TWT amplifier was obtained and the crystal switch circuitry was employed for a total of 4 runs. However, the recording procedure for observation of the received pulse train was altered from that originally planned for these experiments. Instead of recording each pulse pair on one oscilloscope, enabling at most about 0.5 cm pulse width definition, two oscilloscopes were employed for observation of each pulse pair. Both oscilloscopes were operated at sweep rates of 0.5 $\mu$sec/cm and both were triggered from the first pulse of each pair. The second oscilloscope's sweep, however, was delayed 19$\mu$sec so as to record the second pulse of the pair. This permitted satisfactory pulse shape definition. The individual received pulses of a transmitted pulse pair are shown in Fig. 51 together with the post-run calibrations for each channel, where 0 dB corresponds to the no-plasma case measured with the model in the dielectric test section. The signal attenuation as measured at the midpoint of the pulse profile in this case was 16.5 dB. The signal attenuation determined from the CW record at this point was 14 dB. While this recording arrangement does provide for very desirable pulse shape definition, the required use of two oscilloscopes per pulse pair enabled only one power excursion to be observed since only 10 fast-sweep oscilloscopes were available. The CW records indicate, however, that the useful test flow period would only allow one such excursion in any event. The change in pulse shape referred to earlier is clearly evident in the records of Fig. 51 as well as those in Fig. 48. However, since the same trend in pulse shape is present in the calibration traces, this phenomenon cannot be attributed to plasma effects. The pulse shape distortions are probably the result of microwave equipment induced effects.

For purposes of comparison, during the same experimental run corresponding to the records of Fig. 51, the fourth pulse pair in this train was recorded in the manner originally planned. The received pulse pair is shown in Fig. 52. In this case the pulse attenuation was measured to be 22 dB while the CW signal attenuation was 24 dB, relative to the no-plasma case.

During the course of the breakdown experiments, simultaneous measurements were made in two runs of the coupling between the two S-band antennas on the model. The oscilloscope requirements were again such that only one power excursion could be observed. Pulse transmission was from the fore antenna. Two oscilloscopes were required to record the first pulse of each transmitted pulse pair, one to monitor the external receiver and the other to monitor the aft S-band antenna. Because of equipment shortages during these particular tests, however, no CW transmission measurements could be made during the coupling experiments. The direct and coupled receiver signals are shown in Fig. 53. The particular pulse shown in this figure is the first of the fourth pulse pair transmitted which had a peak pulse power of about 75 watts. The external dipole receiver signal indicates a signal attenuation of about 17.5 dB. Whereas the measured free space coupling between the two antennas was 19 dB, the signal received by the aft antenna indicates that the antenna isolation is further increased by about 20 dB in the plasma environment during a run.

None of the signal wave forms recorded during these tests indicated changes in wave shape which might be interpreted as nonlinear interaction phenomena or incipient breakdown. Unfortunately, many of the waveforms could not be observed because the signal amplitude variations exceeded the dynamic range of the receiver equipment. As noted previously, the maximum dynamic range capability of the pulse receiver and display was limited to approximately ±5 dB. The data recorded, however, provided sufficient evidence that no breakdown occurred even at the maximum available antenna power condition. The variation of the mean signal attenuation from run to run, which was approximately ±5 dB for the same tunnel initial pressure conditions as observed previously during the pattern studies, and the

variation with time during any one run (e.g. Fig. 50), indicated a receiver dynamic range requirement of 30 dB or more. Because of cost limitations, it was not possible to provide amplitude compression receivers with such large dynamic range and with adequate bandwidth for these tests. The need for larger dynamic range receivers in future breakdown tests is clearly indicated, however.

While the realized power density of 6 watts/cm$^2$ is in the range where observable nonlinear effects might be expected, it is felt that the failure to observe any nonlinear plasma interactions in the experiments was because a significant fraction of the incident RF power on the plasma was reflected. The effective power density within the plasma was therefore considerably less than that computed from available power. One of the reflected power records taken during the experiments is shown in Fig. 54, together with the calibration records obtained by shorting the antenna with a copper sheet to record maximum power reflection. The pulse peaks have been retouched in this figure for purposes of reproduction, but the record indicates that at least 80% of the incident power is reflected. The high power reflections measured in these experiments at S-band result from plasma-induced antenna mismatch which also caused the similarly high reflections at C-band in the pattern tests.

The large reflection coefficient must also have some effect on the interpretation of the coupling measurements. The coupling experiments showed that the presence of the hypersonic plasma resulted in a 20 dB or so reduction, from the free space value, in the measured signal coupled from the fore to the aft antenna. Of possible concern, however, is the ability of the instrumentation to provide a meaningful measurement of this reduction in coupled signal because of reflected power considerations. Since the RF power reflected from the plasma was high, the measured reduction in coupled signal represents the sum of the plasma-induced effects of increased reflected power and of the modification of the coupling path (i.e., free space vs. plasma) between the antennas. Because only a small fraction of the incident power is transmitted when the plasma is present, any error in determining the actual transmitted power will cause a significant error in evaluating the effects of the plasma on the coupled signal. The accuracy of the coupling measurements must await evaluation in future tests.

# V. CONCLUSIONS

An analytical and experimental study has been made of the effects of an aerodynamically generated plasma on microwave transmission from simple waveguide antennas installed on the cylindrical afterbody of a 12-inch diameter hemisphere-cylinder model in the CAL High Energy Shock Tunnel. The studies comprised signal attenuation and pattern shift measurements at C-band (4.25 GHz) and nonlinear plasma interaction and coupling measurements at S-band (2.7 GHz).

The analytical studies involved the coupled chemical-gasdynamic calculation of the entire nonequilibrium tunnel freestream and body flow fields and the resulting interaction for plane-wave propagation of microwave radiation through the afterbody plasma. The flow field calculations have afforded a valuable insight into the distributions of the electron number density and collision frequency around a body geometry of basic interest.

The shock tunnel is a facility unique in its capability to generate essentially contaminant-free high enthalpy flows for the simulation of reentry scale velocities. In the present tests, the shock tunnel has been shown to provide test flows at high total enthalpy, which are adequate ($\sim$ 0.6 msec) for the performance of plasma-microwave interaction experiments. In addition, the repeatability of the plasma environment generated about the model in the shock tunnel from run to run was such as to result in a $\pm$5 dB variation in signal attenuation at S- and C-band frequencies. The suitability of the shock tunnel for the performance of microwave experiments was enhanced by the use of a specially designed dielectric test section in order to minimize test environmental effects on the microwave measurements. In operation, the dielectric test section has proven very satisfactory in that diffraction and multipath effects are quite negligible. The test section itself has been shown to permit the duplication of outdoor antenna range pattern measurements to within about 1 dB over the entire 180° upper half-plane above the antenna.

The pattern shift studies furnished measurements of the increase in signal attenuation as the receiver antenna was rotated away from the antenna aperture normal to the 90° position. The signal attenuations measured on the antenna normal were found to exceed the predicted attenuation, while, at the same time, measurements of the reflected power showed that upwards of 80% of the incident RF power was reflected from the plasma back into the aperature. The large power reflection, a feature of both the C-band and S-band experiments, is considered to be primarily a mismatch effect which is due to the change in antenna impedance caused by the plasma. An improved accounting for RF power reflection must be included in future calculations of microwave propagation through plasmas in the vicinity of a ground plane, to ensure better correlation between theoretical and experimental microwave interaction effects. Currently, an analytical-numerical study of the calculation of the self-admittance of an antenna immersed in a plasma is being made at CAL in order to provide this necessary refinement. Obviously, improvements to theoretical approaches in areas revealed inadequate in facility experiments, will lend confidence to the prediction of interaction phenomena in flight situations which cannot be simulated in the shock tunnel.

The S-band experiments were unsuccessful in measuring any incipient breakdown or nonlinear plasma-microwave interaction effects, although the antenna aperture power levels achieved were such that nonlinear effects might be expected. Again, the plasma-induced antenna mismatch, with the attendant high power reflection, resulted in a reduction from aperture values of the power density actually within the plasma. Further experiments will be performed shortly, at considerably increased power levels, to observe S-band breakdown phenomena in the same test environment.

The complex programmed operation of all the microwave instrumentation and its operation in proper synchronization with the tunnel flow was entirely satisfactory. The program budget did not permit the use of receivers with the greater dynamic range capability (i.e., amplitude compression receivers) desired for the breakdown tests. The possible variation of plasma electromagnetic properties (electron concentration, attenuation etc.) from test to test, and the systematic changes which may occur during any one test, indicate a receiver dynamic range requirement of 35 dB, or more, for

further exploratory investigations. A considerable amount of the data collected in the present tests was, in fact, unusable because signal amplitude variations exceeded receiver capability.

During the S-band breakdown tests, measurements were made of the effect of the aerodynamically generated plasma on the coupling between two S-band antennas, situated 2.5 inches apart. The coupling measurements, performed under conditions of high reflection coefficient, indicated that the isolation between antennas was increased an additional 20 dB from the free-space value of about 20 dB, during the plasma flow. While the effect of the plasma absorption alone on the coupling was not separable from the measured loss, the net effect as measured in the present experiments resembles the flight case for a simple slot antenna where power reflection effects and plasma absorption both contrive to change the free-space coupling.

It is recognized that many factors contribute to the overall effect of an adjacent plasma on the propagation of microwave radiation from a slot antenna on a hypervelocity vehicle. Factors such as the rate of boundary layer growth over the vehicle, the curvature of the body surface or ground plane, gradients in the electrical properties of the flow over the antenna, and changes in the antenna impedance all play a rôle. It is believed, however, that comparisons of the results of experimental interaction studies of the type described herein with theoretical predictions will result in evaluation of the effects of each of these factors and further our understanding of the basic effects involved.

## REFERENCES


1. Curtis, J.T., Burke, A.F., Hayman, R.A., An Analytical and Experimental Study of the Ionized Flow Field About a Hemisphere-Cylinder and its Effect on the Radiation Pattern of a Slot Antenna. AFCRL-63-339, CAL Report No. AD-1575-Y-1, August 1963.

2. Lordi, J.A., Mates, R.E., Moselle, J.R., Computer Program for the Numerical Solution of Nonequilibrium Expansions of Reacting Gas Mixtures. CAL Report No. AD-1689-A-6, October 1965.

3. Marrone, P.V., Garr, L.J., Inviscid, Nonequilibrium Flow Behind Bow and Normal Shock Waves, Parts I, II. CAL Report No. QM-1626-A-12 (I), (II), May 1963.

4. Curtis, J.T., Strom, C.R., Computations of the Nonequilibrium Flow of a Viscous, Radiating Fluid About a Blunt Axisymmetric Body. CAL Report No. AM-2113-Y-1, Vols. 1, 2, January 1967.

5. Eschenroeder, A.Q., Boyer, D.W., Hall, J.G., Nonequilibrium Expansions of Air with Coupled Chemical Reactions. Phys. Fluids 5, 615, 1962.

6. Bachynski, M.P., Shkarofsky, I.P., Johnston, T.W., Plasma Physics of Shock Fronts. RCA Research Lab. Report No. 7-801-3, June 1959.

7. Bein, G.P., Plane Wave Transmission and Reflection Coefficients for Lossy Inhomogeneous Plasmas. IEEE Trans. on Antennas and Propagation, Vol. AP-14, 511, July 1966.

8. Bein, G.P., Boyer, D.W. Microwave Transmission in a Pure Air Plasma. AIAA Paper No. 66-173, AIAA Plasmadynamics Conference, Monterey, California, March 2-4, 1966.

9. French, J.B., Langmuir Probes in a Flowing Low Density Plasma. UTIA Report 79, AFOSR 2159, August 1961.

10. Talbot, L., Katz, J.E. and Brundin, C.L., Comparison Between Langmuir Probe and Microwave Electron Density Measurements in an Arc-Heated Low-Density Wind Tunnel. Phys. Fluids 6, 559, 1963.

11. Bredfeldt, H.R., Scharfman, W.E., Guthart, H. and Morita, T., Boundary Layer Ion Density Profiles as Measured by Electrostatic Probes. Stanford Research Institute Tech. Report 33, February 1966.

12. Inouye, Mamoru, Numerical Solutions for Blunt Axisymmetric Bodies in a Supersonic Spherical Source Flow. NASA TN D-3383, April 1966.

Table I

REACTION KINETIC DATA EMPLOYED IN NUMERICAL CALCULATIONS

| REACTION | THIRD BODY M | FORWARD RATE CONSTANT $k_F$ ($cm^3$/mole sec.) |
|---|---|---|
| 1. $O_2 + M \rightleftharpoons 2O + M$ | $O_2$ | $3.6 \times 10^{21} T^{-1.5} \exp\left(-\frac{117960}{R_o T}\right)$ |
| 2. $O_2 + M \rightleftharpoons 2O + M$ | O | $2.1 \times 10^{18} T^{-0.5} \exp\left(-\frac{117960}{R_o T}\right)$ |
| 3. $O_2 + M \rightleftharpoons 2O + M$ | $N_2$, Ar, N, NO | $1.2 \times 10^{21} T^{-1.5} \exp\left(-\frac{117960}{R_o T}\right)$ |
| 4. $N_2 + M \rightleftharpoons 2N + M$ | $N_2$ | $3.0 \times 10^{21} T^{-1.5} \exp\left(-\frac{224990}{R_o T}\right)$ |
| 5. $N_2 + M \rightleftharpoons 2N + M$ | N | $1.5 \times 10^{22} T^{-1.5} \exp\left(-\frac{224990}{R_o T}\right)$ |
| 6. $N_2 + M \rightleftharpoons 2N + M$ | $O_2$, Ar, O, NO | $9.9 \times 10^{20} T^{-1.5} \exp\left(-\frac{224990}{R_o T}\right)$ |
| 7. $NO + M \rightleftharpoons N + O + M$ | $O_2$, $N_2$, Ar, O, N, NO | $5.2 \times 10^{21} T^{-1.5} \exp\left(-\frac{149960}{R_o T}\right)$ |
| 8. $N + O_2 \rightleftharpoons NO + O$ | | $1.0 \times 10^{12} T^{0.5} \exp\left(-\frac{6200}{R_o T}\right)$ |
| 9. $O + N_2 \rightleftharpoons NO + N$ | | $5.0 \times 10^{13} \exp\left(-\frac{75520}{R_o T}\right)$ |
| 10. $O_2 + N_2 \rightleftharpoons NO + NO$ | | $9.1 \times 10^{24} T^{-2.5} \exp\left(-\frac{129120}{R_o T}\right)$ |
| 11. $NO^+ + e^- \rightleftharpoons N + O$ | | $1.8 \times 10^{21} T^{-1.5}$ |

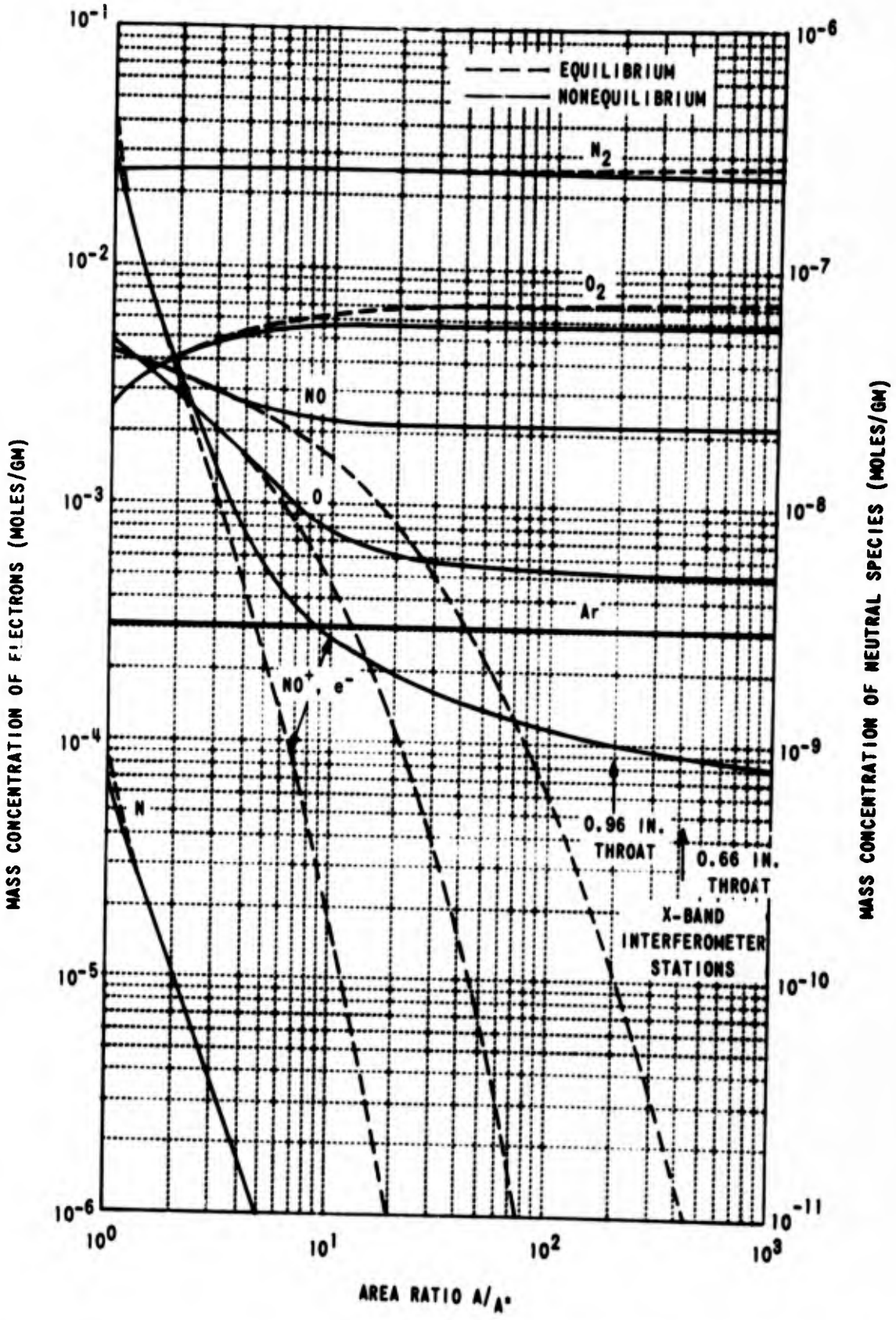


Figure 1 SPECIES DISTRIBUTIONS FOR PURE AIRFLOW IN THE CAL HYPERSONIC NOZZLE

$T_o$ = 5800°K, $P_o$ = 657 ATM

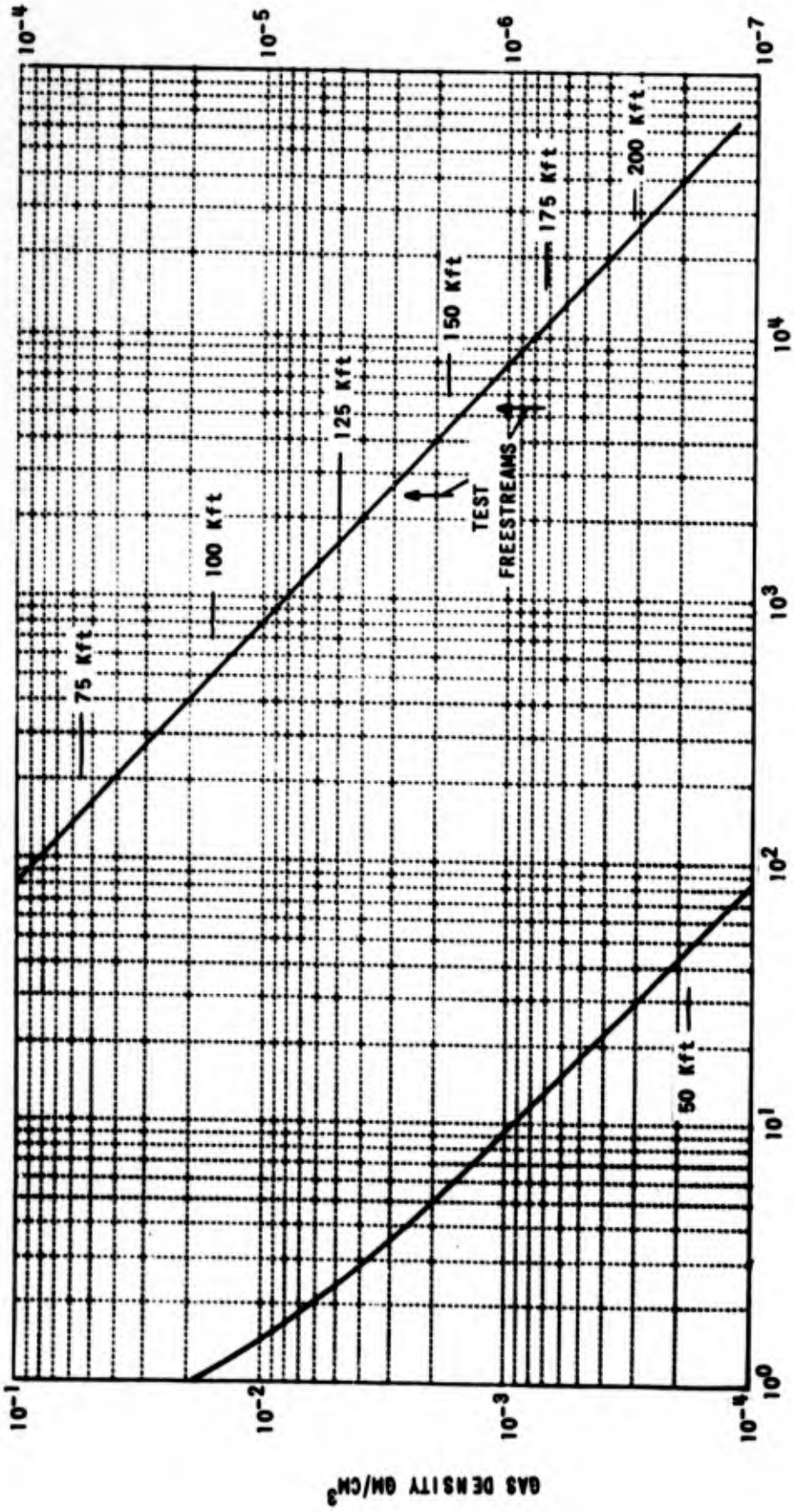


**Figure 2 DENSITY VARIATION IN HYPERSONIC NOZZLE AIRFLOW**

$T_o$ = 5800°K, $P_o$ = 657 ATM

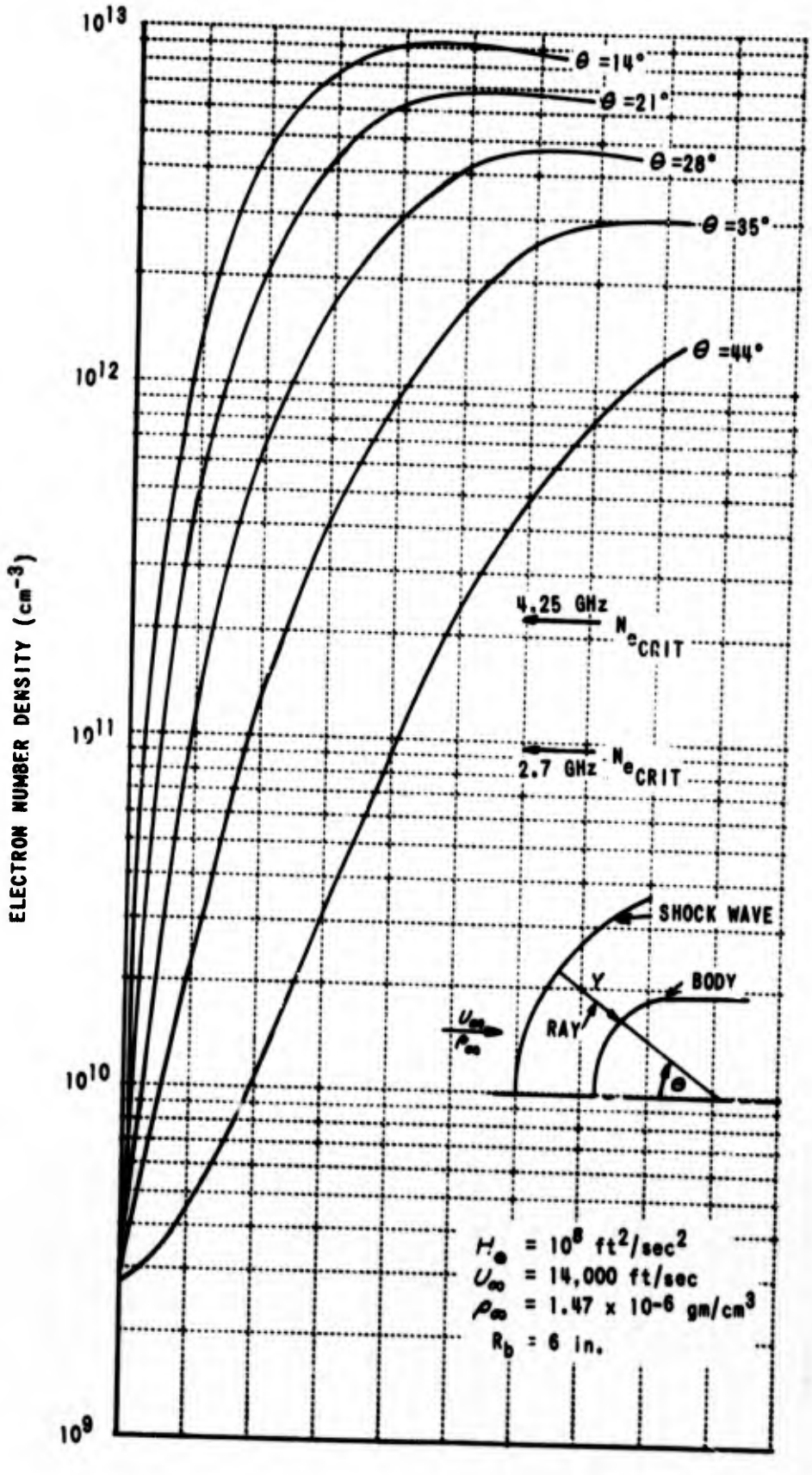


Figure 3 ELECTRON NUMBER DENSITY PROFILES CALCULATED NORMAL TO THE SHOCK IN THE NOSE REGION OF THE 12-INCH DIAMETER HEMISPHERE-CYLINDER MODEL

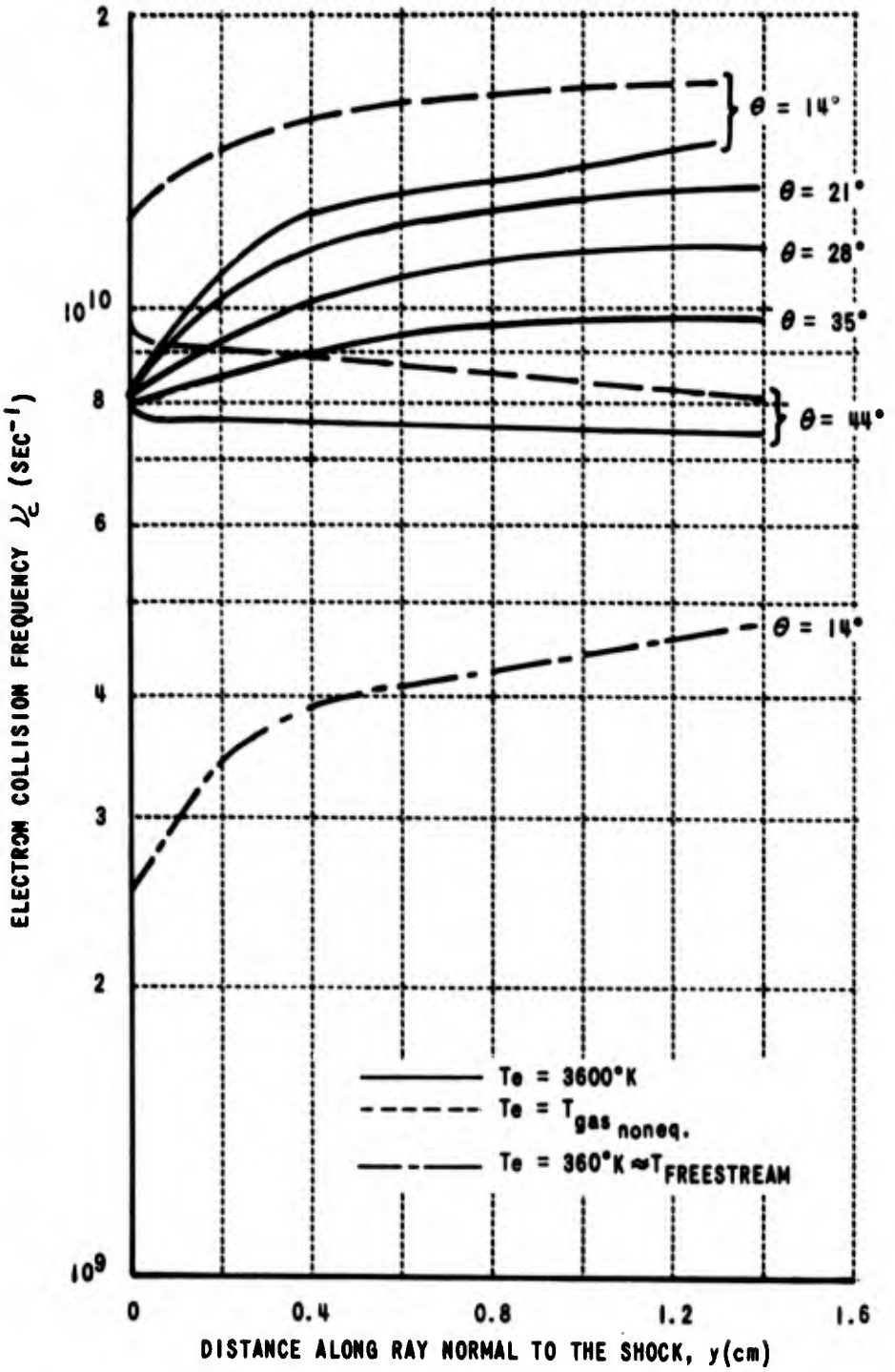


Figure 4 ELECTRON COLLISION FREQUENCY PROFILES, NORMAL TO THE SHOCK IN THE NOSE REGION OF THE HEMISPHERE-CYLINDER MODEL

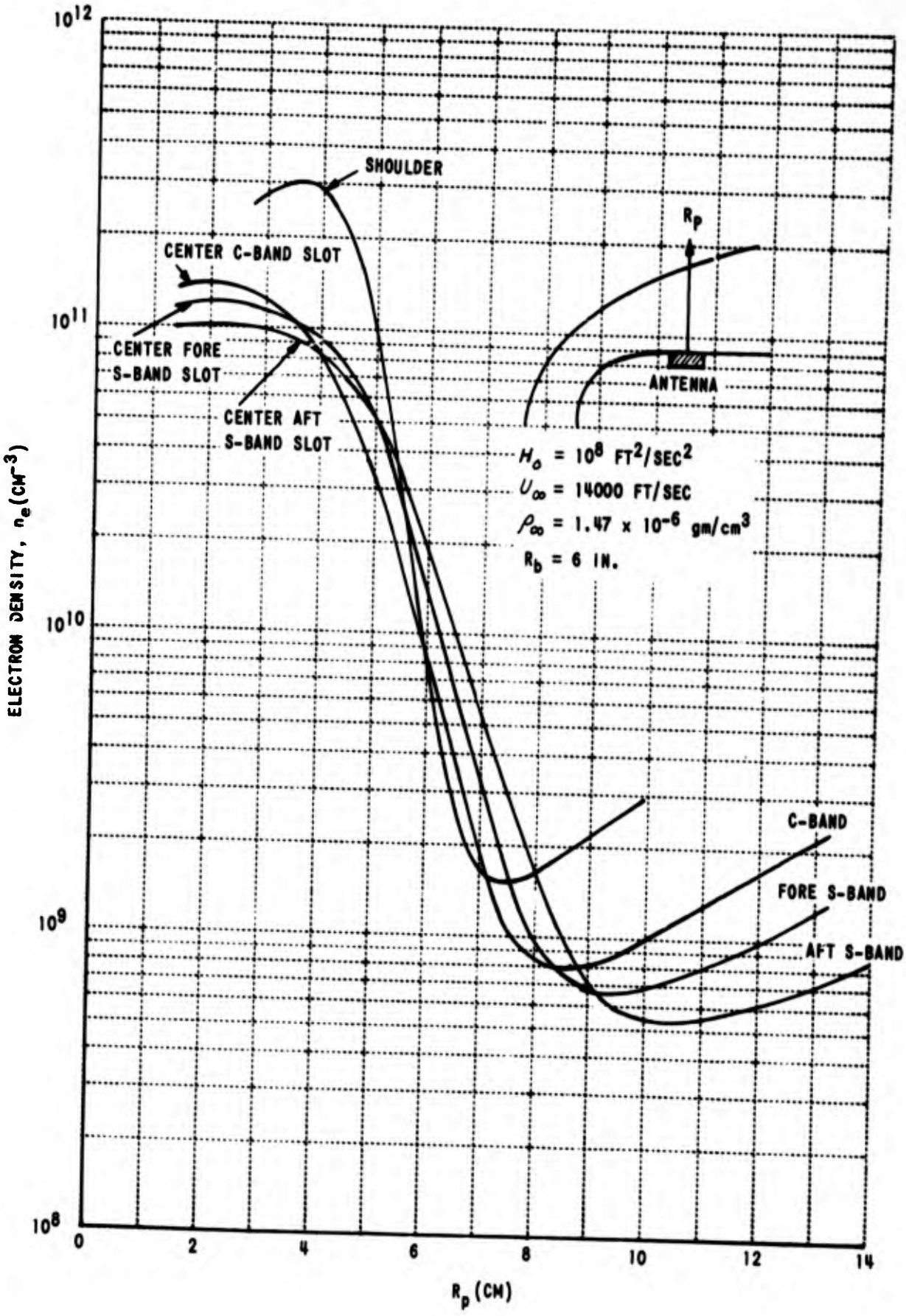


Figure 5 ELECTRON NUMBER DENSITY PROFILES CALCULATED ALONG RAYS NORMAL TO MODEL AFTERBODY SURFACE

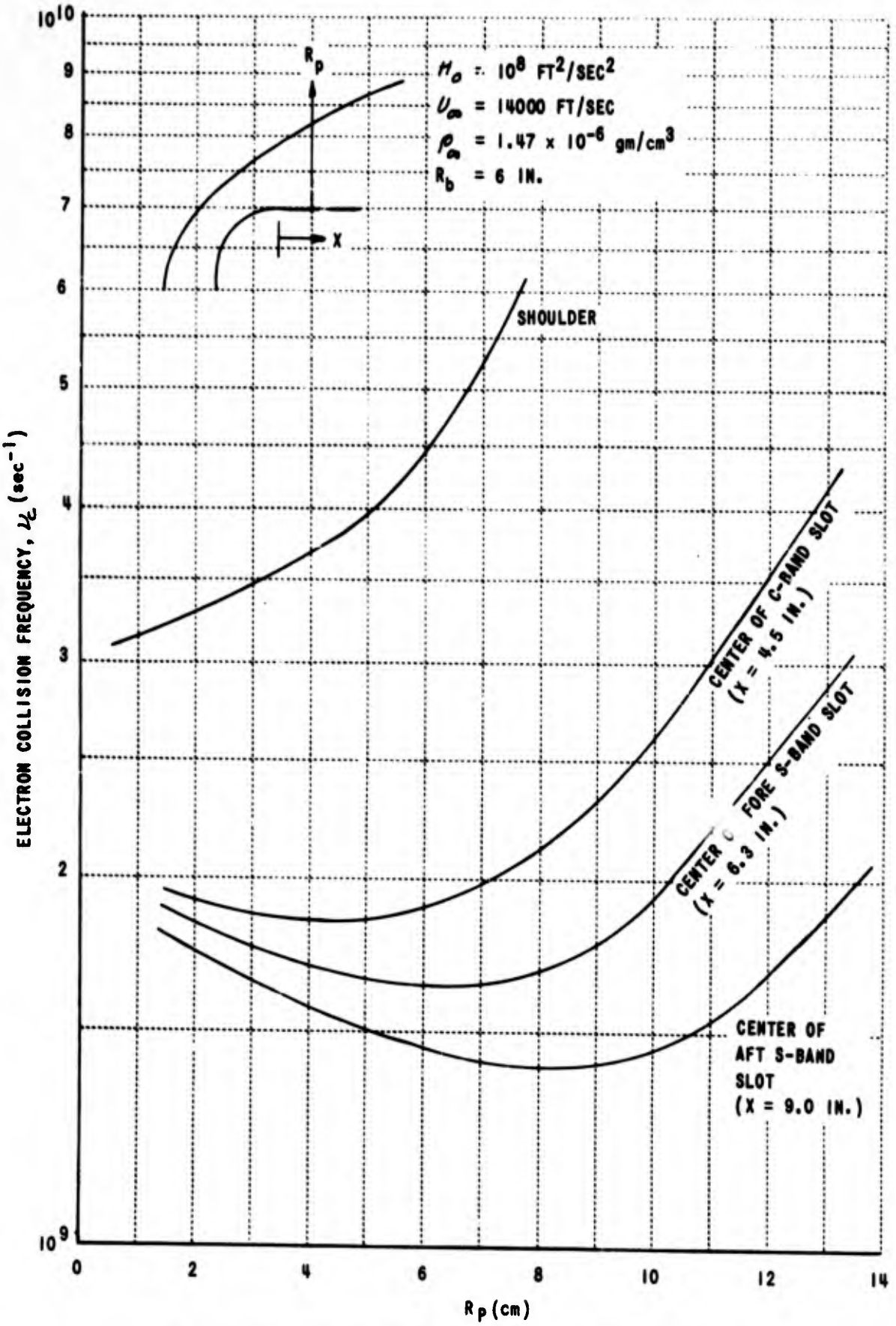


Figure 6 COLLISION FREQUENCY PROFILES CALCULATED ALONG RAYS NORMAL TO MODEL AFTERBODY SURFACE

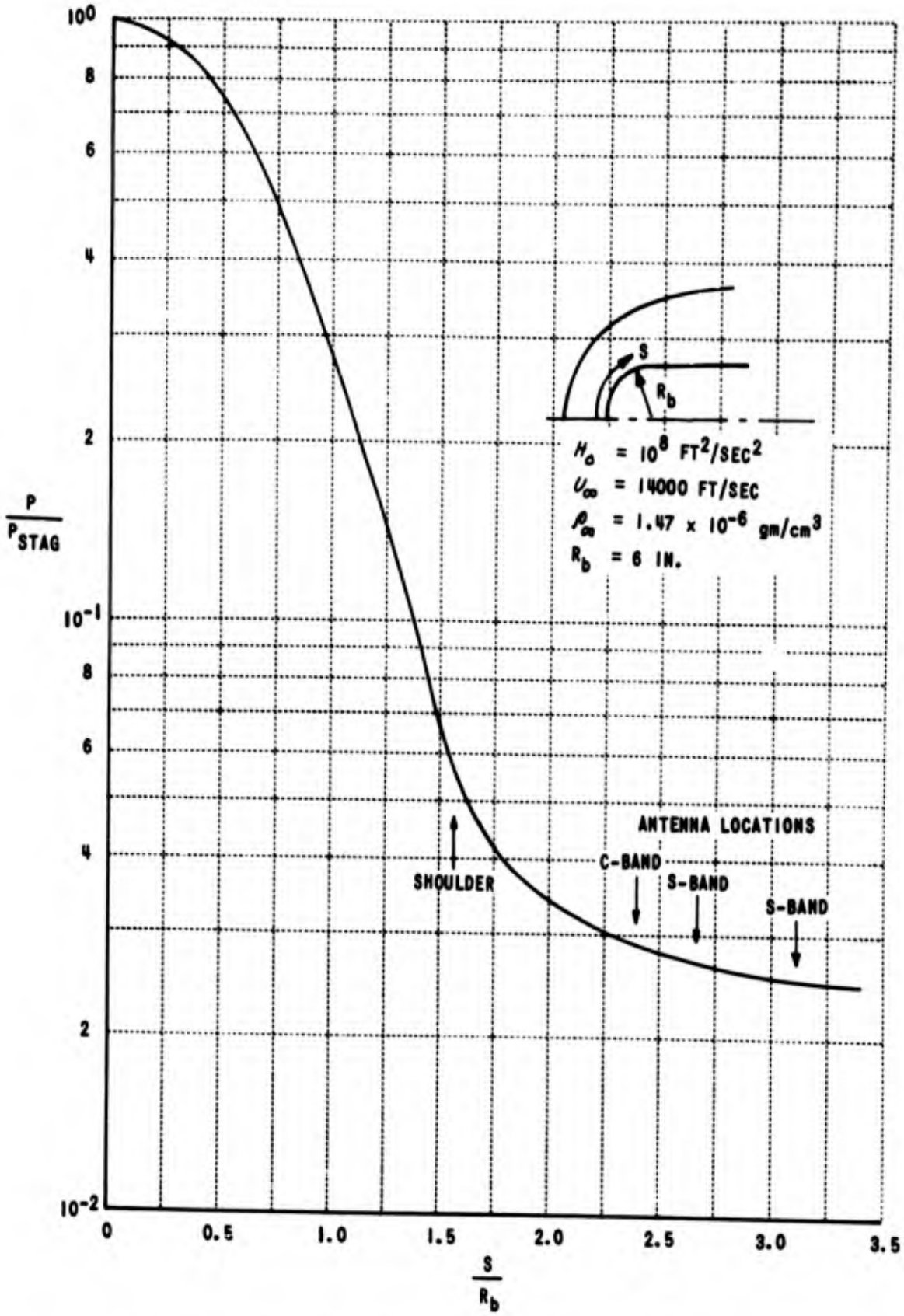


Figure 7 CALCULATED SURFACE PRESSURE DISTRIBUTION OVER THE 12-INCH DIAMETER HEMISPHERE-CYLINDER MODEL

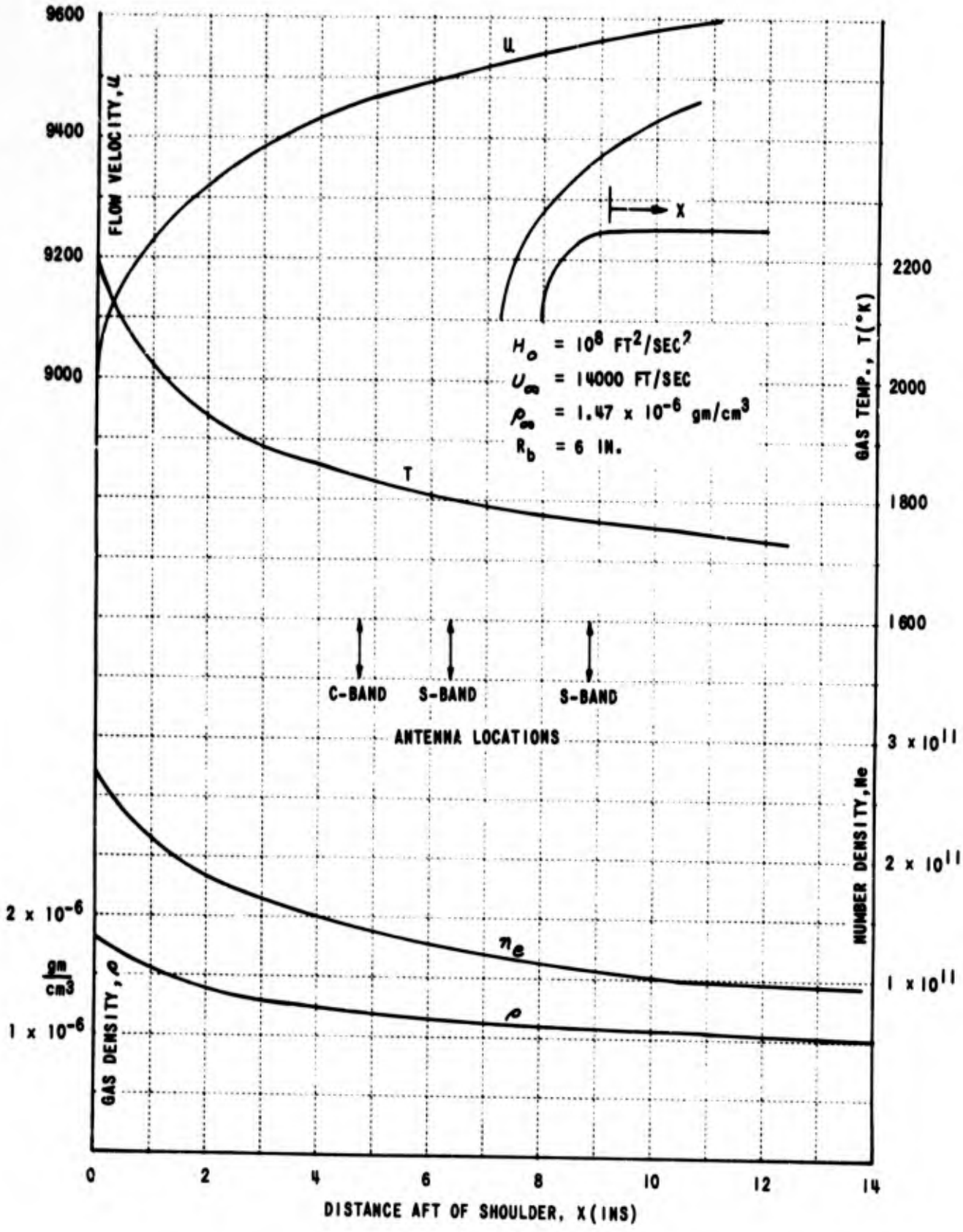


Figure 8 CALCULATED BOUNDARY LAYER EDGE CONDITIONS ON MODEL AFTERBODY

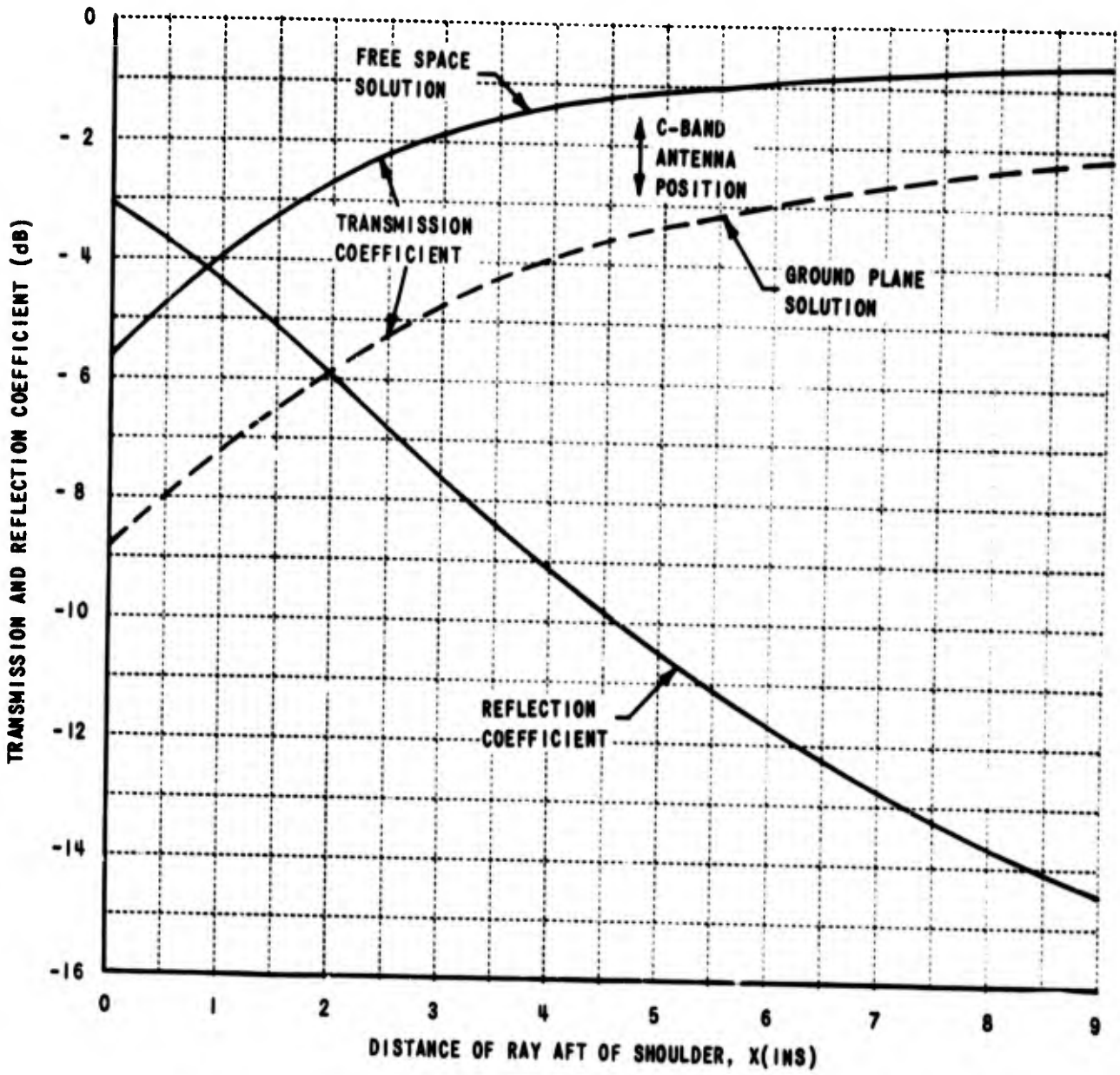


Figure 9 TRANSMISSION AND REFLECTION COEFFICIENTS FOR PROPAGATION AT 4.25 GHz ALONG RAYS NORMAL TO BODY SURFACE

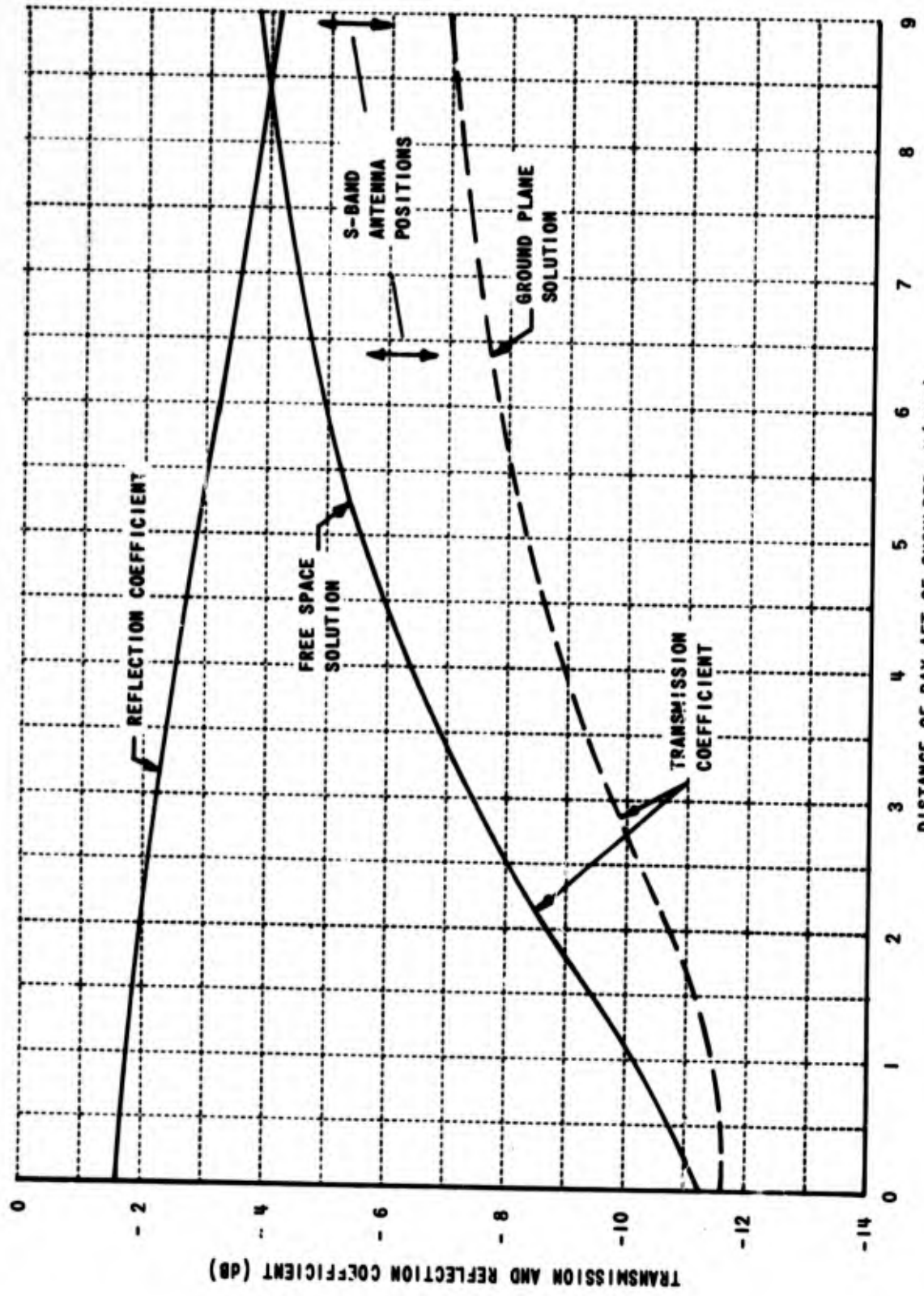


Figure 10 TRANSMISSION AND REFLECTION COEFFICIENTS FOR PROPAGATION AT 2.7 GHz ALONG RAYS NORMAL TO BODY SURFACE

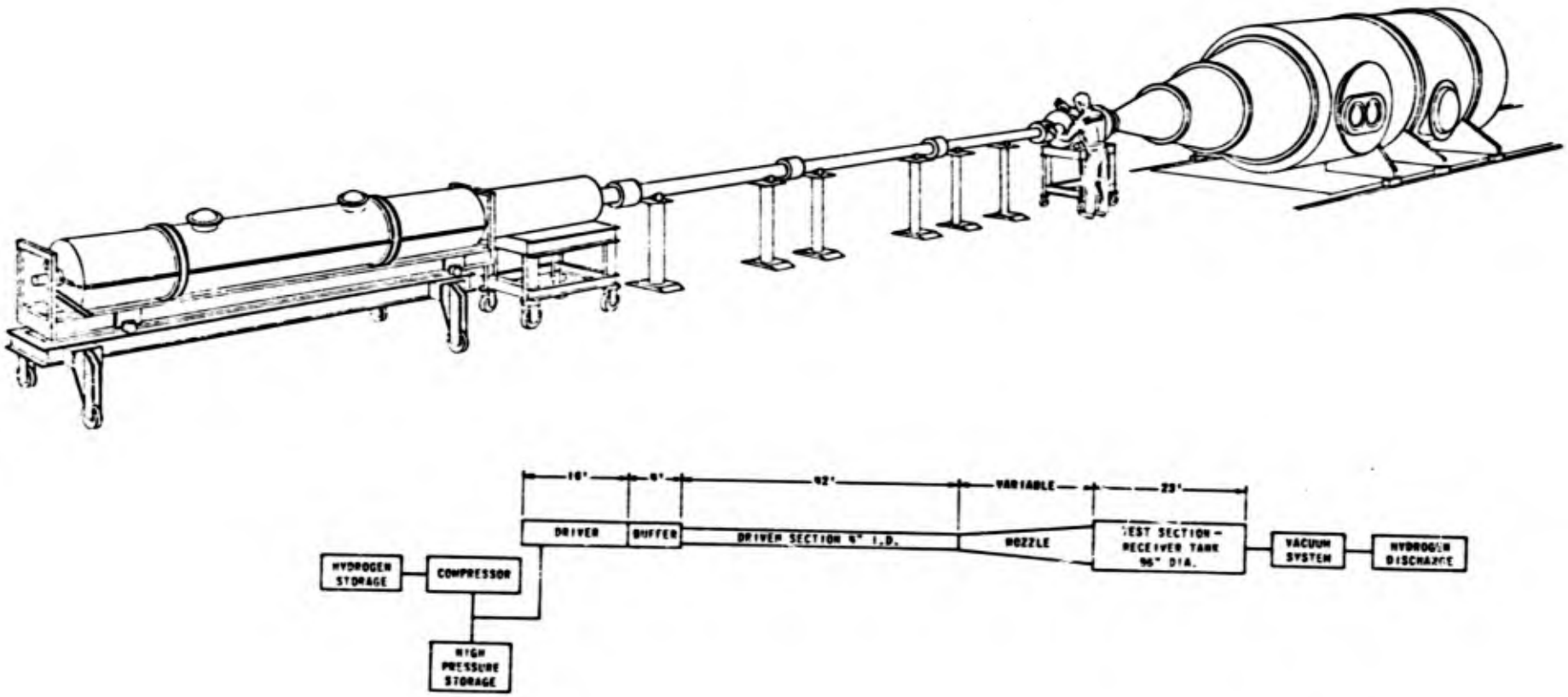


3416

Figure 11 BASIC COMPONENTS OF THE CAL 96-INCH HIGH ENERGY SHOCK TUNNEL

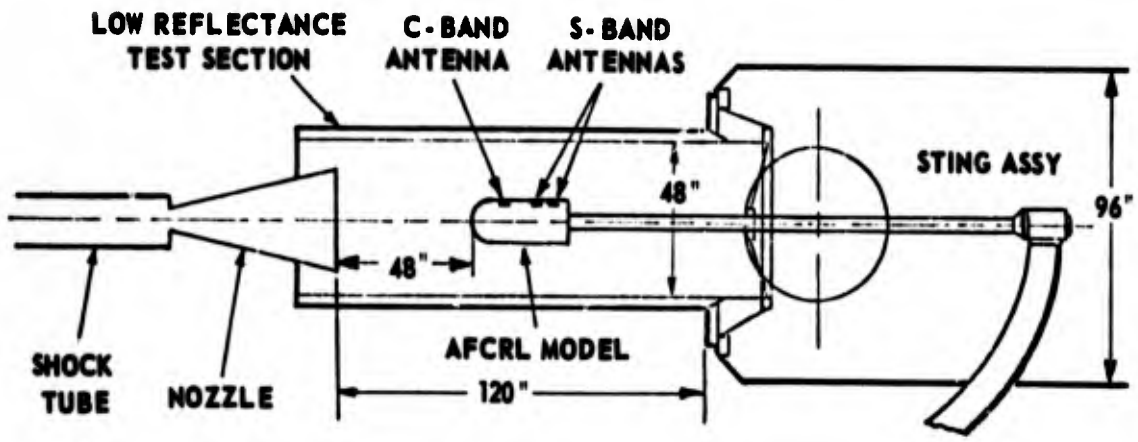


Figure 12 SCHEMATIC DIAGRAM OF TUNNEL LAYOUT

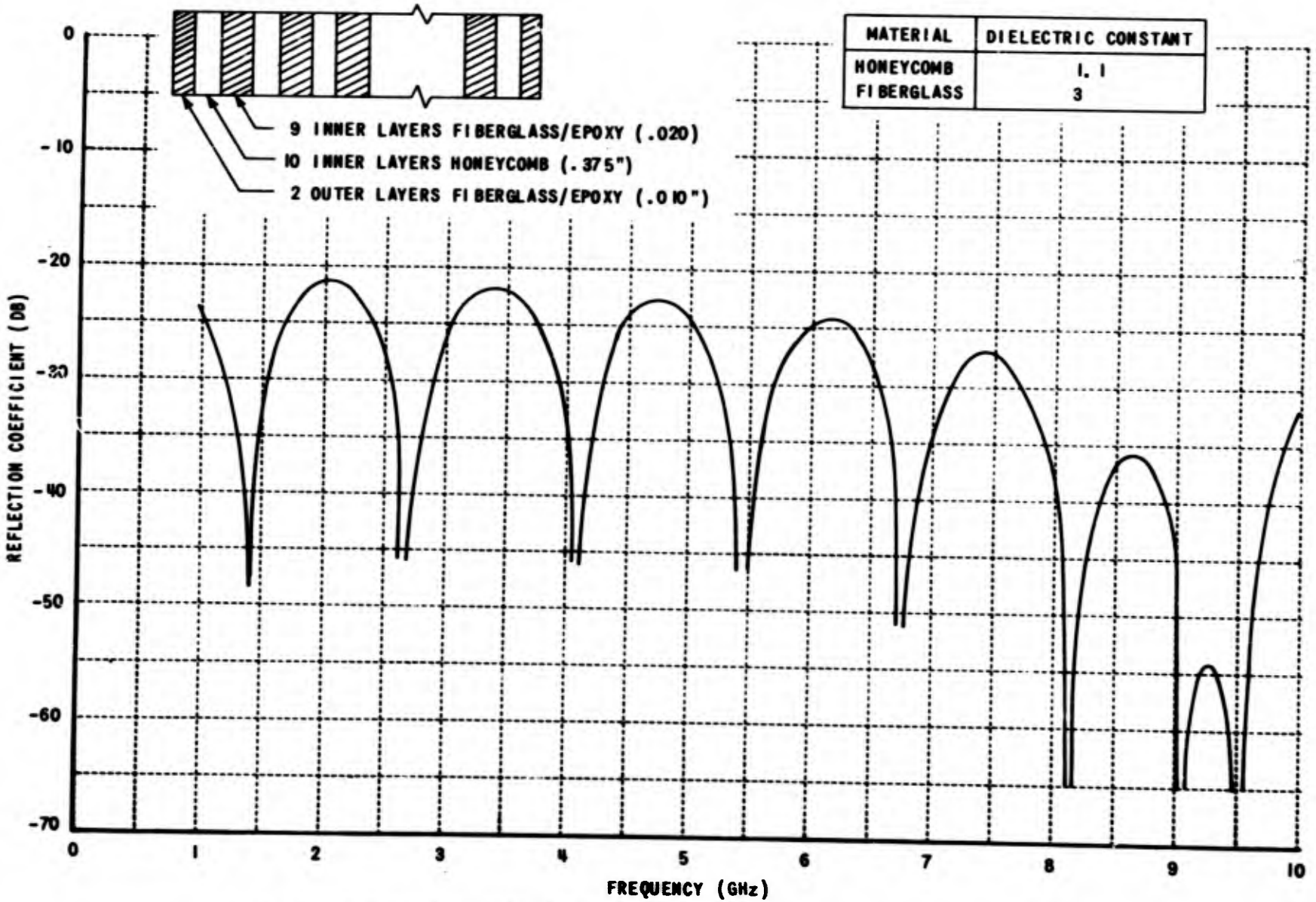


Figure 13 DIELECTRIC TEST SECTION - REFLECTION COEFFICIENT VS FREQUENCY

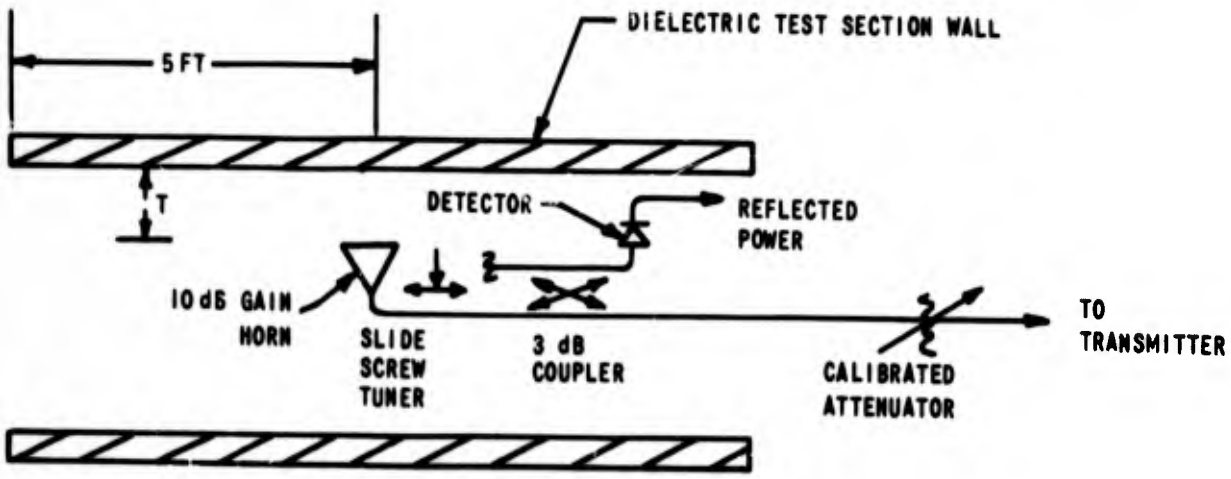


Figure 14 SCHEMATIC OF REFLECTION MEASUREMENT

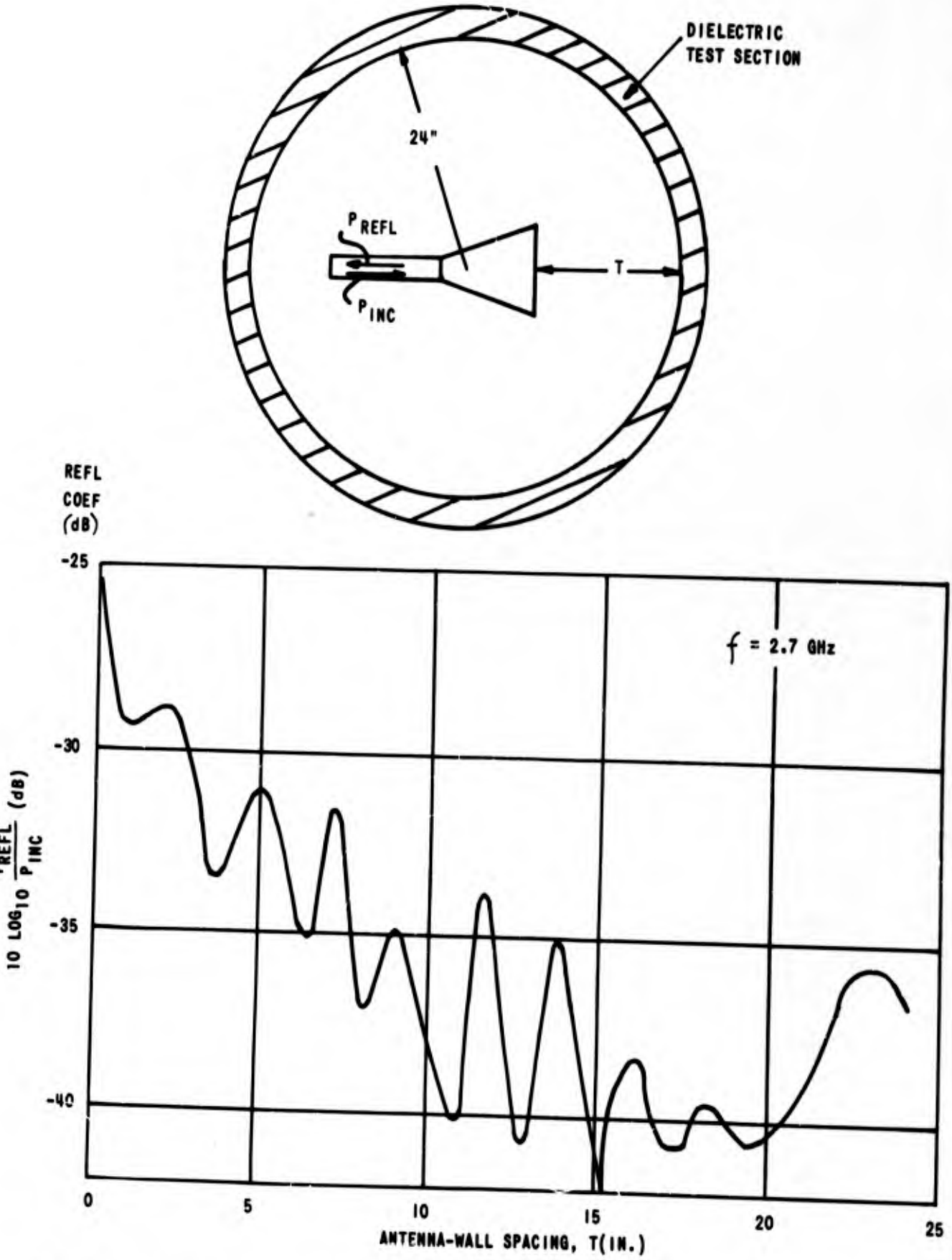


Figure 15 ANTENNA REFLECTION COEFFICIENT vs. ANTENNA-DIELECTRIC WALL SPACING

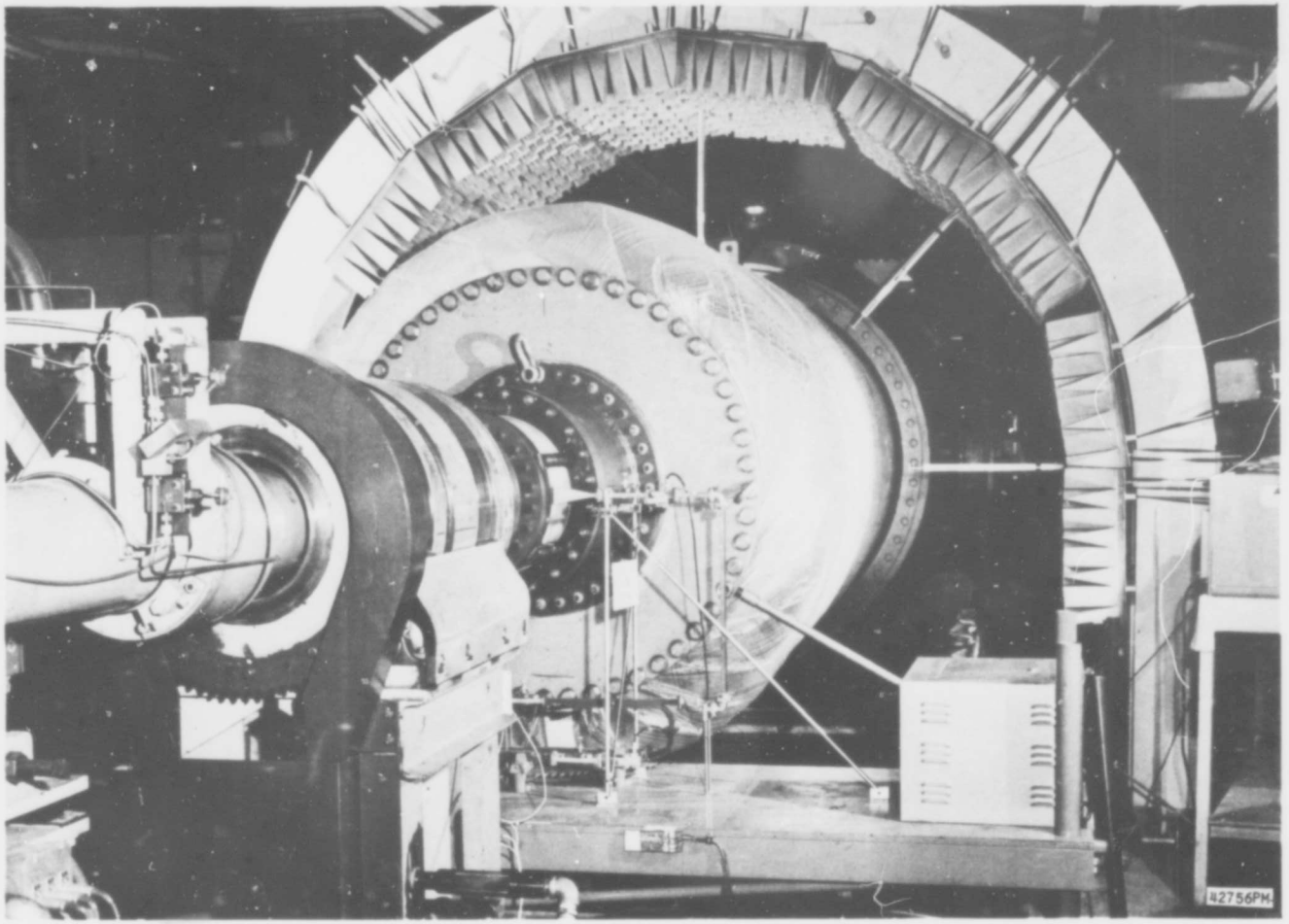


Figure 16 EXPERIMENTAL ARRANGEMENT FOR ANTENNA RADIATION PATTERN MEASUREMENTS

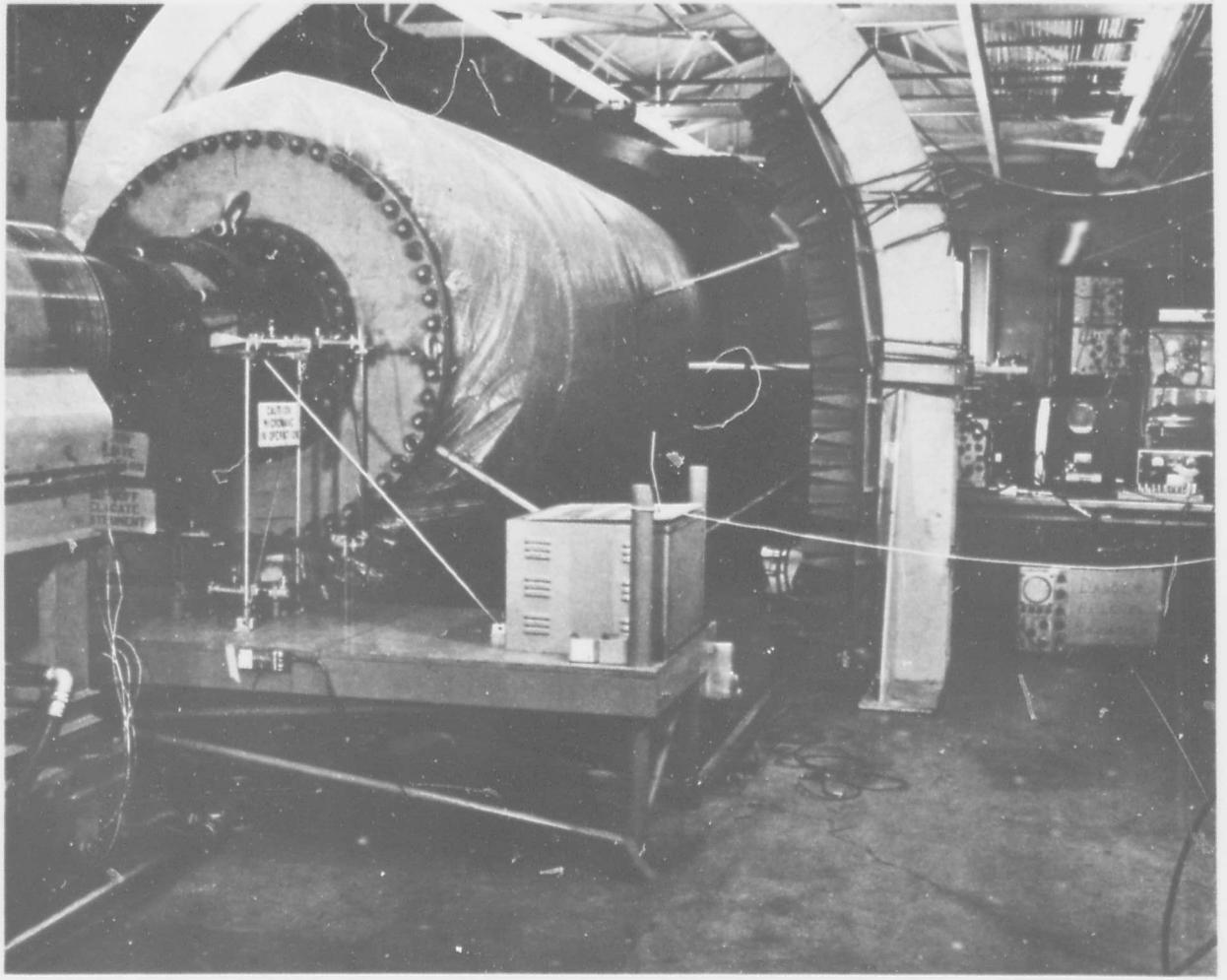

Figure 17 EXPERIMENTAL ARRANGEMENT FOR ANTENNA BREAKDOWN STUDIES

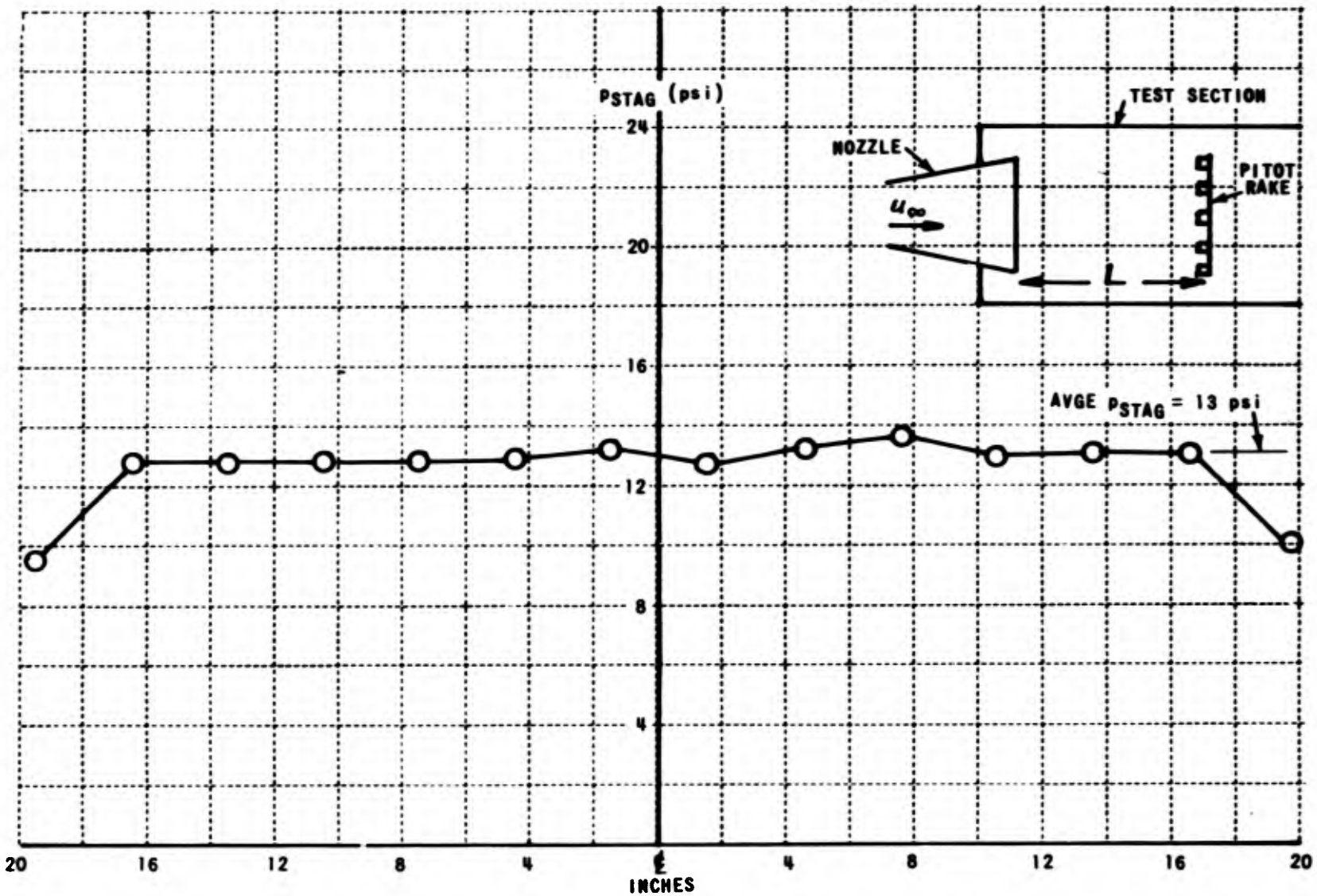


Figure 18 TEST SECTION PITOT PRESSURE DISTRIBUTION

$M_i$ = 9.30, $P_o$ = 8600 psi, THROAT DIA = 1.363 IN., L = 4 FT

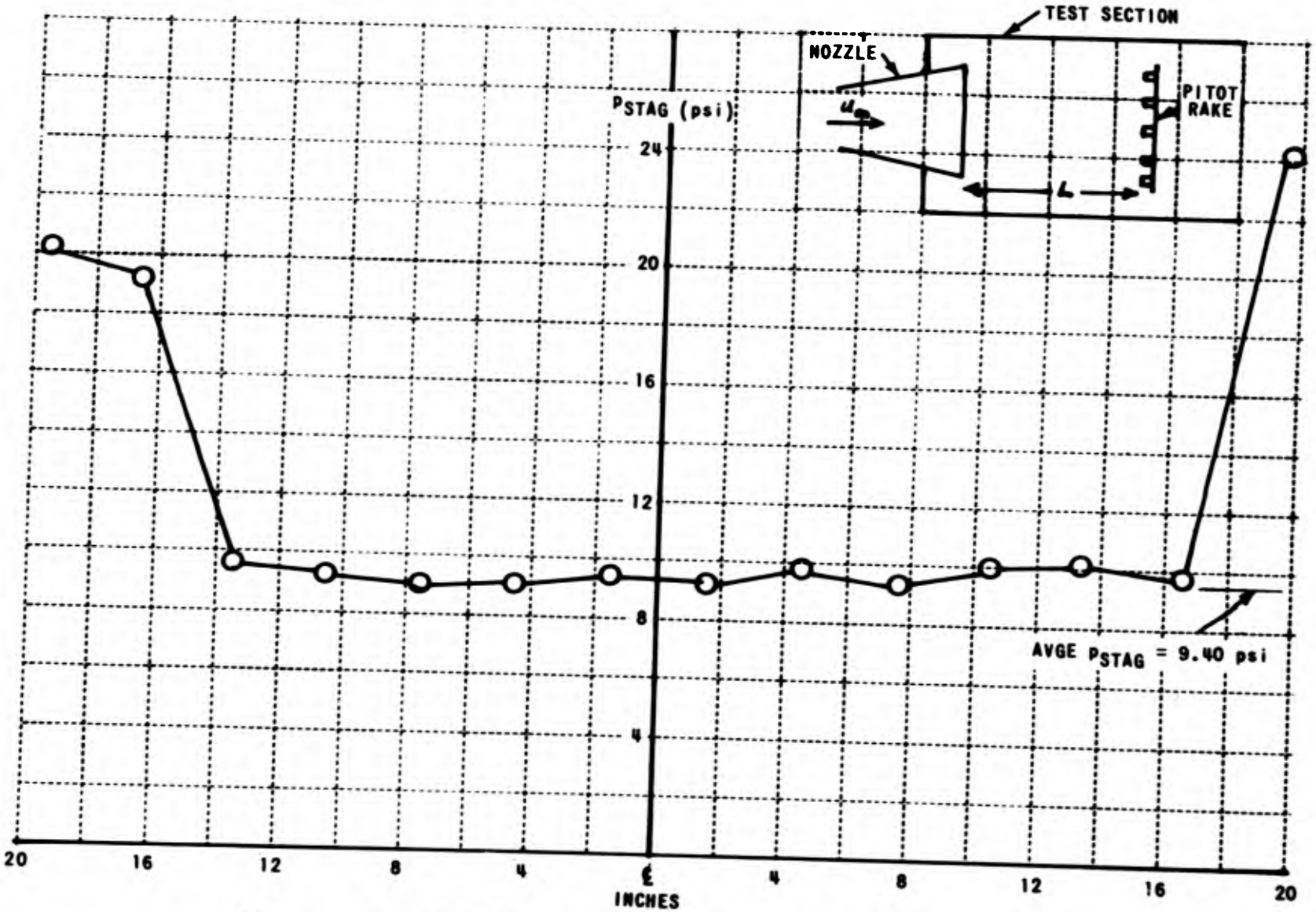


Figure 19 TEST SECTION PITOT PRESSURE DISTRIBUTION

$M_i$ = 9.22, $P_o$ = 8400 psi, THROAT DIA = 1.363 IN., L = 6 FT

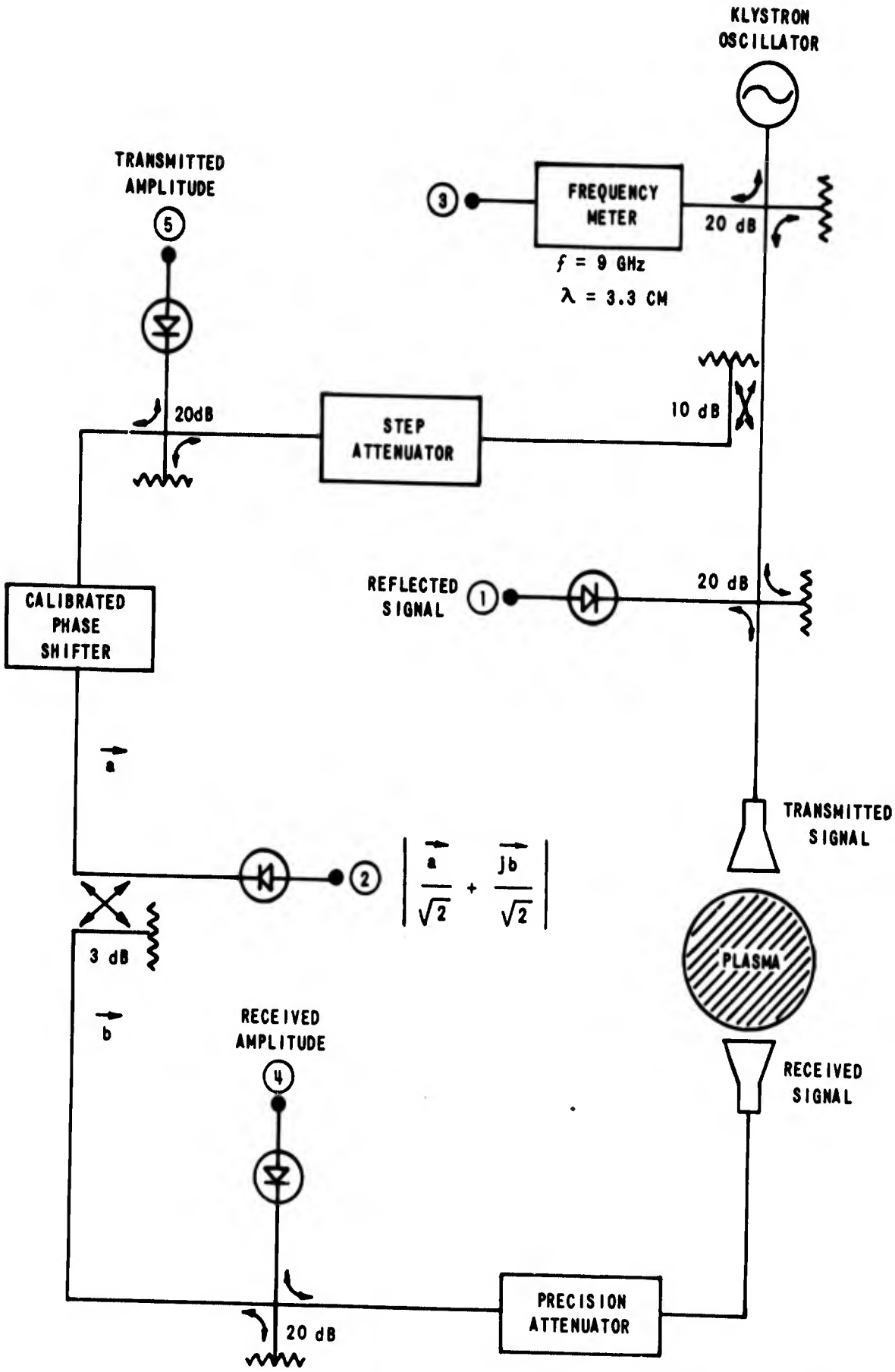


Figure 20 SIMPLIFIED BLOCK DIAGRAM OF SINGLE FREQUENCY MICROWAVE INTERFEROMETER

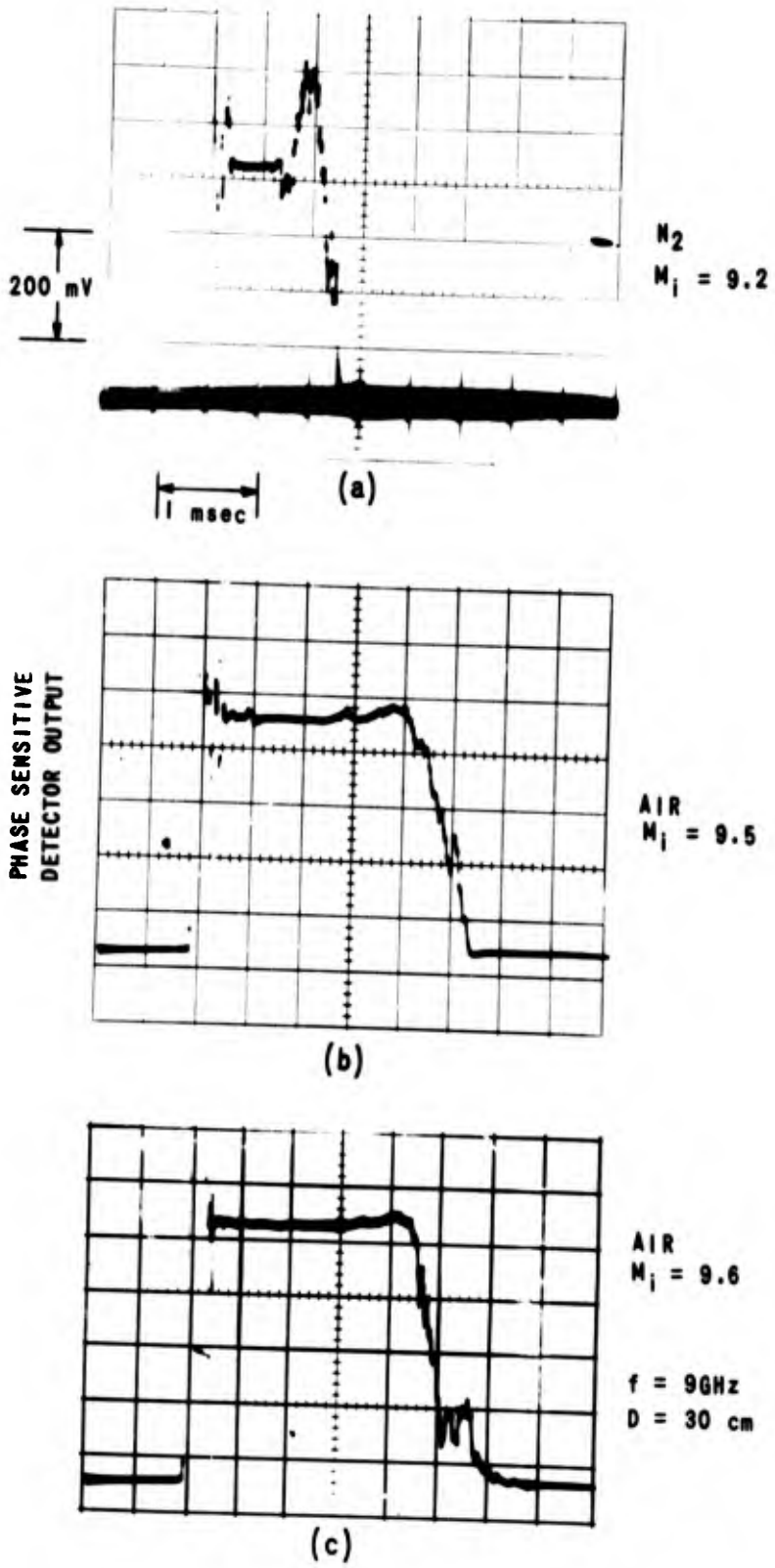


Figure 21 X-BAND INTERFEROMETER RESPONSE IN A HYPERSONIC AIRSTREAM WITH SLIGHT CONTAMINATION

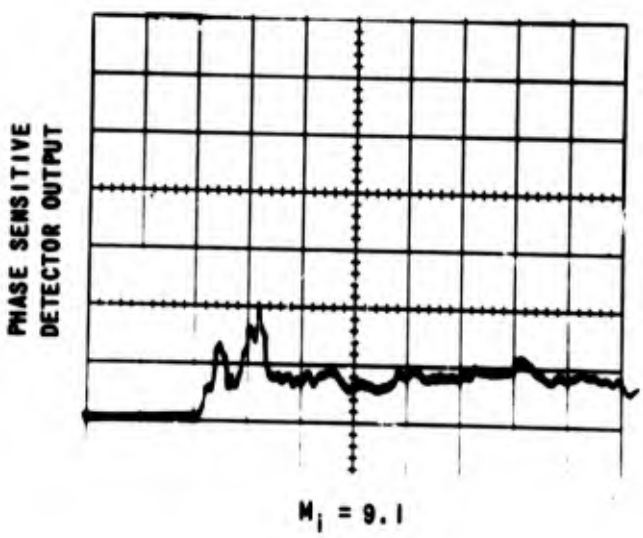


Figure 22 X-BAND INTERFEROMETER RESPONSE IN A PURE HYPERSONIC AIRSTREAM
$f$ = 9 GHz, $D$ = 30 cm

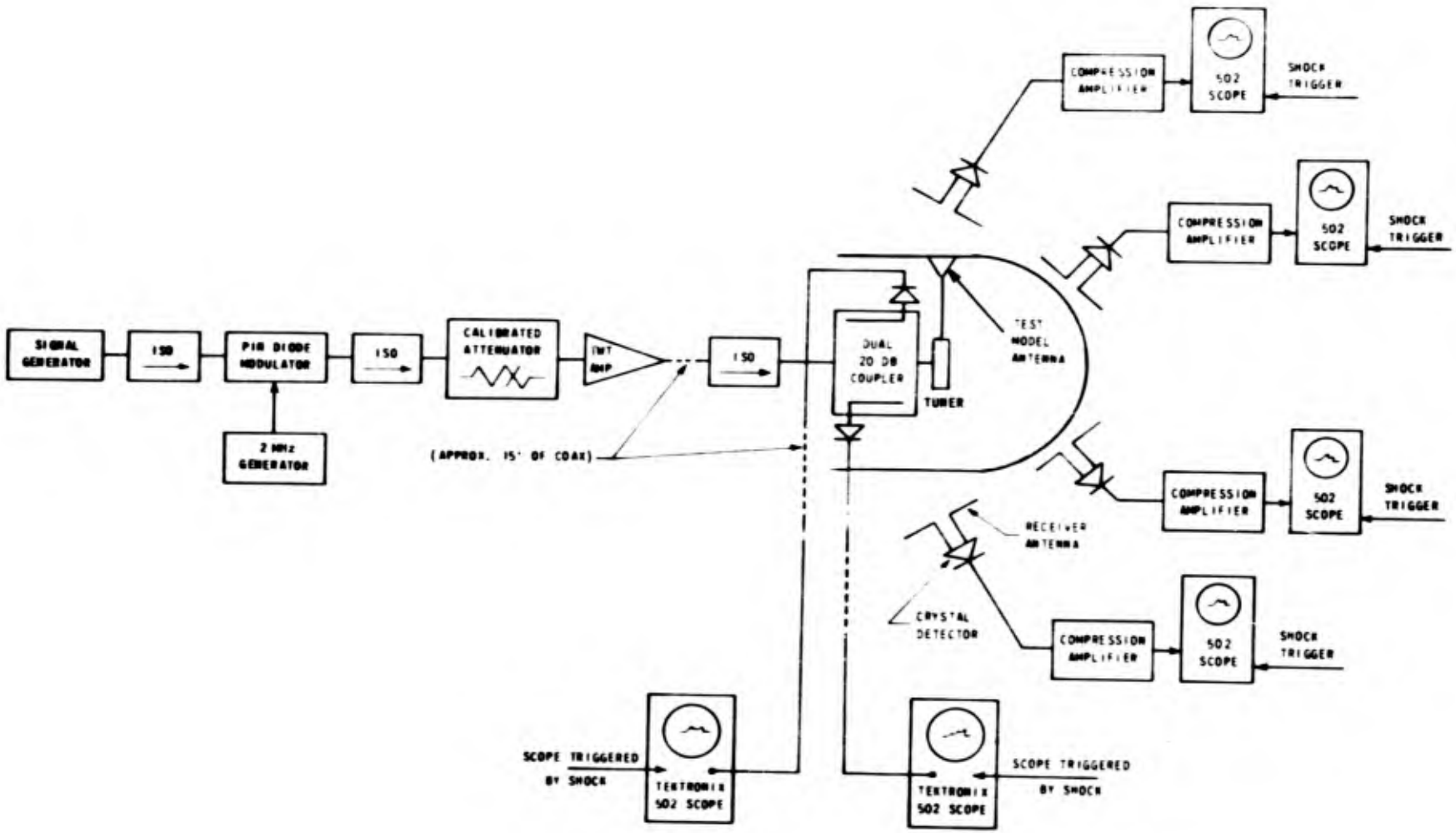


Figure 23 FUNCTIONAL BLOCK DIAGRAM OF MICROWAVE INSTRUMENTATION FOR THE RADIATION PATTERN MEASUREMENTS

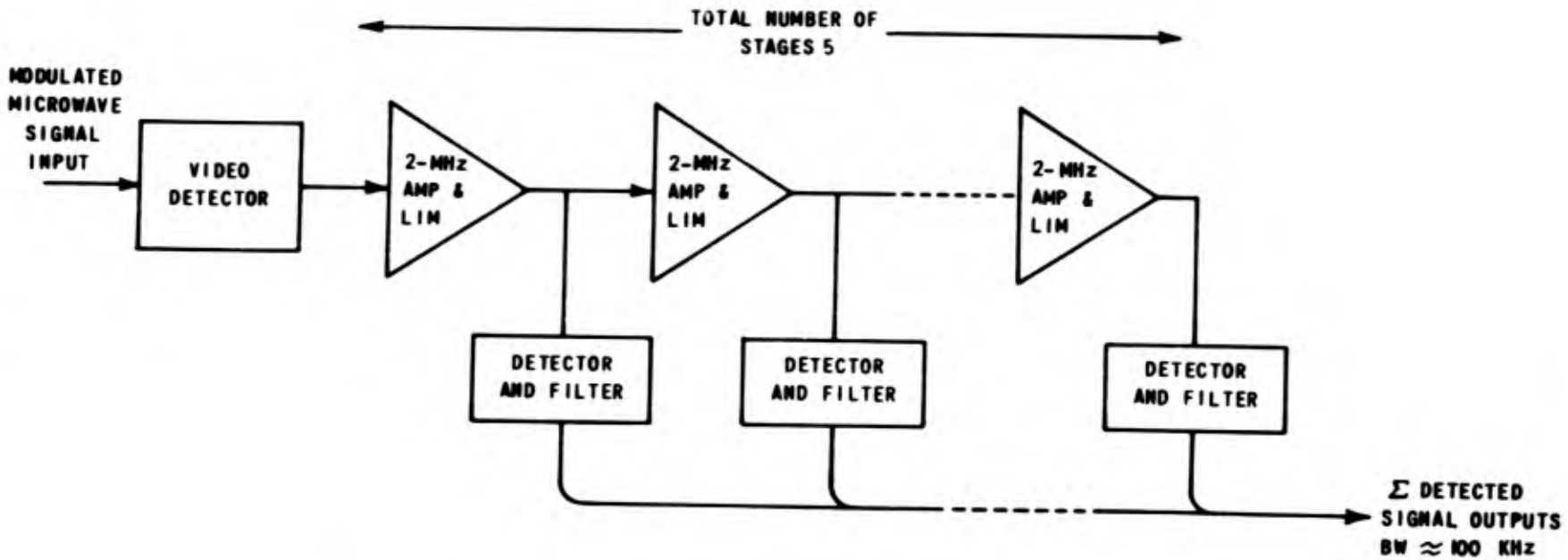


Figure 24 FUNCTIONAL BLOCK DIAGRAM OF THE MICROWAVE COMPRESSION RECEIVER

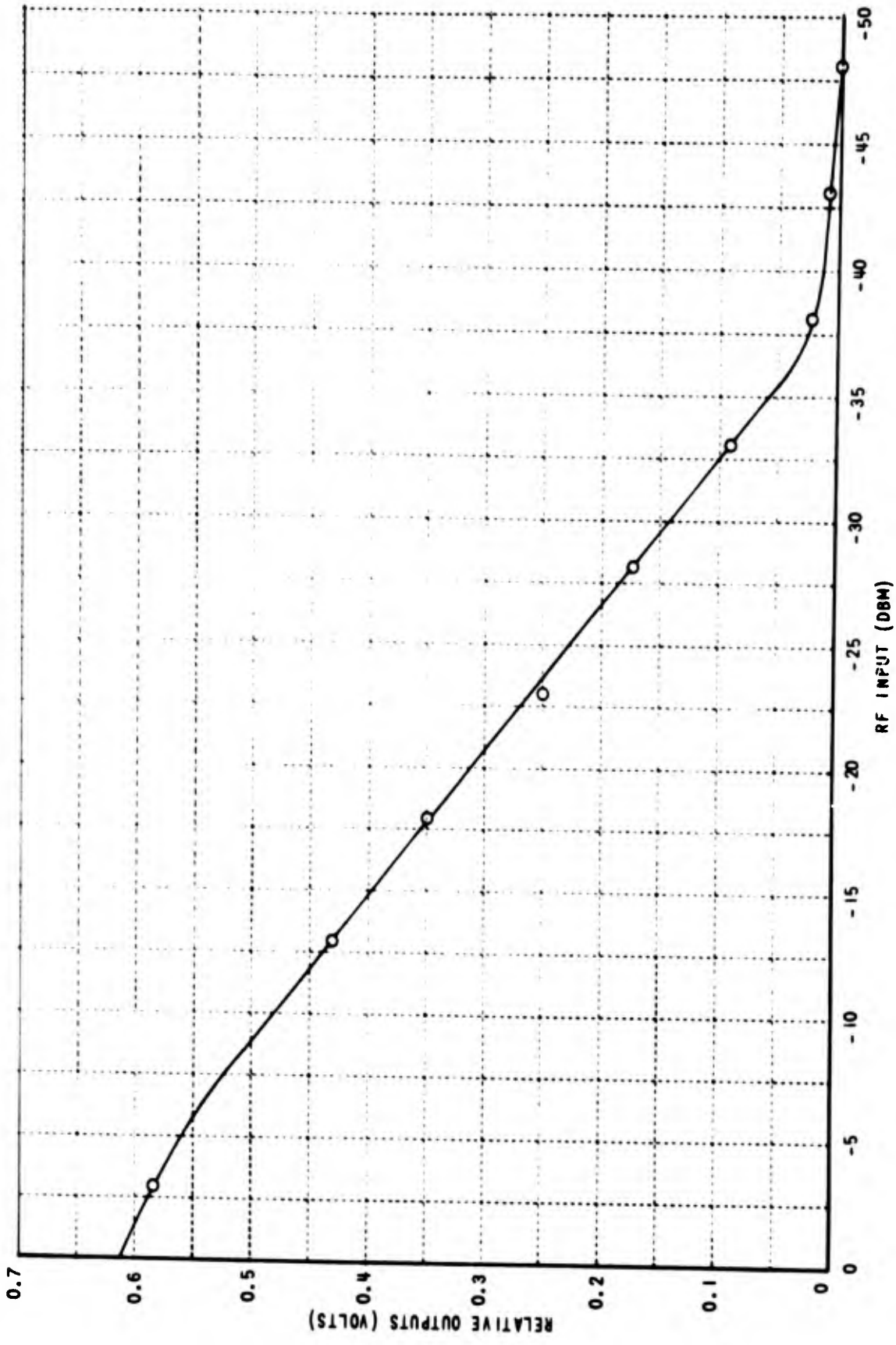


Figure 25 DYNAMIC RANGE OF MICROWAVE COMPRESSION RECEIVER

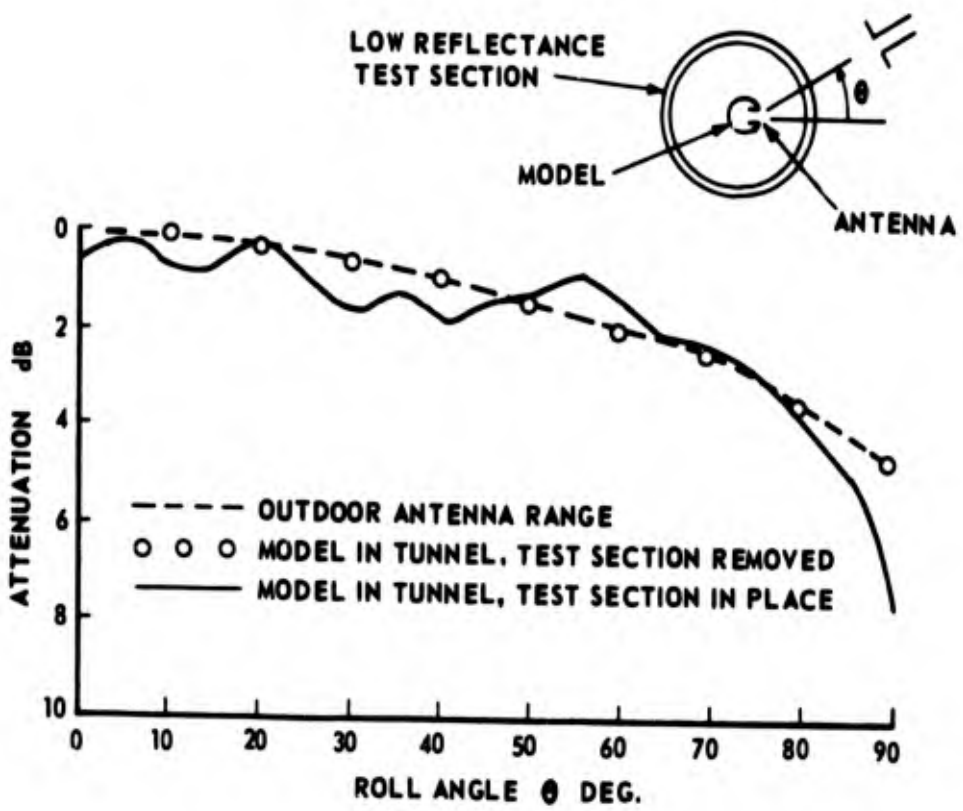


Figure 26 LOW-REFLECTANCE TEST SECTION PERFORMANCE

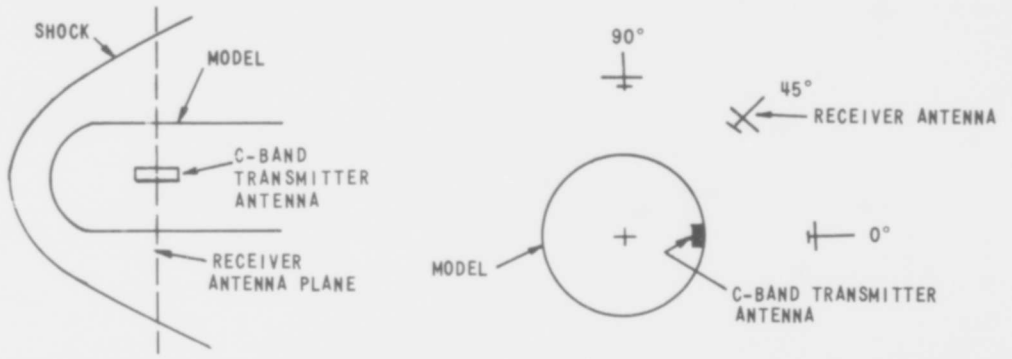


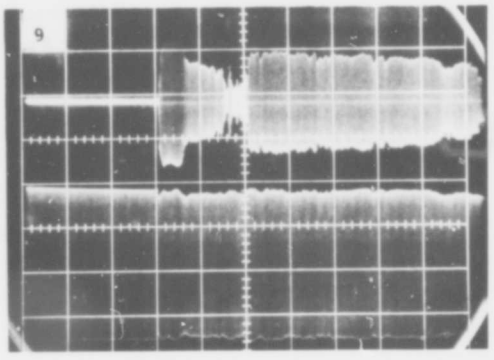


(a) REFLECTED POWER
(B) INCIDENT POWER

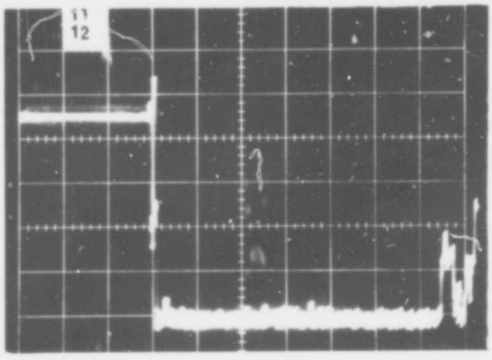


θ = 0°

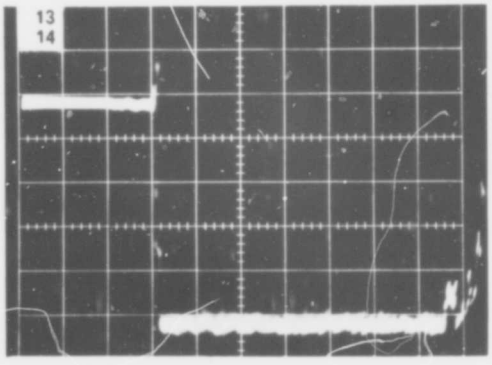


θ = 45°

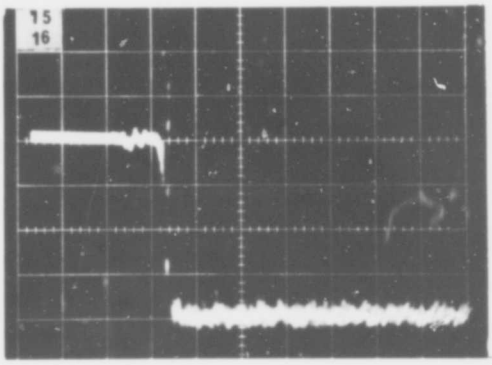


θ = 90°

Figure 27 INCIDENT AND REFLECTED POWER AT TRANSMITTER ANTENNA, AND RECEIVED SIGNALS $M_i$ = 8.62, THROAT DIAMETER = 1.36 IN., f = 4.25 GHz, SWEEP = 0.5 msec/cm

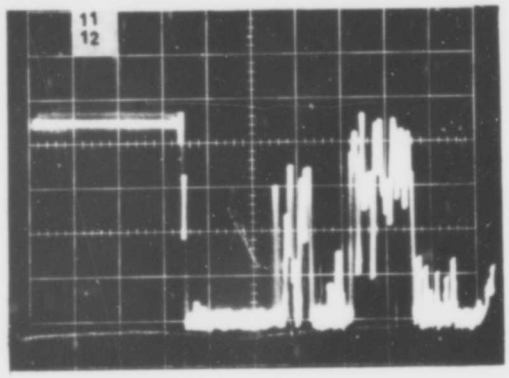


θ = 0°

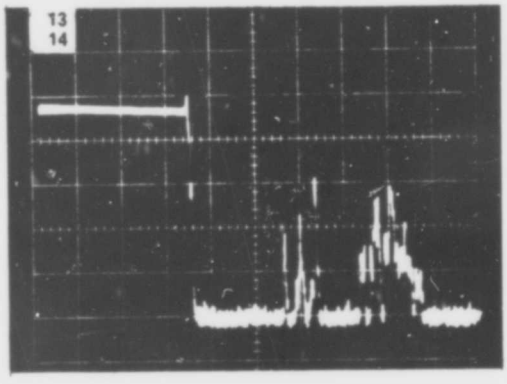


θ = 45°

Figure 28 RECEIVED SIGNALS AT 0° AND 45° ANTENNA POSITIONS
$M_j$ = 7.7, THROAT DIAMETER = 1.38 IN., f = 4.25 GHz
SWEEP = 0.5 msec/cm

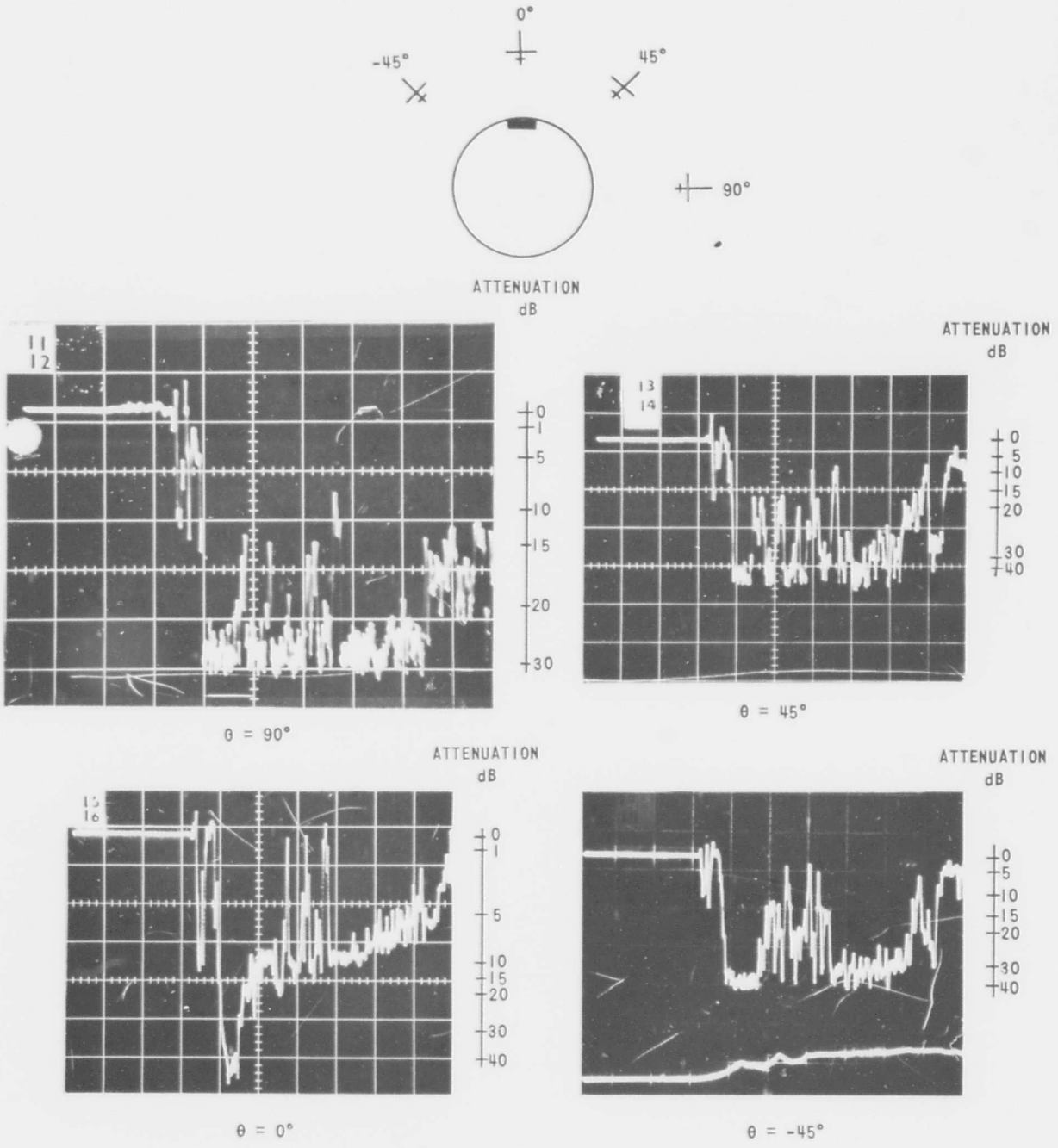


Figure 29 RECEIVED SIGNALS
$M_i$ =8.52, THROAT DIAMETER =0.66 IN.,
f =4.25 GHz, SWEEP =0.5 msec/cm

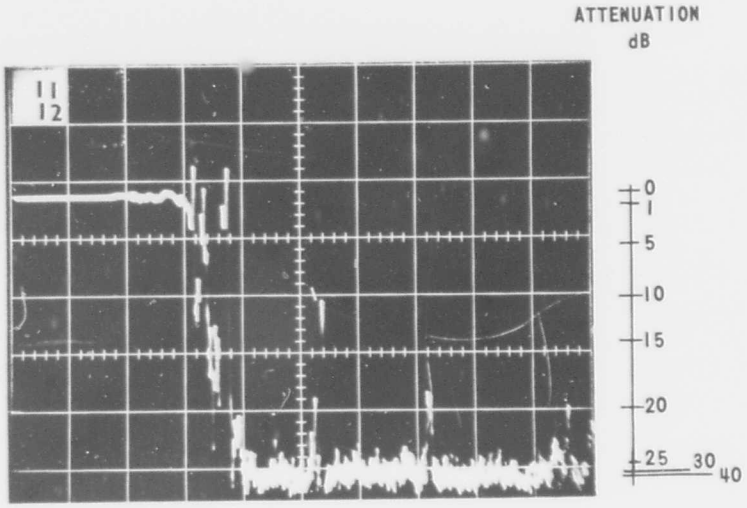


θ = 90°

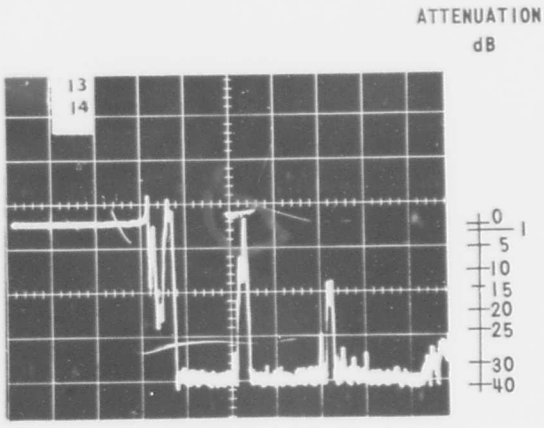


θ = 45°

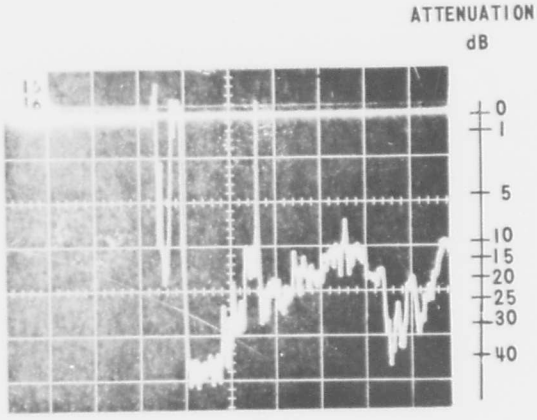


θ = 0°

Figure 30 RECEIVED SIGNALS
$M_i$ = 8.55, THROAT DIAMETER = 0.66 IN.,
f = 4.25 GHz, SWEEP = 0.5 msec/cm

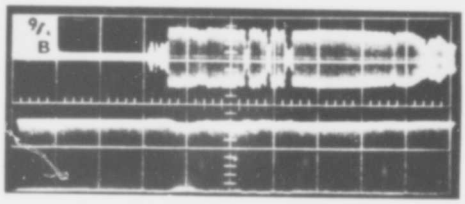

(a) REFLECTED POWER

(b) INCIDENT POWER
$M_i$ = 8.52

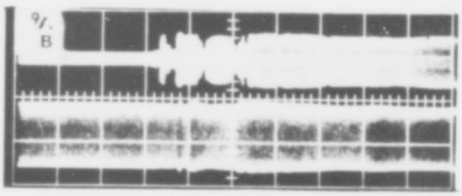

$M_i$ = 8.55

Figure 31 INCIDENT AND REFLECTED POWER AT C-BAND TRANSMITTER ANTENNA THROAT DIAMETER = 0.66 IN. f = 4.25 GHz, SWEEP = 0.5 msec/cm

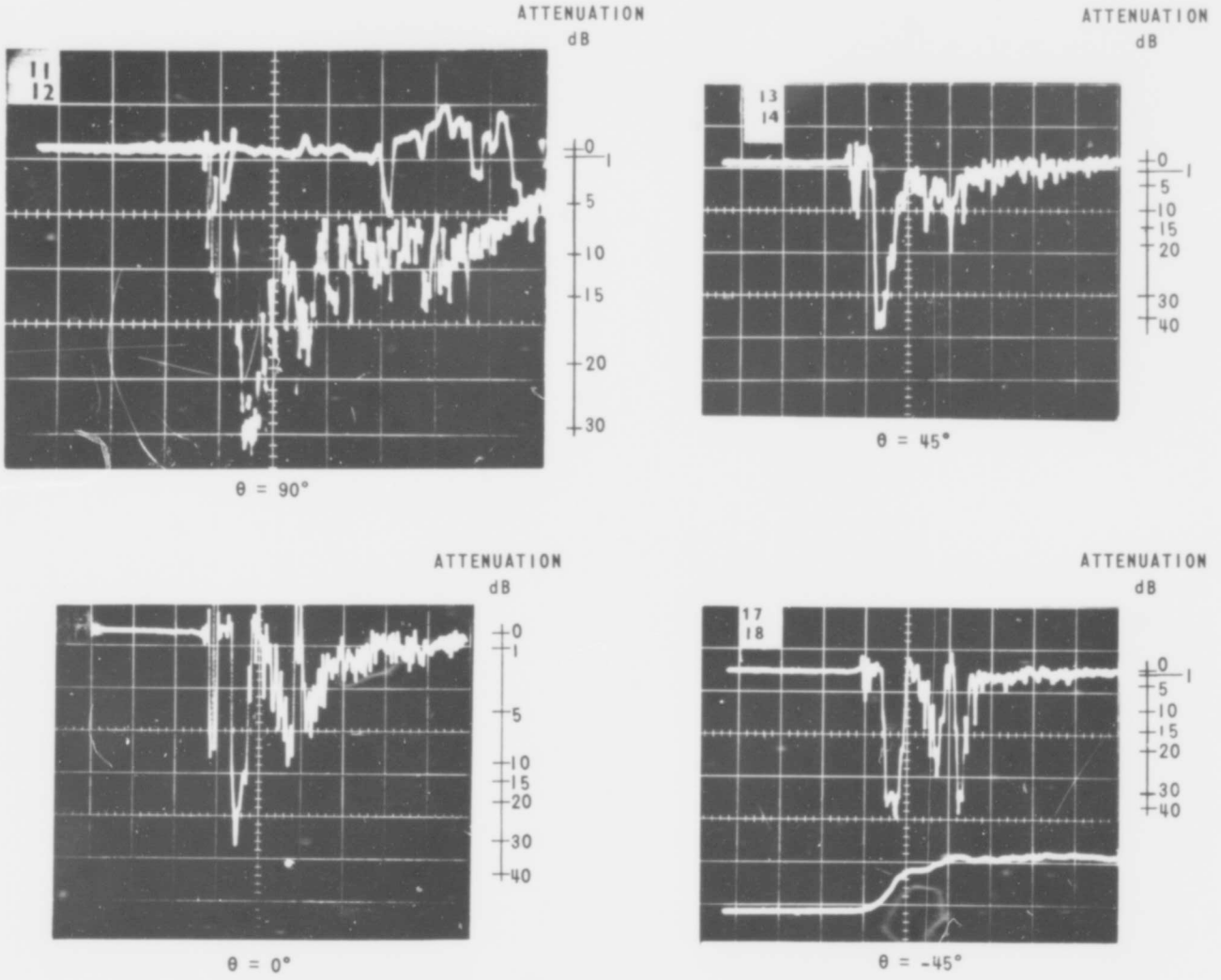


Figure 32 RECEIVED SIGNALS
$M_i$ = 8.57, THROAT DIAMETER = 0.5 IN.,
f = 4.25 GHz, SWEEP = 0.5 msec/cm

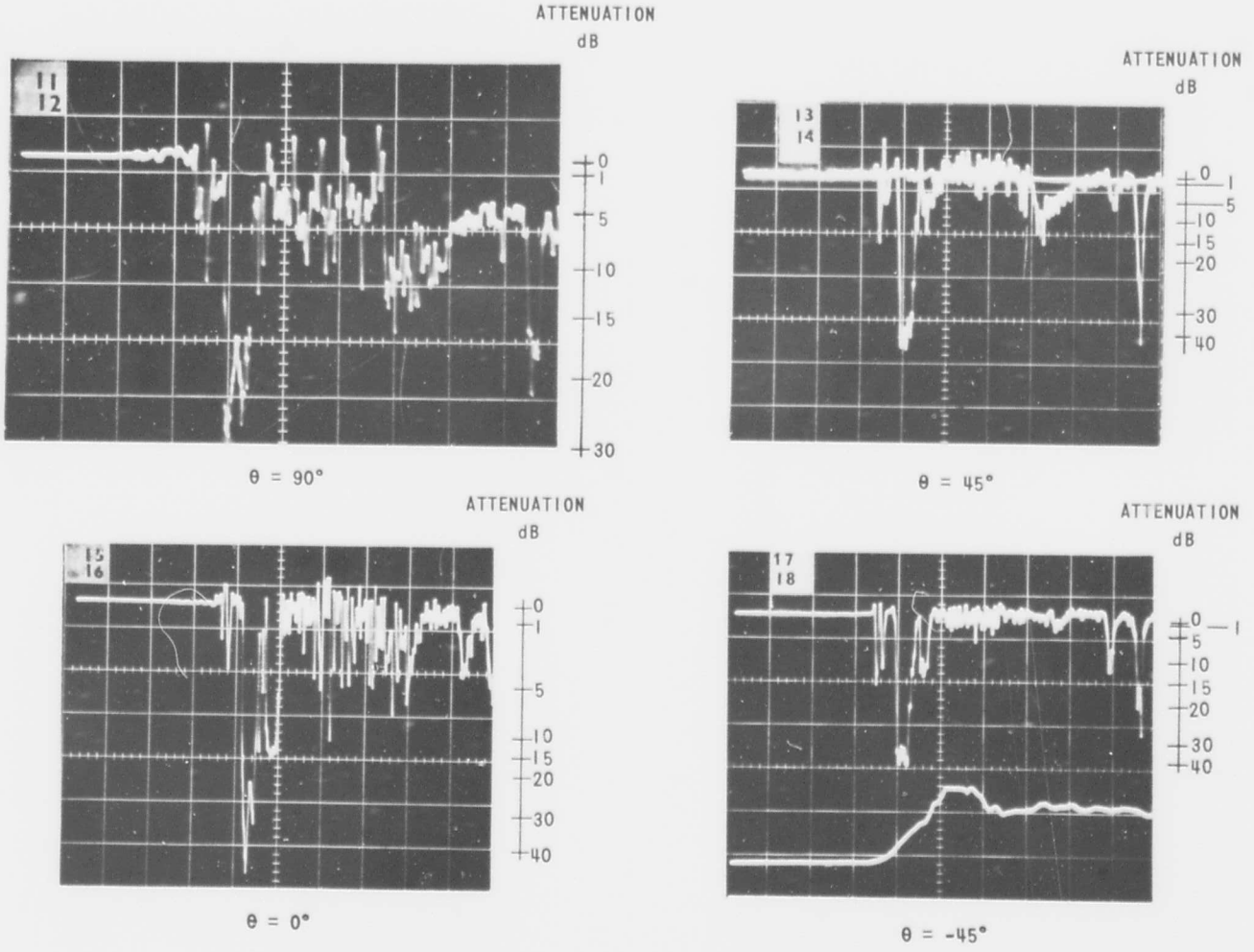


Figure 33 RECEIVED SIGNALS
$M_j$ = 8.53, THROAT DIAMETER = 0.5 IN.,
f = 4.25 GHz, SWEEP = 0.5 msec/cm

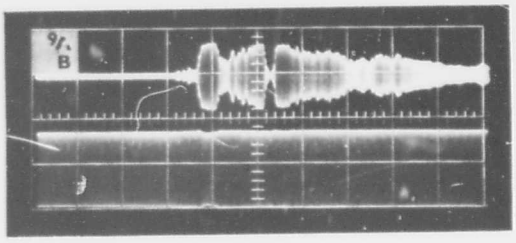


$M_i = 8.57$

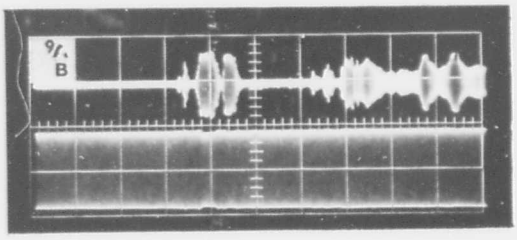


$M_i = 8.53$

Figure 34 INCIDENT AND REFLECTED POWER AT C-BAND TRANSMITTER ANTENNA THROAT DIAMETER = 0.5 IN., f = 4.25 GHz, SWEEP = 0.5 msec/cm

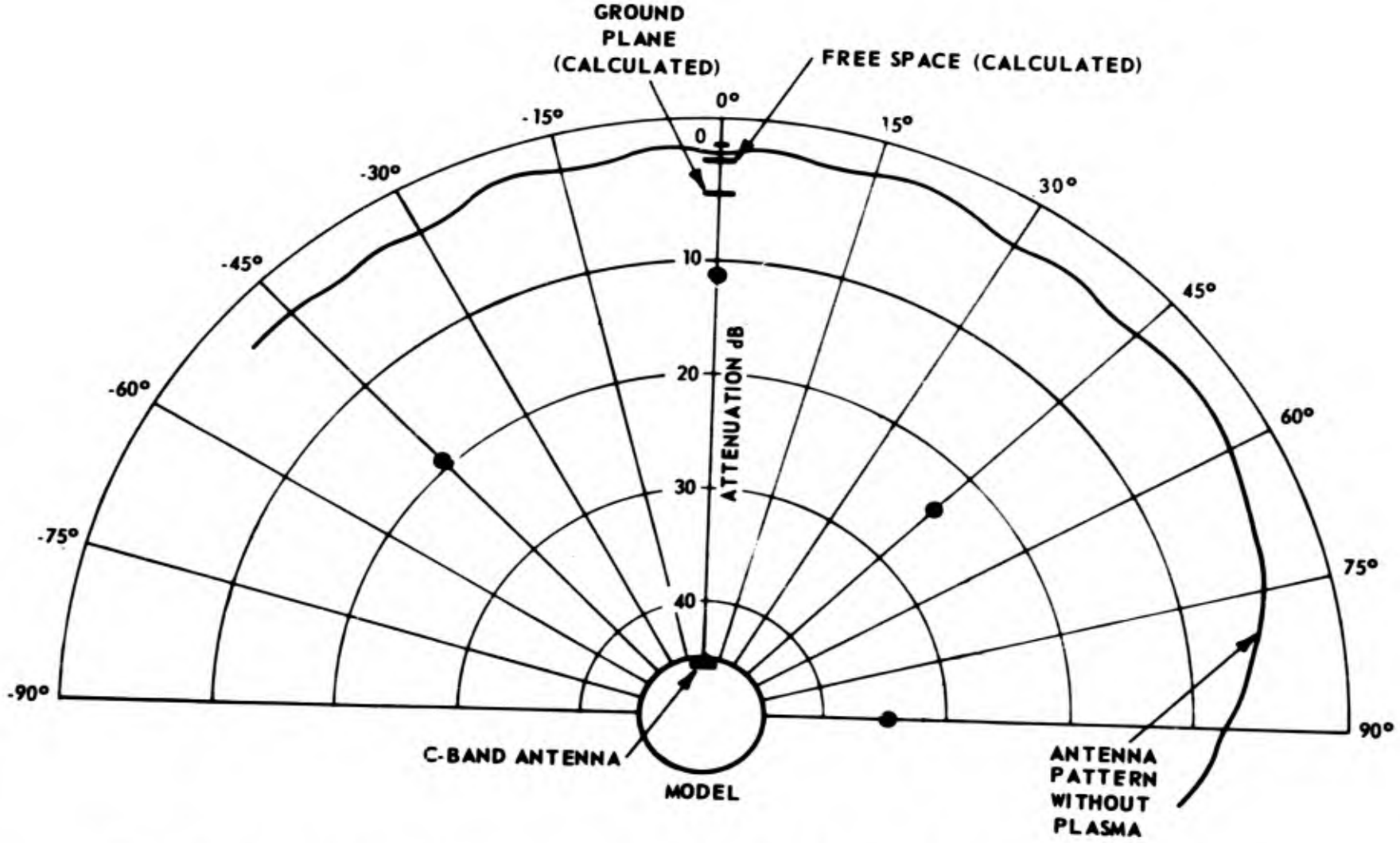


Figure 35 SIGNAL ATTENUATION THROUGH HEMISPHERE-CYLINDER MODEL AFTERBODY PLASMA
$M_i$ = 8.52, THROAT DIAMETER = 0.66 INCH, f = 4.25 GHz

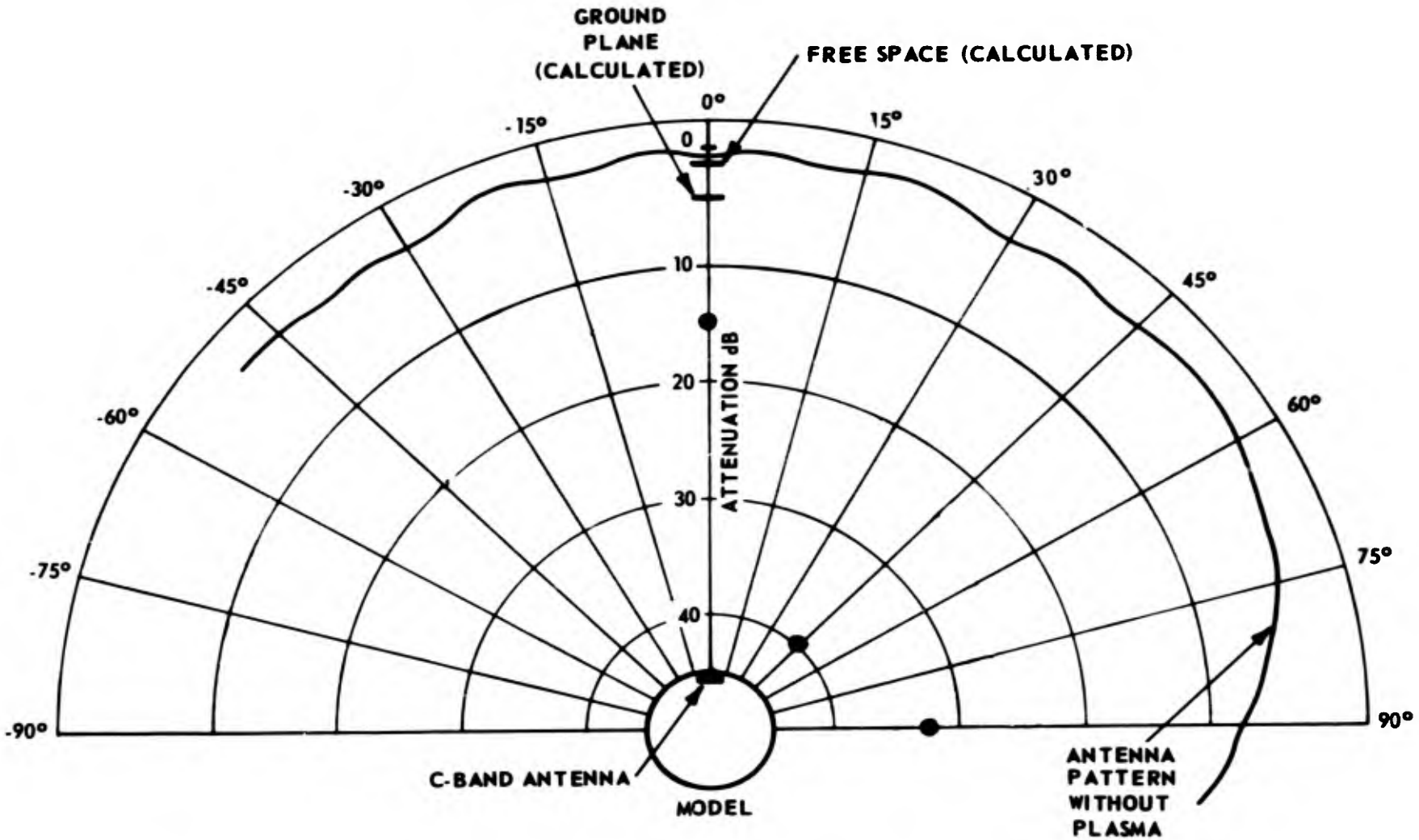


Figure 36 SIGNAL ATTENUATION THROUGH HEMISPHERE-CYLINDER MODEL AFTERBODY PLASMA
$M_i$ = 8.55, THROAT DIAMETER = 0.66 INCH, f = 4.25 GHz

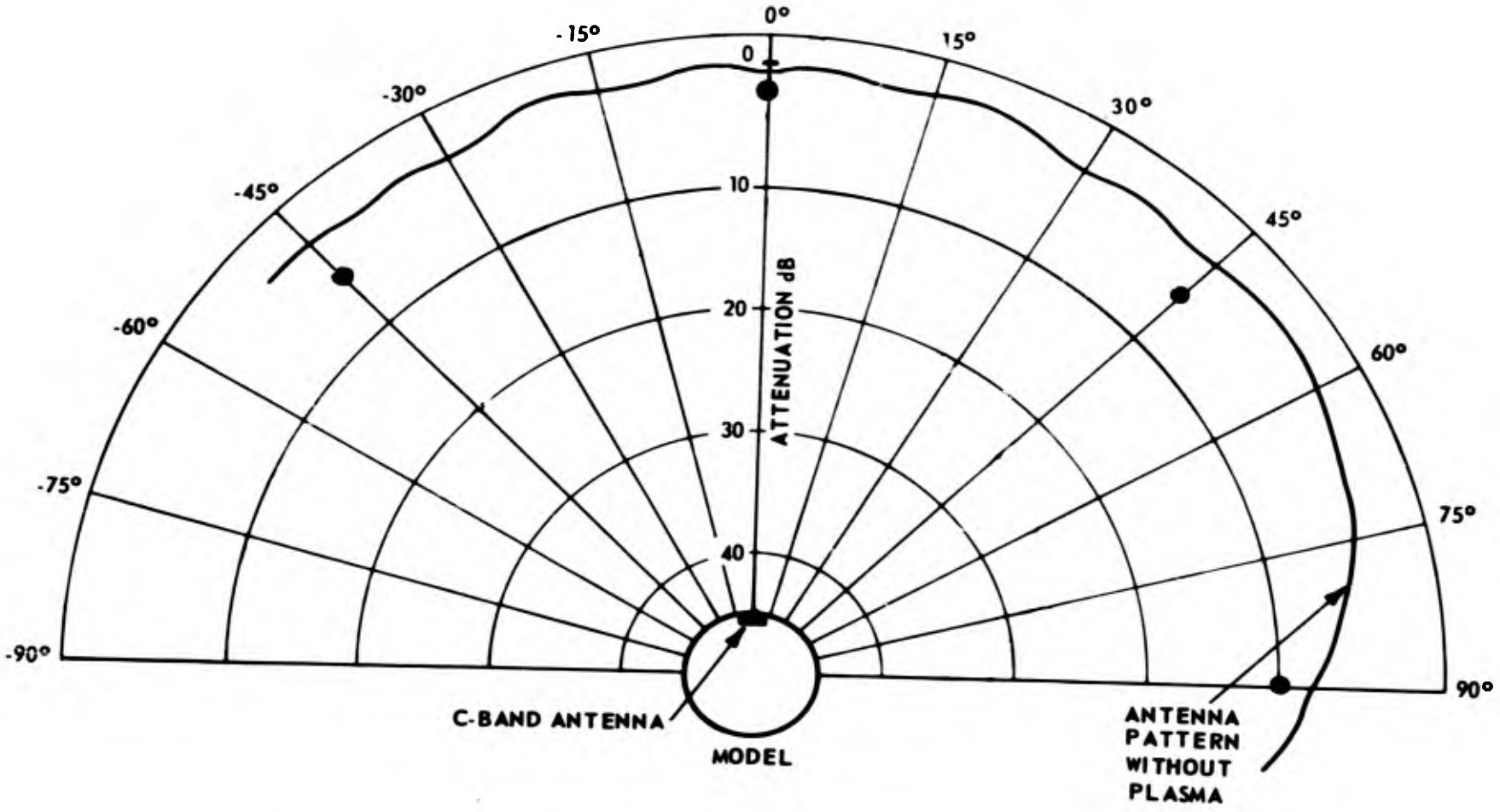


Figure 37 SIGNAL ATTENUATION THROUGH HEMISPHERE-CYLINDER MODEL AFTERBODY PLASMA
$M_i$ = 8.57, THROAT DIAMETER = 0.50 INCH, $f$ = 4.25 GHz

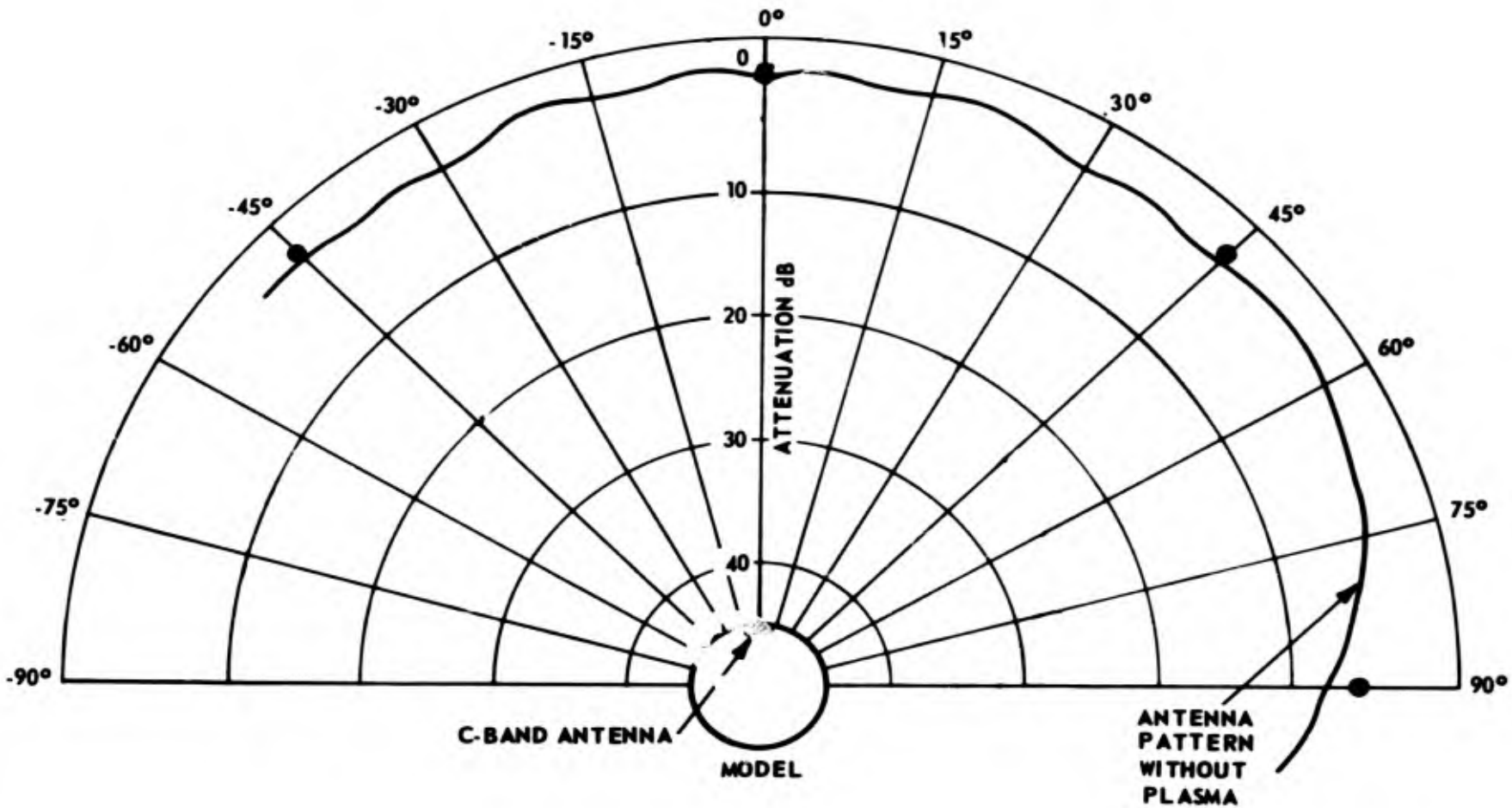


Figure 38 SIGNAL ATTENUATION THROUGH HEMISPHERE-CYLINDER MODEL AFTERBODY PLASMA
$M_i$ = 8.53, THROAT DIAMETER = 0.50 INCH, f = 4.25 GHz

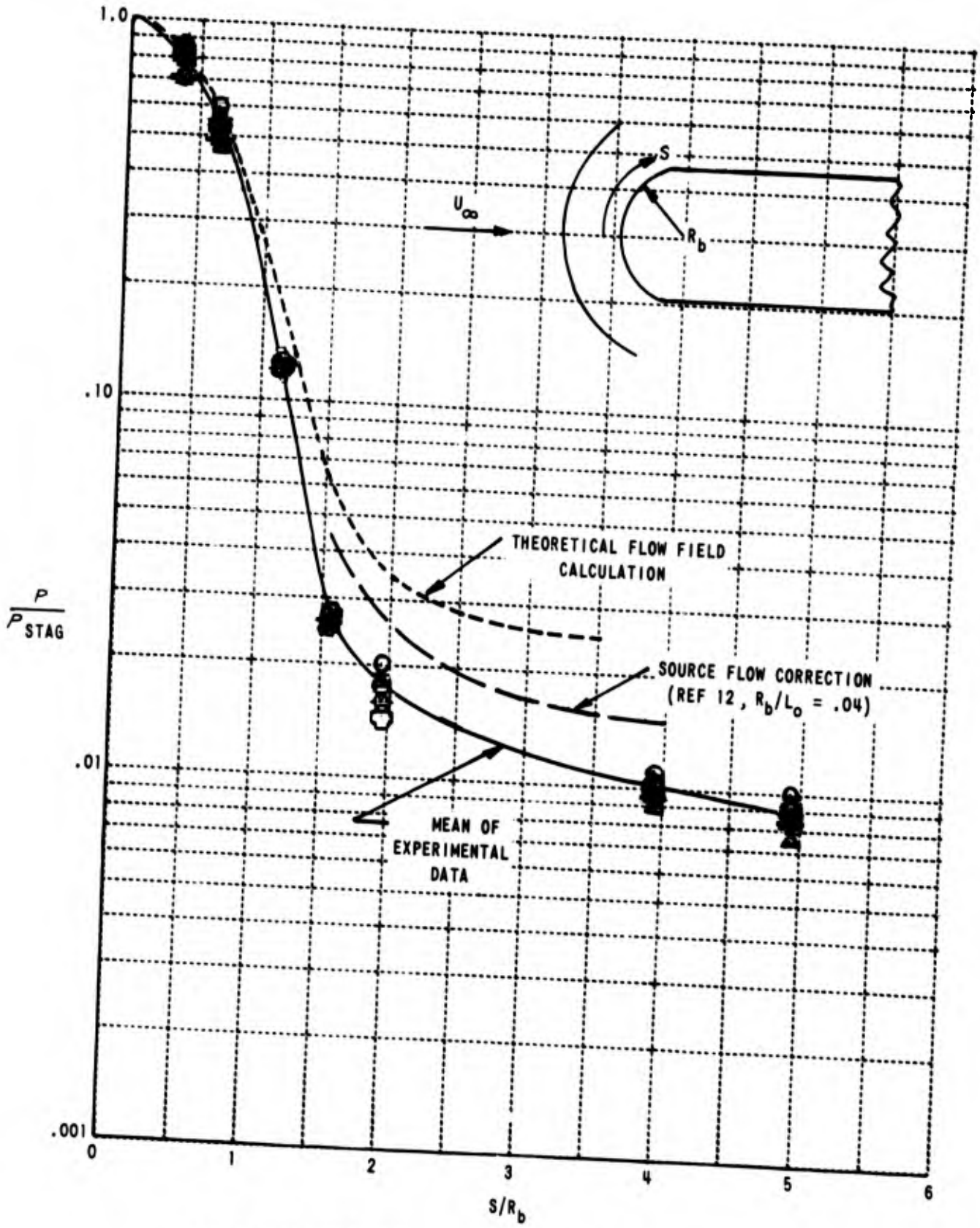


Figure 39 MEASURED SURFACE PRESSURE DISTRIBUTION ON HEMISPHERE-CYLINDER MODEL

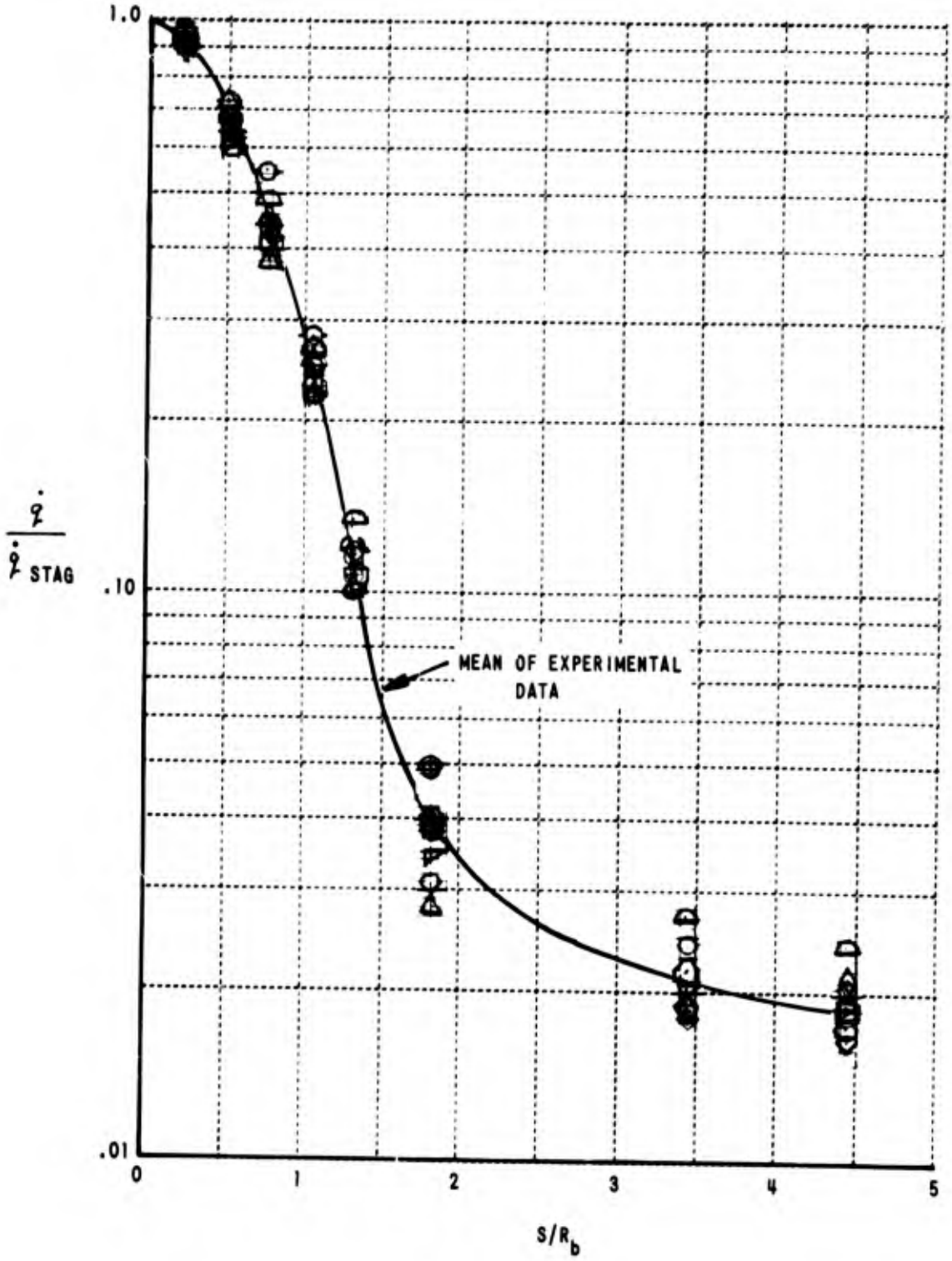


Figure 40 MEASURED HEAT TRANSFER DISTRIBUTION ON HEMISPHERE-CYLINDER MODEL

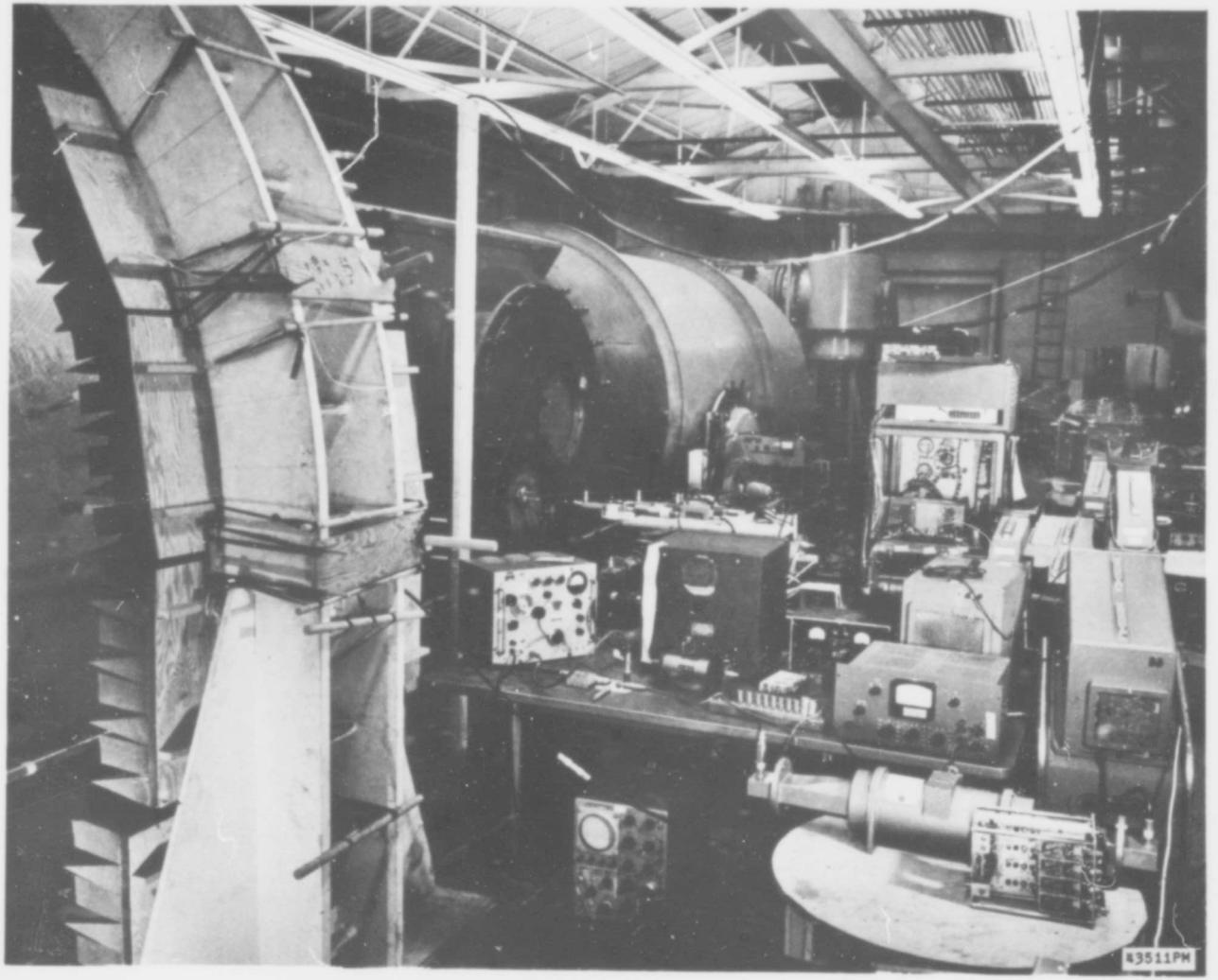


Figure 41 GENERAL VIEW OF THE MICROWAVE INSTRUMENTATION FOR THE BREAKDOWN TESTS

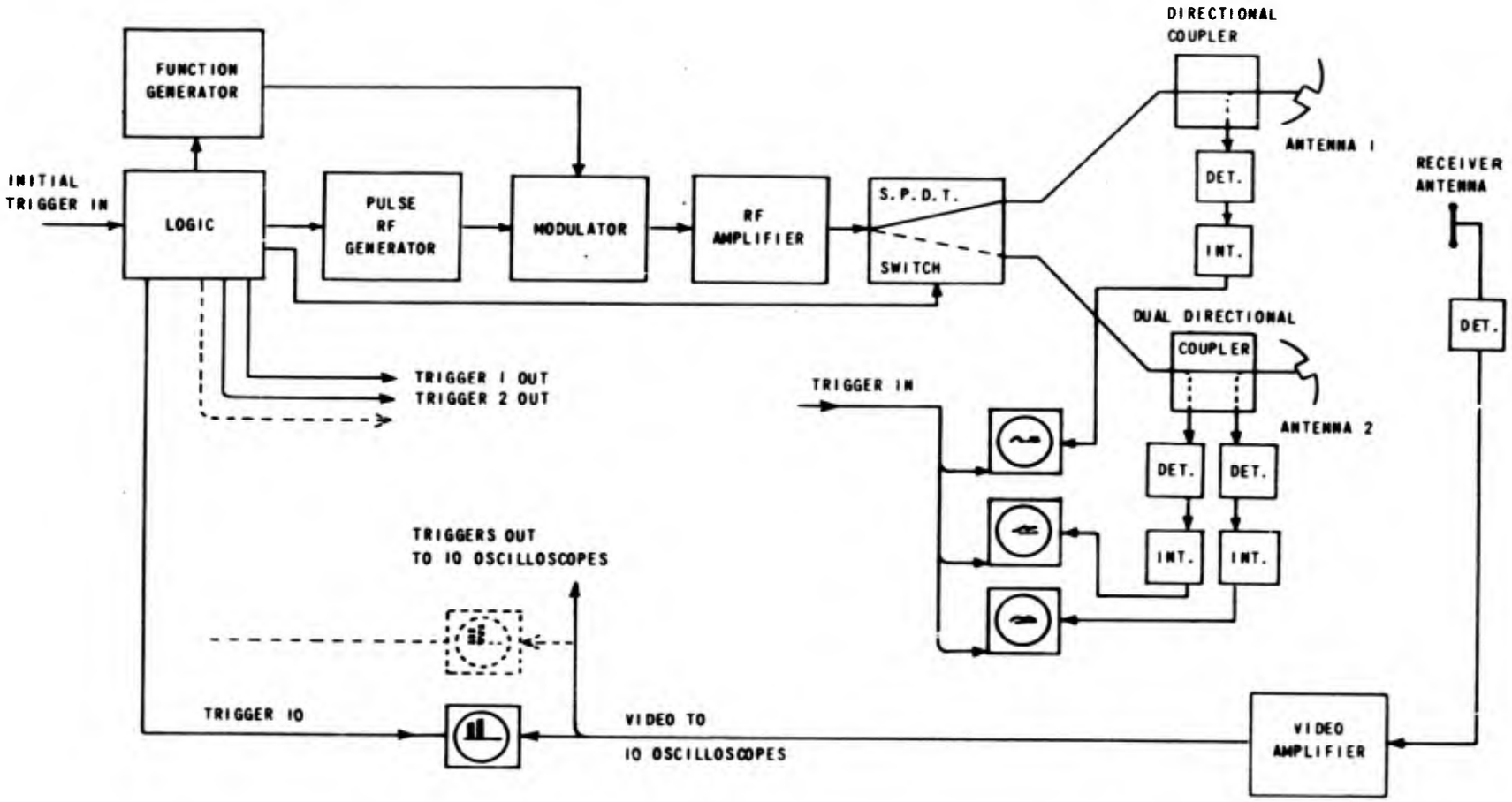


Figure 42 BLOCK DIAGRAM OF THE MICROWAVE INSTRUMENTATION FOR THE BREAKDOWN TESTS

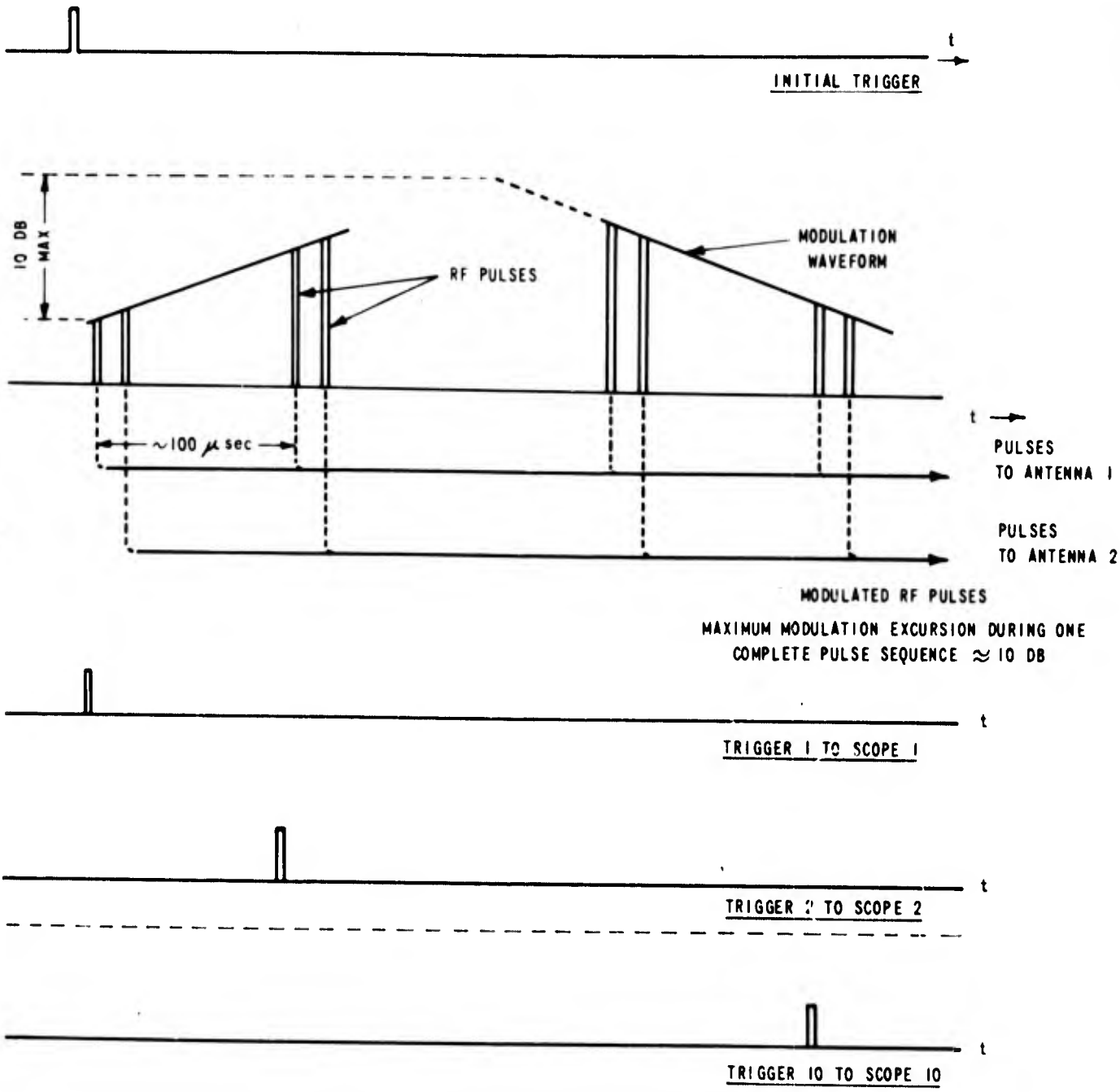


Figure 43 TRIGGER AND RF PULSE TIMING SEQUENCE FOR THE BREAKDOWN TESTS

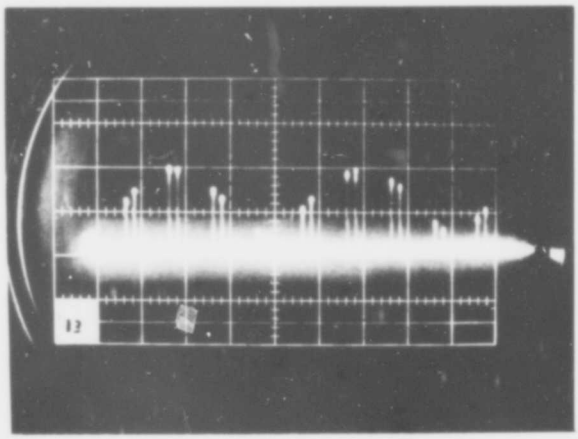

Figure 44 INCIDENT MICROSECOND PULSE TRAIN
EMPLOYED IN THE BREAKDOWN STUDIES
SWEEP = 0.1 msec/cm

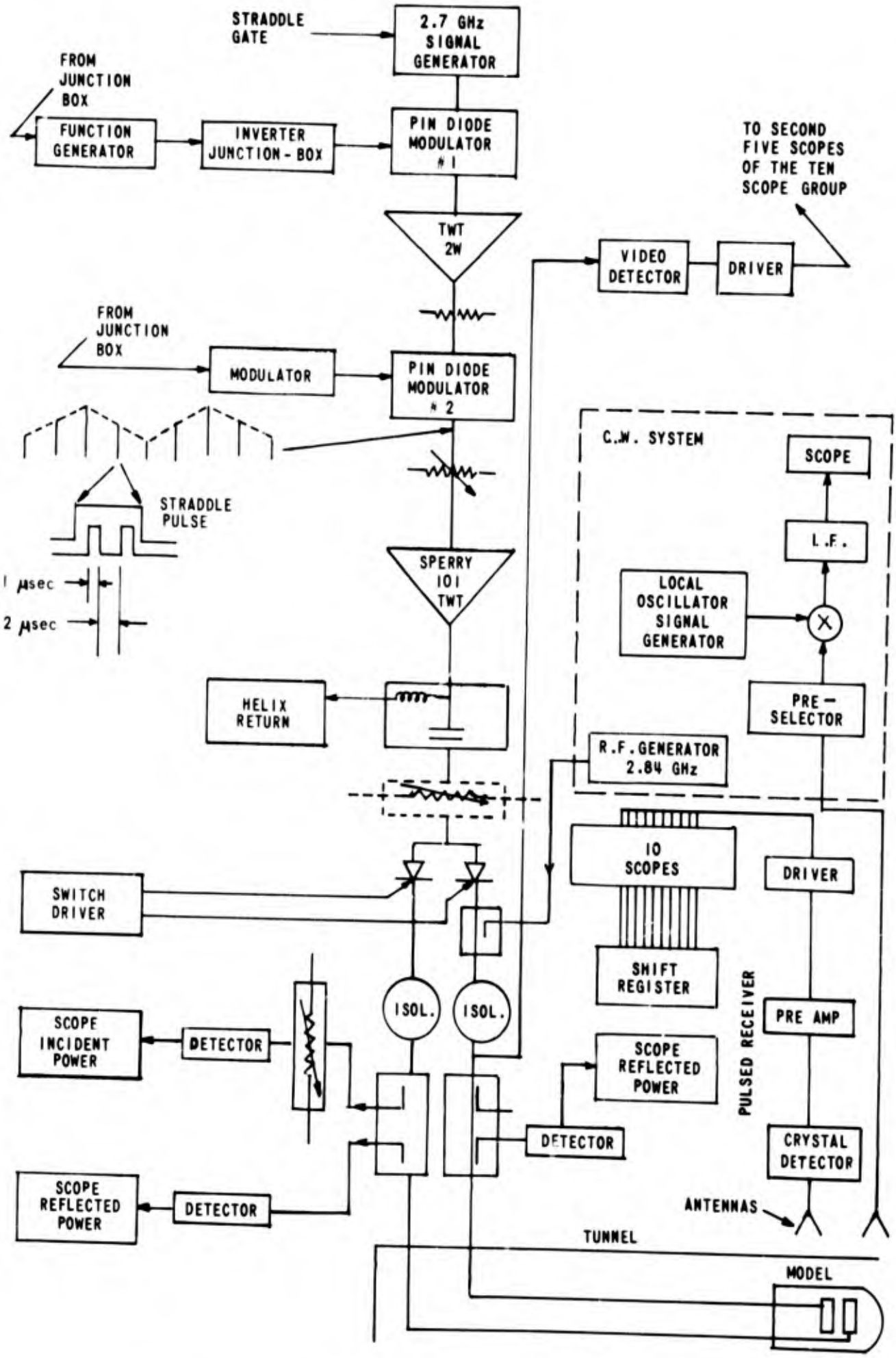


Figure 45 BLOCK DIAGRAM OF MICROWAVE INSTRUMENTATION FOR THE BREAKDOWN TESTS

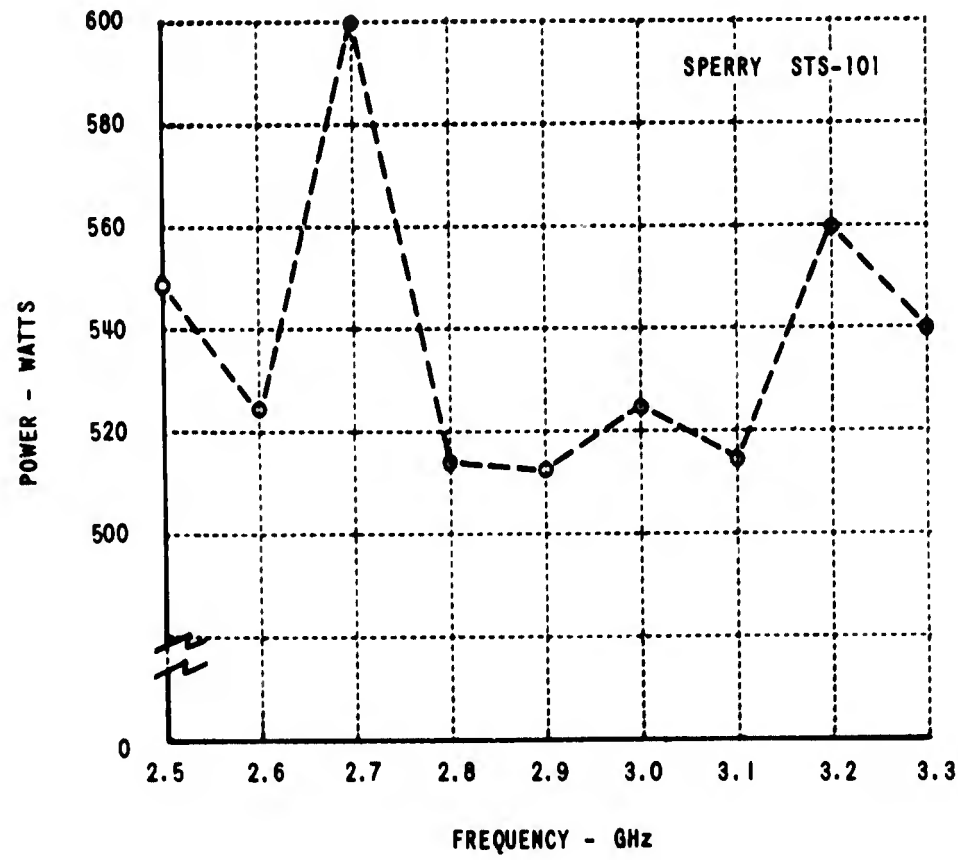


Figure 46 PEAK POWER OUTPUT OF THE TWT AMPLIFIER vs. FREQUENCY

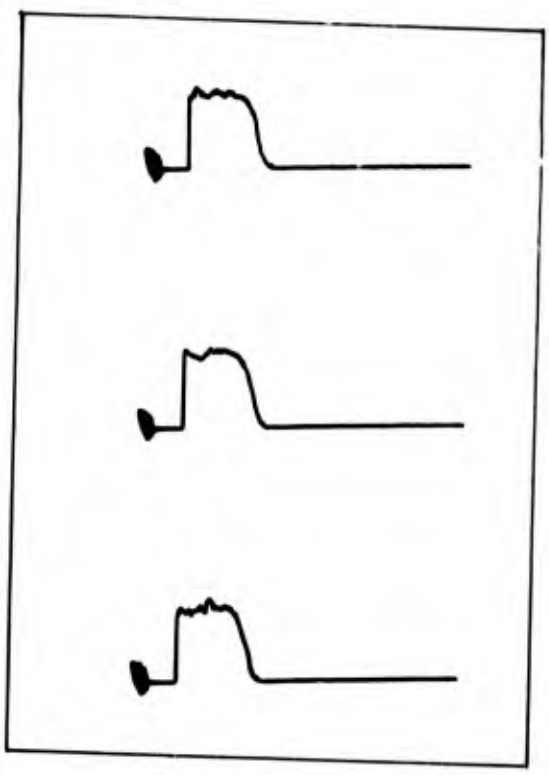

Figure 47 TYPICAL ONE-MICROSECOND PULSES FROM THE SPERRY STS - 101 TWT AMPLIFIER

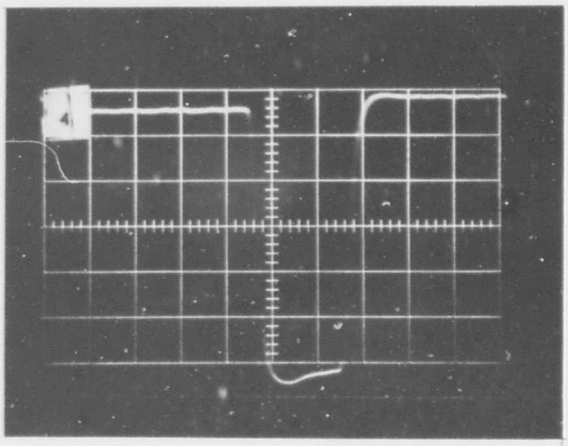

(a) RECEIVED PULSE.
SWEEP .5 μSEC/CM

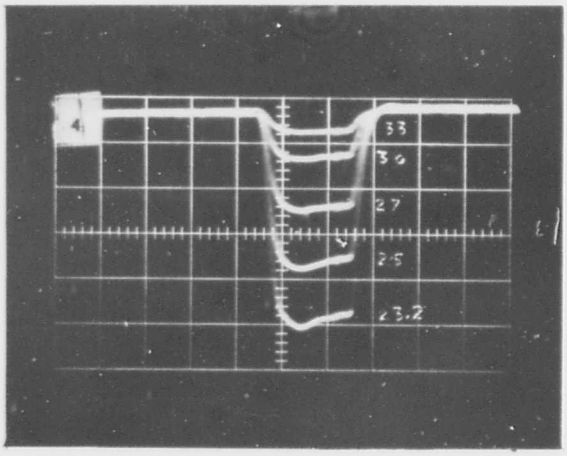


(b) POST RUN CALIBRATION.
SIGNAL LEVELS 23.2, 25, 27, 30, 33 dB

Figure 48 RECEIVED ONE-MICROSECOND PULSE.
PEAK PULSE POWER ~ 75 WATTS

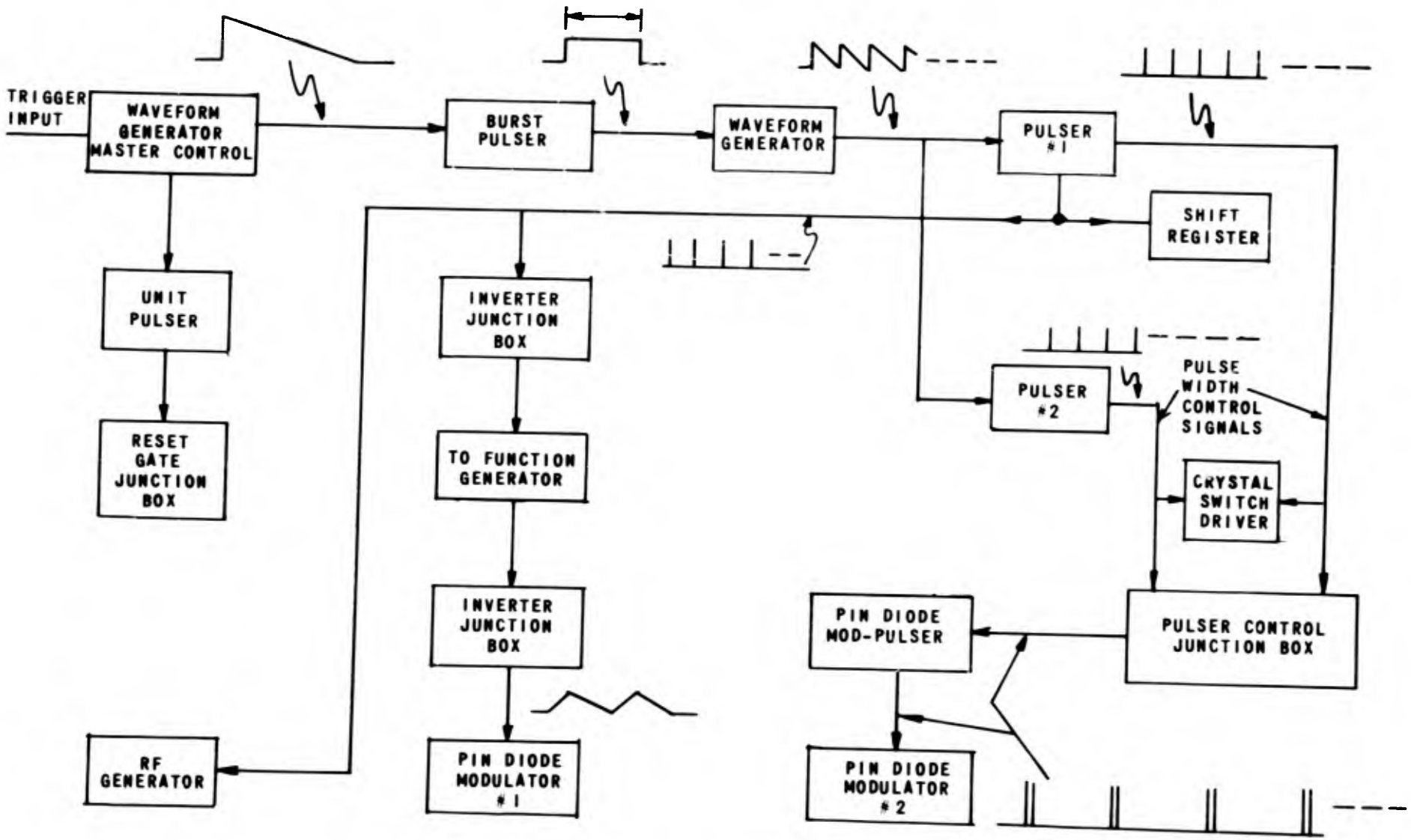


Figure 49 BREAKDOWN INSTRUMENTATION—PULSER AND WAVEFORM GENERATOR SUBSYSTEM

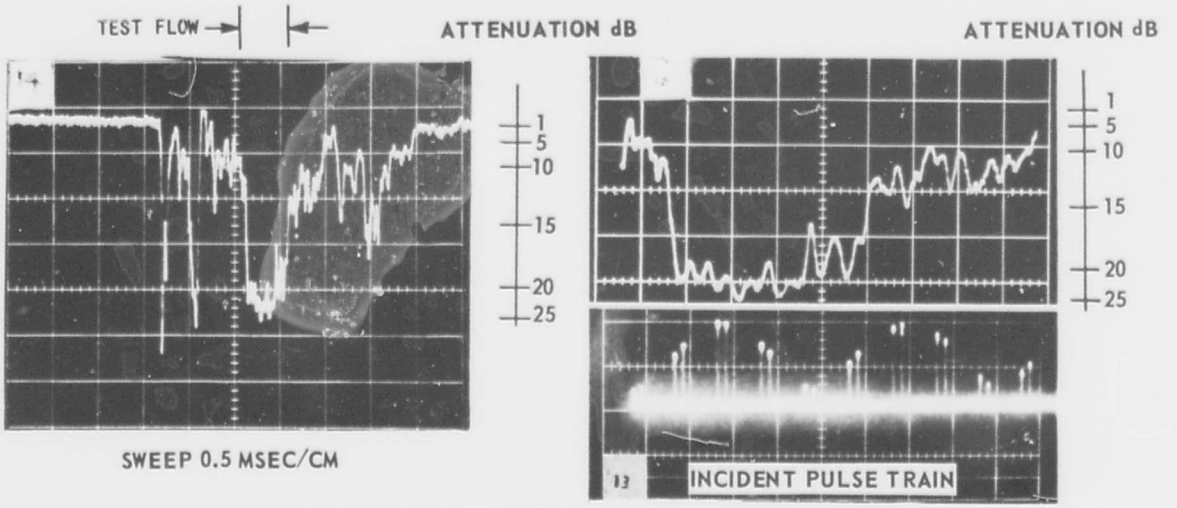


a. CW SIGNAL ATTENUATION

b. CW SIGNAL ATTENUATION AND INCIDENT PULSE TRAIN (5X EXPANDED SWEEP)

Figure 50 CW SIGNAL ATTENUATION AT 2.84 GHz AND PULSE TRAIN

RECEIVED AND CALIBRATION PULSES

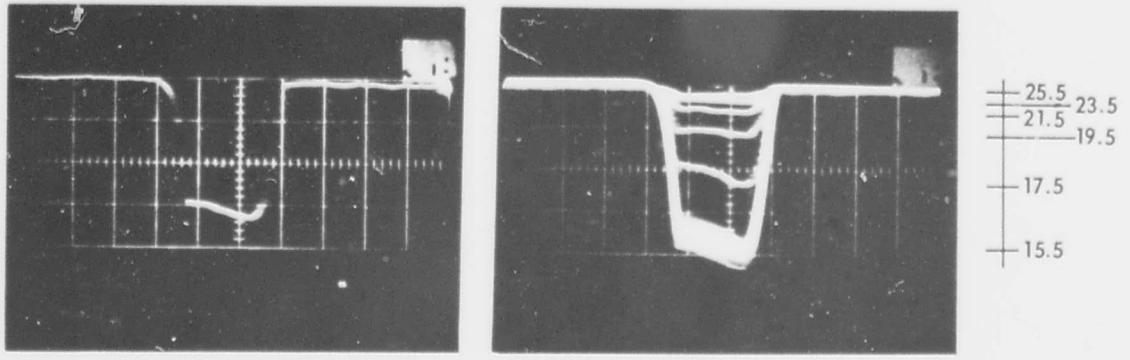


FIRST PULSE OF PULSE PAIR.
SWEEP .5μSEC/CM

CALIBRATION

ATTENUATION dB

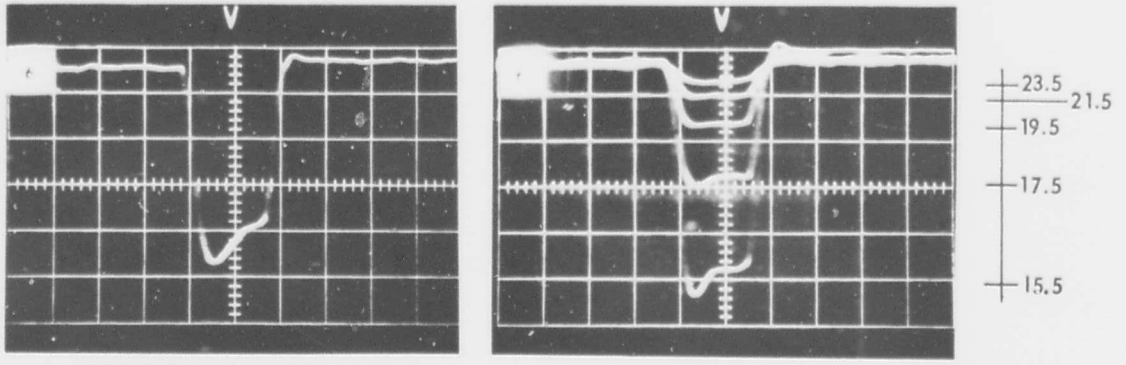


SECOND PULSE OF PULSE PAIR.
SWEEP DELAYED 19μSEC

CALIBRATION

ATTENUATION dB

Figure 51 RECEIVED PULSE SHAPES IN THE BREAKDOWN TESTS

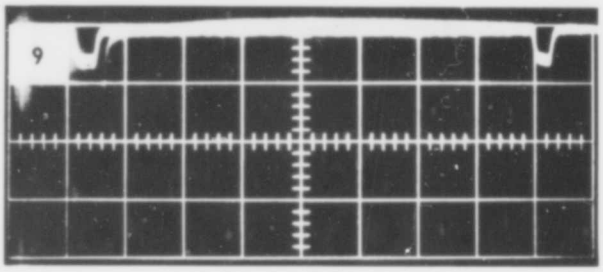


(a) 4th PULSE PAIR
SWEEP ~ 2 μsec/cm

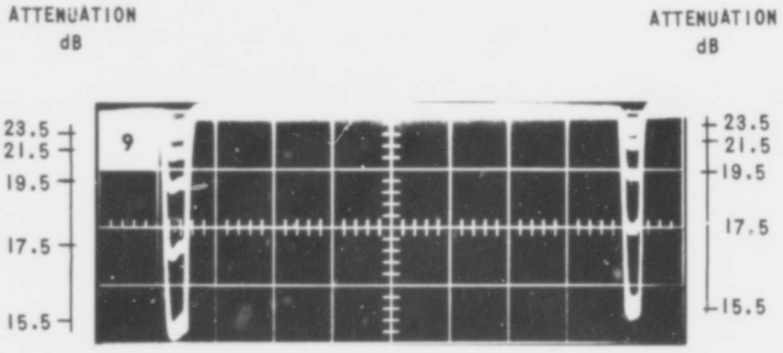


(b) CALIBRATION

Figure 52 RECEIVED PULSE PAIR IN THE BREAKDOWN TESTS

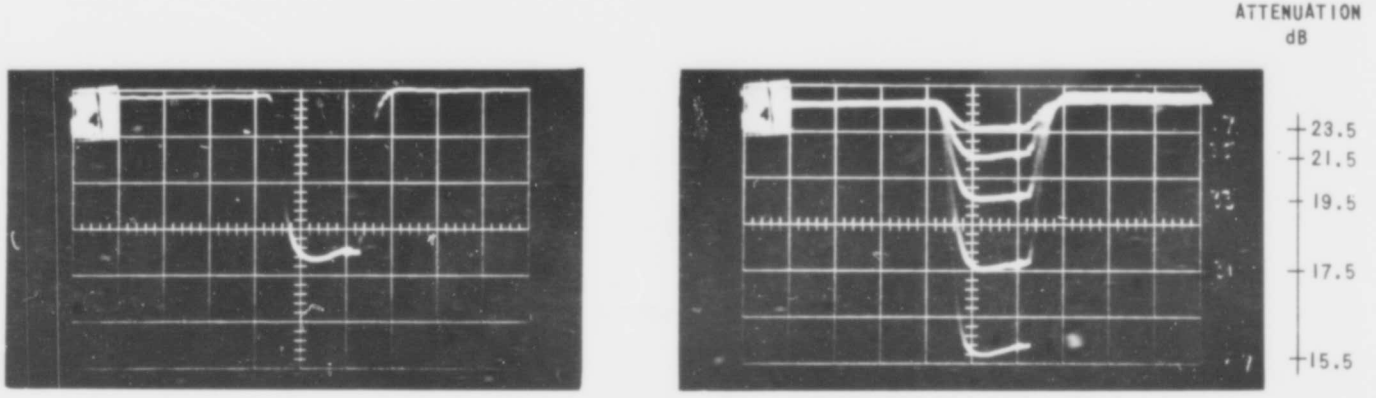


(a) EXTERNAL RECEIVER
SWEEP 0.5 μsec/cm

CALIBRATION

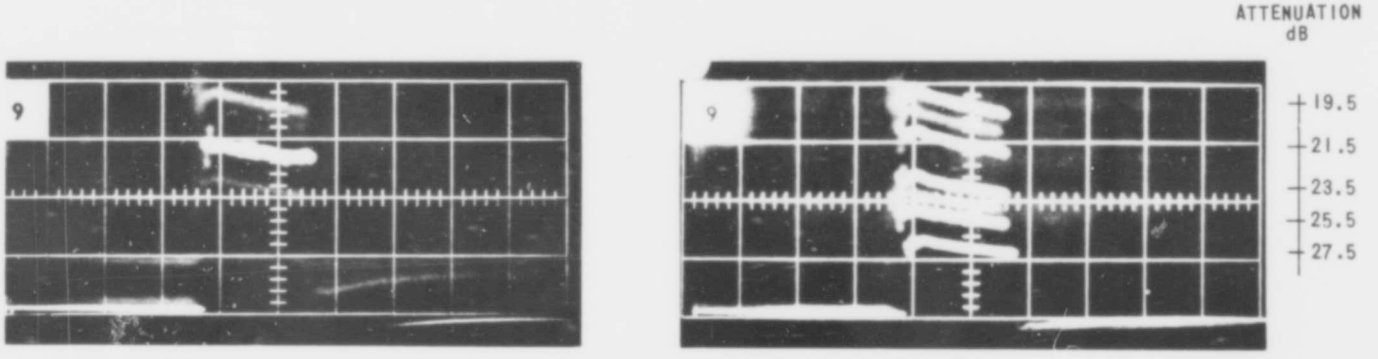


(b) COUPLED SIGNAL
SWEEP 0.5 μsec/cm

CALIBRATION



Figure 53 COUPLING BETWEEN TWO S-BAND ANTENNAS
(a) PULSE AT EXTERNAL RECEIVER
(b) PULSE AT AFT S-BAND ANTENNA

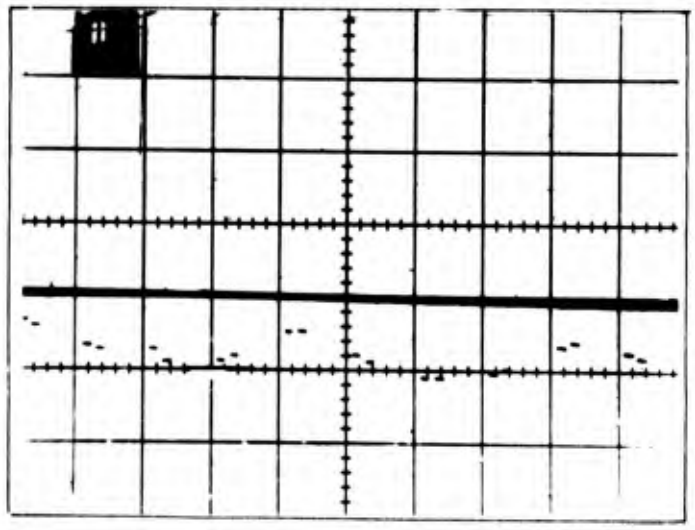

REFLECTED POWER

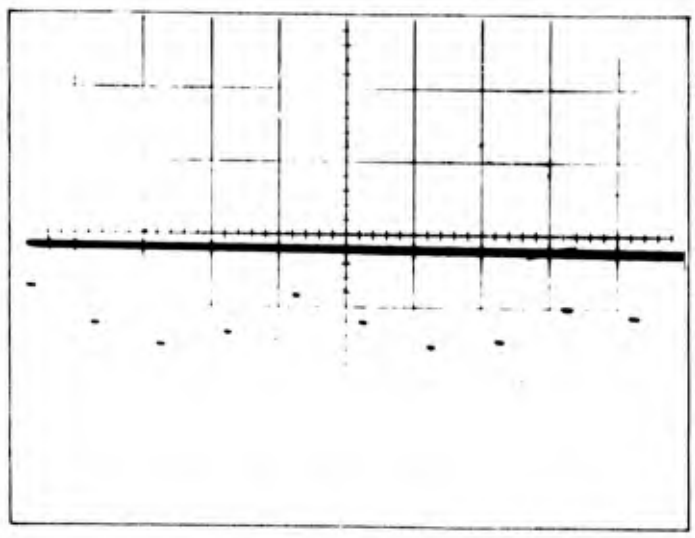

MAX POWER REFLECTION CALIBRATION

Figure 54 REFLECTED POWER AT TRANSMITTER ANTENNA

Unclassified

Security Classification

## DOCUMENT CONTROL DATA - R&D

*(Security classification of title, body of abstract and indexing annotation must be entered when the overall report is classified)*

1 ORIGINATING ACTIVITY *(Corporate author)*
Cornell Aeronautical Laboratory, Inc.
Aerodynamic Research Department
P.O. Box 235, Buffalo, New York 14221

2a REPORT SECURITY CLASSIFICATION
Unclassified

2b GROUP

3 REPORT TITLE
Analytical and Experimental Studies of Microwave Interaction with a Hypersonic Air Plasma

4 DESCRIPTIVE NOTES *(Type of report and inclusive dates)*
Interim Scientific Report

5 AUTHOR(S) *(Last name, first name, initial)*
Boyer, Donald W., Bitikofer, Dean R.

| 6 REPORT DATE | 7a TOTAL NO. OF PAGES | 7b NO. OF REFS |
|---|---|---|
| February 1967 | 108 | 12 |

| 8a CONTRACT OR GRANT NO. | 9a ORIGINATOR'S REPORT NUMBER(S) |
|---|---|
| AF 19(628)-4968 | Scientific Report No. 1 |
| b Project and Task No. 4642-02 | |
| c DoD Element No. 62405394 | 9b OTHER REPORT NO(S) *(Any other numbers that may be assigned this report)* |
| d DoD Subelement No. 681000 | AFCRL -67-0201 |

10 AVAILABILITY/LIMITATION NOTICES
DISTRIBUTION OF THIS DOCUMENT IS UNLIMITED

| 11 SUPPLEMENTARY NOTES | 12 SPONSORING MILITARY ACTIVITY |
|---|---|
| | Hq. AFCRL, (CRD)<br>United States Air Force<br>L.G. Hanscom Field, Bedford, Mass. 07130 |

13 ABSTRACT


Analytical and experimental studies are described of phenomena associated with the interaction of microwave radiation with the aerodynamically generated plasma surrounding a hemisphere-cylinder model in the CAL High Energy Shock Tunnel. The report is an interim report on continuing studies.

The program consisted of three parts, namely, (1) measurements of the changes in antenna radiation patterns at C-band (4.25 GHz), (2) an investigation of antenna breakdown, and nonlinear signal transmission effects and (3) measurements of the coupling between two antennas at S-band (2.7 GHz).

Exact nonequilibrium flow field calculations are discussed which describe the plasma properties surrounding the model and antennas. Analytical calculations have also included the computation of the complex transmission and reflection coefficients for microwave propagation through the inhomogeneous afterbody shock layer plasma.

A Phase I series of test measured the effect of the hypervelocity plasma on the radiation pattern from a C-band transmitting antenna located on the model cylindrical afterbody. Measurements of signal attenuation were made at four locations about the model at angular positions up to 90° from the normal to the antenna slot aperture. The measurements indicated an increase in the signal attenuation with angular departure of the receiving antenna from the slot normal.

A Phase II experimental program investigated nonlinear interaction effects due to propagation of variable high power S-band pulse radiation through the afterbody shock layer plasma. These later testsalso included measurements of the effect of the plasma on the coupling between two adjacent S-band antennas. While the coupling measurements were successful, no nonlinear interaction effects were observed at the Phase II power levels, primarily as a result of high power reflection due to plasma-induced antenna mismatch effects. Breakdown and coupling studies are to be continued at considerably higher power levels in a Phase III test program.


DD FORM 1 JAN 64 1473

Unclassified

Security Classification

| 14. KEY WORDS | LINK A | | LINK B | | LINK C | |
|---|---|---|---|---|---|---|
| | ROLE | WT | ROLE | WT | ROLE | WT |
| AERODYNAMICS<br>ANTENNA RADIATION PATTERNS<br>ATMOSPHERE ENTRY<br>BLACKOUT (ELECTROMAGNETIC)<br>MICROWAVE BREAKDOWN<br>ELECTROMAGNETIC-PLASMA INTERACTION<br>HYPERSONIC FLOW<br>PLASMA PHYSICS<br>NONEQUILIBRIUM FLOW | | | | | | |

## INSTRUCTIONS

1. ORIGINATING ACTIVITY. Enter the name and address of the contractor, subcontractor, grantee, Department of Defense activity or other organization *(corporate author)* issuing the report.

2a. REPORT SECURITY CLASSIFICATION: Enter the overall security classification of the report. Indicate whether "Restricted Data" is included. Marking is to be in accordance with appropriate security regulations.

2b. GROUP: Automatic downgrading is specified in DoD Directive 5200.10 and Armed Forces Industrial Manual. Enter the group number. Also, when applicable, show that optional markings have been used for Group 3 and Group 4 as authorized.

3. REPORT TITLE: Enter the complete report title in all capital letters. Titles in all cases should be unclassified. If a meaningful title cannot be selected without classification, show title classification in all capitals in parenthesis immediately following the title.

4. DESCRIPTIVE NOTES: If appropriate, enter the type of report, e.g., interim, progress, summary, annual, or final. Give the inclusive dates when a specific reporting period is covered.

5. AUTHOR(S): Enter the name(s) of author(s) as shown on or in the report. Enter last name, first name, middle initial. If military, show rank and branch of service. The name of the principal author is an absolute minimum requirement.

6. REPORT DATE: Enter the date of the report as day, month, year, or month, year. If more than one date appears on the report, use date of publication.

7a. TOTAL NUMBER OF PAGES: The total page count should follow normal pagination procedures, i.e., enter the number of pages containing information.

7b. NUMBER OF REFERENCES: Enter the total number of references cited in the report.

8a. CONTRACT OR GRANT NUMBER: If appropriate, enter the applicable number of the contract or grant under which the report was written.

8b, 8c, & 8d. PROJECT NUMBER. Enter the appropriate military department identification, such as project number, subproject number, system numbers, task number, etc.

9a. ORIGINATOR'S REPORT NUMBER(S): Enter the official report number by which the document will be identified and controlled by the originating activity. This number must be unique to this report.

9b. OTHER REPORT NUMBER(S): If the report has been assigned any other report numbers *(either by the originator or by the sponsor)*, also enter this number(s).

10. AVAILABILITY/LIMITATION NOTICES: Enter any limitations on further dissemination of the report, other than those imposed by security classification, using standard statements such as:

(1) "Qualified requesters may obtain copies of this report from DDC."

(2) "Foreign announcement and dissemination of this report by DDC is not authorized."

(3) "U. S. Government agencies may obtain copies of this report directly from DDC. Other qualified DDC users shall request through

_____."

(4) "U. S. military agencies may obtain copies of this report directly from DDC. Other qualified users shall request through

_____."

(5) "All distribution of this report is controlled. Qualified DDC users shall request through

_____."

If the report has been furnished to the Office of Technical Services, Department of Commerce, for sale to the public, indicate this fact and enter the price, if known.

11. SUPPLEMENTARY NOTES: Use for additional explanatory notes.

12. SPONSORING MILITARY ACTIVITY: Enter the name of the departmental project office or laboratory sponsoring *(paying for)* the research and development. Include address.

13. ABSTRACT. Enter an abstract giving a brief and factual summary of the document indicative of the report, even though it may also appear elsewhere in the body of the technical report. If additional space is required, a continuation sheet shall be attached.

It is highly desirable that the abstract of classified reports be unclassified. Each paragraph of the abstract shall end with an indication of the military security classification of the information in the paragraph, represented as *(TS), (S), (C), or (U)*

There is no limitation on the length of the abstract. However, the suggested length is from 150 to 225 words.

14. KEY WORDS: Key words are technically meaningful terms or short phrases that characterize a report and may be used as index entries for cataloging the report. Key words must be selected so that no security classification is required. Identifiers, such as equipment model designation, trade name, military project code name, geographic location, may be used as key words but will be followed by an indication of technical context. The assignment of links, roles, and weights is optional.